EPFL

Investigation of femtosecond laser-enabled 3D micro-infiltration processes

Présentée le 29 avril 2022

Faculté des sciences et techniques de l'ingénieur
Laboratoire Galatea
Programme doctoral en manufacturing

pour l'obtention du grade de Docteur ès Sciences

par

Enrico CASAMENTI

Acceptée sur proposition du jury

Prof. C. Moser, président du jury
Prof. Y. Bellouard, directeur de thèse
Prof. R. Osellame, rapporteur
Prof. R. Thomson, rapporteur
Prof. S. Lacour, rapporteuse

■ École
polytechnique
fédérale
de Lausanne

2022

To my family. . .

Acknowledgements

First of all, my gratitude goes to my thesis supervisor Prof. Yves Bellouard for the opportunity to pursue my doctoral studies in his laboratory. It has been a pleasure to share this incredible journey with you. I really appreciated your support, trust, and guidance throughout these four years.

A huge thanks goes to all my colleagues of the Galatea laboratory for creating a stimulating and fun research environment. With each of you, I discussed, learned, and laughed and, even if you don't say it, I know you will all miss my Christmas calendar, as much as I'll miss the lakeside BBQs. Here goes the list: Christos E. Athanasiou, Samuel Y. Benketaf, Olivier Bernard, Benedikt Braun, Antoine M. Delgoffe, Julien G. E. Gateau, Sargis Hakobyan, Benedikt Hermann, Ernesto Gribaudo, David Lambelet, Margarita Lesik, Saood I. Nazir, Josiane Pachaud, Vinod Parmar, Sacha Pollonghini, Arunkrishnan Radhakrishnan, Samuel P. Rey, Ruben Ricca, Manon Tardif, Gözden Torun, Pieter Vlugter, and Tao Yang. A special mention to Olivier and Saood for the countless enlightening discussions, Julien for preparing and maintaining almost all optical set-ups in the lab, Josiane for taking care of us, and Gözden and Pieter for the productive collaborations.

I further wish to acknowledge all the colleagues from other laboratories with whom I cooperated and from whom I learned a lot: Luciano Borasi - my inseparable research teammate, Raphael Charvët, Léa Deillon, Cyril Dénéréaz, Adeline Durand, Simone Frasca, and Francesco Gramuglia. A special thanks goes to Prof. Andreas Mortensen for the collaboration on the micro-infiltration process and for being an inexhaustible source of knowledge and support for my entire doctorate.

Last but not least, a big thanks goes to my dear family and girlfriend who always believe in me and are always there to support me when I need.

Neuchâtel, April 14, 2022   Enrico Casamenti.

Abstract

In the last decades, the femtosecond laser micromachining of glass has attracted a lot of attention due to its three-dimensional manufacturing ability and flexibility both in terms of compatible substrates and modification types. Yet, to fully unravel its potential for the production of multi-functional micro-devices, new techniques able to integrate multiple materials in the same glass substrate have to be conceived.

In this thesis work, we present a few techniques based on micro-infiltration to integrate both noble metals and glass architectures in a single glass substrate. Specifically, we select femtosecond laser-assisted chemical etching as a means to realize the glass molds and we design a vacuum pressure-assisted micro-infiltration process to cast different materials in fused silica.

The first part of the study focuses on femtosecond laser-assisted chemical etching as a manufacturing process. From a technological perspective, (i) we demonstrate the presence of a low laser fluence regime that enables an order of magnitude increase in laser writing speed while maintaining or surpassing selectivity and etching rate obtained for commonly used laser parameters, and (ii) we introduce sodium hydroxide as a novel and more environmentally friendly etching solution and show its superior performance compared to potassium hydroxide and hydrofluoric acid solutions. From the fundamental point of view, we prove that the low laser fluence etching regime is mainly governed by the presence of laser-induced molecular defects, and not by the presence of *nanogratings*, which were usually accounted for the origin of laser-assisted etching selectivity. Further, the observation of an anisotropy in the etching rate for different laser polarization states even with such a low laser fluence suggests that self-organization phenomena are initiated after far fewer pulses than the amount needed for the formation of nanogratings.

The second part of the study introduces a pressure-assisted micro-infiltration process and explains the challenges in translating casting to the micron-scale. In particular, we demonstrate the ability of such a process to produce micron-scale architectures of arbitrary geometrical complexity in 3D out of noble metals (silver, gold, copper, and their alloys) and an infrared glass from the chalcogenide family. Additionally, we study its potential for large-scale production compared to existing technologies and explore techniques to produce self-standing glass-metal composites and to perform multiple infiltrations of different materials on the same substrate.

This thesis is a step forward in the direction of manufacturing multi-materials monolithic multi-functional glass devices. This combination of materials with completely different

Abstract

properties allows almost unlimited possibilities in terms of designing novel architectures for applications in microtechnologies.

Zusammenfassung

Im Laufe der vergangenen Jahrzehnte hat sich die Mikrofabrikation von Glass mit Femtosekunden-Lasern etabliert, nicht nur da freie drei-dimensionale Geometrien hergestellt werden können, sondern auch aufgrund der hohen Flexibilität im Bezug auf kompatible Materialien und Arten der Modifikationen. Um das volle Potential dieser Fabrikationstechnologie für multi-funktionale Geräte auszuschöpfen, bedarf es neuer Methoden um verschiedene Materialien in ein und dem selben Glassubstrat zu kombinieren.

Im Rahmen dieser Doktorarbeit wurden Techniken zur Mikrofinfiltration von Edelmetallen und verschieden Gläsern in einem einzelnen Glassubstrat erarbeitet. Die Formen werden im Quarzglas mittels Femtosekunden-Lasern gefolgt von einem chemischen Ätzverfahren definiert. Anschliessend können verschieden Materialien mit Hilfe eines Vakuumverfahren in die Formen gefüllt werden.

Der erste Teil der Studie behandelt den chemischen Ätzprozess nach Femtosekunden-Laser Exposition als Fabrikationsprozess. Aus einer technischen Perspektive: (i) wir zeigen ein Regime niedriger Laserflussdichte auf, welches den Ätzvorgang um eine Grössenordnung beschleunigt, während die Selektivität gewahrt oder sogar übertroffen wird, im Vergleich zu üblicherweise verwendeten Laserparametern. (ii) Wir führen Natriumhydroxid als umwelt-freundlichere Ätzlösung ein und demonstrieren einen höhere Ätzrate als mit den Lösung Kaliumhydroxid und der oft verwendeten aber hochgradig toxischen Fluorwasserstoffsäure. Von einem fundamentalen Standpunkt aus zeigen wir, dass das Regime der niedrigen La-serflussdichte hauptsächlich durch laser-induzierte molekulare Defekte getrieben ist, und nicht durch *nanogratings* denen üblicherweise der selektive Ätzprozess zugeschrieben wird. Darüber hinaus deutet die Anisotropie der Ätzrate in Abhängigkeit der Laserpolarisation selbst bei niedriger Laserflussdichte darauf hin, dass selbstorganisierte Phänomene bereits durch deutliche weniger Pulse hervorgerufen werden als für die Formation von *nanogratings* benötigt werden.

Im zweiten Teil der Studie wird ein druckunterstütztes Mikrofiltrationsverfahren vorgestellt und die Herausforderungen bei der Übertragung des Giessens auf den Mikromassstab erläu-tert. Insbesondere demonstrieren wir die Fähigkeit eines solchen Verfahrens, Architekturen im Mikromassstab von beliebiger geometrischer Komplexität in 3D aus Edelmetallen (Silber, Gold, Kupfer und deren Legierungen) und einem Infrarotglas aus der Familie der Chalkoge-nide herzustellen. Darüber hinaus untersuchen wir ihr Potenzial für eine grosstechnische Produktion im Vergleich zu bestehenden Technologien und erforschen Techniken zur Her-stellung freiststehender Glas-Metall-Verbunde und zur Durchführung mehrerer Infiltrationen

verschiedener Materialien auf demselben Substrat.

Diese Arbeit stellt einen substantiellen Fortschritt für die Herstellung von monolithischen multi-funktionalen Mikrogeräten aus mehreren Materialien. Diese Kombination von Materialien mit völlig unterschiedlichen Eigenschaften bietet nahezu unbegrenzte Möglichkeiten für die Gestaltung neuartiger Architekturen für Anwendungen in einem breiten Spektrum im Bereich der Mikrotechnologie.

Résumé

Au cours des deux dernières décennies, la technologie d'usinage des verres par laser femtoseconde a reçu beaucoup d'attention grâce à sa capacité à fabriquer des pièces en trois dimensions, sa compatibilité avec un grand nombre de substrats, et la variété de types de modifications qu'elle permet de créer. Afin d'exploiter pleinement son potentiel pour la fabrication de micro-dispositifs multifonctionnels, de nouvelles techniques, capables d'intégrer plusieurs matériaux dans le même substrat en verre, doivent être développées.

Dans cette thèse, nous présentons de nouvelles méthodes dites de 'micro-infiltrations' pour inclure des structures à base de métaux nobles et de verres au sein d'un même substrat en verre de silice. Plus précisément, nous utilisons la gravure chimique assistée par laser femtoseconde pour fabriquer des moules en silice fondue, que nous combinons avec un procédé de micro-infiltration sous pression pour y couler les différents matériaux.

La première partie de cet ouvrage présente la gravure chimique assistée par laser femtoseconde en tant que méthode de fabrication. Spécifiquement, (i) nous démontrons l'existence d'un régime à basse fluence, permettant l'augmentation d'un ordre de grandeur de la vitesse d'écriture tout en maintenant, voire en surpassant, les niveaux de sélectivité et les taux de gravure chimique obtenus jusqu'à présent, et (ii) nous introduisons l'hydroxyde de sodium (NaOH), plus communément appelé soude caustique, comme nouvel agent de gravure chimique, plus écologique, pour lequel nous démontrons ses performances en comparaison de celles obtenues avec l'hydroxyde de potassium (KOH) ou l'acide fluorhydrique (HF), qui sont les deux agents utilisés jusqu'à présent. D'un point de vue plus fondamental, nous démontrons que le régime de gravure consécutif à une exposition au laser *à basse fluence* résulte principalement de la présence de défauts induits par l'irradiation laser dans la matrice de verre, plutôt que par l'existence de *nano-réseaux* - une hypothèse communément formulée pour expliquer la sélectivité à la gravure chimique des zones exposées. L'observation à des niveaux de fluences très faibles d'une anisotropie du taux de gravure en fonction de l'état de polarisation du laser suggère quant à elle que les phénomènes d'auto-organisation démarrent au bout d'un nombre d'impulsions bien plus faible que celui requis pour la formation de *nano-réseaux*.

La deuxième partie de cette thèse s'intéresse à un procédé de micro-infiltration sous pression, et détaille les difficultés pour miniaturiser le coulage à des échelles micrométriques. Nous montrons la capacité d'un tel procédé à produire des structures de géométries tridimensionnelles micrométriques et arbitrairement complexes constituées de métaux nobles (argent, or, cuivre, et leurs alliages) ou de verre de chalcogénures. De plus, nous étudions son potentiel

pour une production de masse en comparaison avec les technologies existantes. Enfin, nous proposons des méthodes pour produire des composites verre-métal autoporteurs et pour réaliser des infiltrations multiples de matériaux différents dans un substrat unique.

Ce travail forme une avancé vers la fabrication de micro-dispositifs en verre, multifonctionnels, monolithiques, et composés de plusieurs matériaux. Cette approche ouvre de nombreuses possibilités pour la conception de structures fonctionelles nouvelles, particulièrement adaptées à des applications en microtechnique.

Sommario

Negli ultimi decenni, la microlavorazione del vetro tramite laser al femtosecondo ha suscitato molta attenzione grazie all'abilità di fabbricare pezzi tridimensionali e alla flessibilità sia in termini di substrati compatibili che nel tipo di modificazione. Nonostante ció, per sfruttare completamente il suo potenziale nella fabbricazione di micro-dispositivi multifunzionali è necessario sviluppare nuove tecniche capaci di integrare piú materiali nello stesso substrato di vetro.

In questa tesi, vengono presentate alcune tecniche basate sulla micro-infiltrazione per integrare architetture sia di metalli nobili che di vetri in un unico substrato di vetro. Nello specifico, stampi di vetro alla micro scala sono fabbricati tramite la combinazione di incisione con laser al femtosecondo seguita da rimozione chimica, mentre un processo di micro-infiltrazione a vuoto e sotto pressione è progettato per infiltrare diversi materiali all'interno di substrati di quarzo fuso.

La prima parte dello studio si focalizza sulla combinazione di incisione con laser al femtosecondo e successiva rimozione chimica come processo manifatturiero. Da una prospettiva tecnologica, (i) viene dimostrata la presenza di un regime a bassa intensità laser che consente un aumento di velocità di scrittura di un ordine di grandezza, mantenendo o sorpassando allo stesso tempo la selettività e il ritmo di rimozione chimica ottenibile con i parametri laser comunemente utilizzati; (ii) viene introdotto l'idrossido di sodio come nuova e maggiormente ecosostenibile soluzione per la rimozione chimica e viene dimostrato come le sue prestazioni sorpassino quelle di soluzioni basate su idrossido di potassio o acido fluoridrico. Dal punto di vista dei fenomeni fondamentali, viene comprovato che nel regime a bassa intensità laser la rimozione chimica è prevalentemente governata dalla presenza di difetti a livello molecolare introdotti dal laser e non dalla presenza di *nanogratings*, a cui solitamente veniva attribuita l'origine della selettività. Inoltre, l'osservazione di una anisotropia nel ritmo di rimozione chimica collegata allo stato di polarizzazione del laser anche per il regime di bassa intensità suggerisce che fenomeni di auto-orientamento hanno inizio già dopo decisamente meno impulsi di quanti necessari alla formazione di *nanogratings*.

La seconda parte dello studio introduce un processo di micro-infiltrazione tramite pressurizzazione e presenta le sfide da affrontare nel traslare la pressofusione alla micro-scala. In particolare, viene dimostrata l'abilità di tale processo nel produrre architetture alla micro-scala di arbitraria complessità geometrica in 3D sia fatte di metalli nobili (argento, oro, rame e le loro leghe) che di vetri per l'infrarosso della famiglia dei calcogenuri. Inoltre, viene studiato il potenziale per produzione in larga scala rispetto alle tecnologie esistenti e vengono esplorate

tecniche per produrre compositi vetro-metallo e per realizzare molteplici infiltrazioni di diversi materiali nello stesso substrato.

Questa tesi rappresenta un passo avanti nella manifattura di dispositivi di vetro monolitici multi-funzionali e multi-materiali. La combinazione di materiali con proprietà completamente differenti permette una libertà pressochè illimitata in termini di progettazione di nuove architetture per applicazioni in microtecnologia.

Contents

Contents

1 Introduction

Last decades have seen extraordinary development in terms of manufacturing capability both at micron- and nano-scale. In the '90s, the pioneering work of Davis *et al.* [1] paved the way to femtosecond laser direct writing of waveguides inside a glass. Shortly, this technology attracted lots of attention thanks to its flexibility in terms of multi-substrates compatibility and three-dimensional printing capability. In parallel, Kondo *et al.* [2] first and Marcinkevicius *et al.* [3] then demonstrated that the regions of the glass illuminated with femtosecond laser pulses could be selectively removed by chemical etching at a much higher rate than the surrounding pristine material. In this fashion, femtosecond laser micromachining of glass based on laser irradiation followed by chemical etching was initiated. As a result, femtosecond laser became a flexible and versatile platform both for direct-writing of optical components and micromachining of glass, and this, in three dimensions. In the following years and until nowadays, a multitude of devices and applications have been explored. From mechanical micro-actuators [4–8] to integrated photonic devices as 3D waveguides, couplers [9, 10], Bragg gratings [11–14], phase plates [15, 16], and photonic lanterns [17, 18], just to cite a few. Furthermore, the combination of optical devices with micro-fluidic channels and components [19–25] attracted a large research interest for lab-on-a-chip applications [26–33], while the possibility of creating 3D highly dense and stable modifications in glass resulted in studies in the context of memory storage [34–36].

To further expand the use of femtosecond laser micromachining of fused silica as a platform for functional integration, this work investigates the use of infiltration processes to form glass-metal and glass-glass composites.

This work aims at *defining methods for integrating complex geometries of different materials, in particular glass and metals, in a single glass host substrate*. Specifically, (1) we explore femtosecond laser-micromachining of glass as a technique to fabricate three-dimensional micron-scale free-form cavities that we fill with metals and glass by a vacuum pressure-assisted infiltration technique, and to this end, (2) we optimize femtosecond laser-assisted chemical etching processes in terms of both speed and aspect ratio and we investigate the origin of the etching selectivity.

This introductory chapter presents the core technologies of femtosecond laser micromachining of glass and micro-infiltration as a means for building multi-materials 3D structures, and ends by describing the thesis' objectives and outline.

1.1 Ultrafast laser processing of transparent materials

Since their invention in 1960, lasers have become a fundamental tool for a multitude of fields, ranging from telecommunications to medicine and from fundamental research to industry and particularly relevant for this dissertation, manufacturing. A milestone in pulsed-lasers history was the discovery of chirped pulsed amplification (CPA) in 1985 [37]. It consists in

temporally stretching the laser pulse prior to the amplification, so to avoid the build-up of high-peak intensity in the amplifier cavity. This conceptually simple, but fundamental idea, combined with high spectral bandwidth crystals like Ti-sapphire, led to high peak-power table-top lasers.

Around the same period, nanosecond lasers emerged as an efficient, high-throughput, and innovative tool for metal processing, both in common industrial applications such as thin-sheets drilling, cutting, and engraving and innovative additive manufacturing processes such as selective laser melting and sintering. Since then, femtosecond lasers have revolution-ized material processing. Femtosecond pulses being shorter than characteristic relaxation times observed during the laser-matter interaction, the thermal damage and laser affected zone are greatly reduced, leading to higher spatial resolution and high processing quality. Furthermore, tightly-focused femtosecond laser in transparent material overcoming a given threshold-intensity (e.g. in the range of 10^{13} W/cm^2 for fused silica [38]), triggers *non-linear* absorption phenomena that lead to material modifications confined in the focal volume or into even smaller volume. This effect enables laser-induced transparent materials modifica-tions three-dimensionally (3D) in the bulk.

In transparent materials, depending on the material, laser parameters, and focusing condi-tions, different types of laser-induced modifications can be found: (i) a local homogeneous modification, usually associated with a densification, and consequently, a refractive index increase; (ii) the formation of self-organized structures, commonly identified as '*nanograt-ings*', which often increase locally the reactivity of the material to etchants, but also bear interesting optical birefringence properties; (iii) confined bulk melting that can culminate in micro-explosions [39–41]; (iv) elemental diffusion both in doped glass, as in [42], and at the interface of different materials (see for instance [43]); and (v) localized crystallization [44, 45].

During the last two decades, the first three types led to industrial applications in the field of manufacturing. In the sequel, we focus our attention on the first two that are of particular interest in the context of this study.

On one hand, homogeneous densification and related waveguiding properties were ob-served in a variety of substrates. Fused silica [1, 46–50], silicate-based glass [46, 51, 52], lithium niobate [53–59], diamond [60–62], and silicon [63] are just but a few where this effect was reported. On the other hand, laser-induced self-organized structures, even if not always related to an enhanced etching rate, have been reported in fused silica [64], silicate-based glass [25, 65–69], tellurites [70], chalcogenides [71–73], diamond [74, 75], and sapphire [76].

In this work, we focus on femtosecond laser interaction with fused silica, which along the years has been adopted as the principal substrate for the experimentation and integration of femtosecond laser-written devices. Apart from being transparent over a broad spectral range (from ultraviolet to near-infrared), fused silica is highly stable from a chemical point of view, making it an ideal candidate for both bio-compatible and harsh environments applications. Its glass transition temperature surpasses a thousand degrees Celsius and its coefficient of thermal expansion is one of the lowest among non-engineered materials, which combined

with high mechanical strength makes fused silica thermal-shock resistant. Despite having a low toughness like other glass, micro-machined fused silica according to the process used in this work shows a tensile strength well above 1 GPa with low failure probability [77, 78]. Finally, it has one of the lowest internal friction coefficients, resulting in near-zero thermoelastic losses. Altogether, these characteristics elect fused silica as an ideal substrate for the integration of multi-functional devices ranging from micro-mechanics to micro-optics and micro-fluidics.

The following sections present in more detail first, the mechanisms behind ultrafast laser-matter interaction with dielectrics, and then, with a special focus on fused silica, the two main types of modification achievable, and their broad range of applications.

1.1.1 Ultrafast laser-matter interaction

Ultrafast is commonly attributed to pulsed lasers with pulses in the order of the picosecond (10^{-12} s) or less. A unique feature is that with such a short laser-matter interaction thermal and structural events triggered by the light do not happen concomitantly to the pulse presence, which greatly reduces the laser affected zone and undesired modification occurring outside the zone under laser exposure. Paramount to the duration of the pulse, ultrashort pulses allow for reaching high-peak power without the need for a large amount of energy.

By focusing an ultrafast laser, it becomes possible to overcome a power density threshold dependent on the material properties that triggers non-linear absorption events in a substrate, even with a wavelength for which the material is transparent. The process starts with the excitation of seed electrons (that constitute free carriers) from the valence to the conduction band through multiphoton absorption phenomena. These seeded electrons continue absorbing energy from incoming photons until they eventually become energetic enough to in turn excite other electrons from the valence band during impact ionization events. This sequence of events populates a plasma that rapidly expands. As the pulse ends, the plasma is no longer fed and two main energy-dissipation mechanisms occur: carrier-carrier scattering, i.e. the recombination of the electrons within the glass matrix, and carrier-phonon scattering, i.e. the energy transfer from electrons to atomic-scale vibrational states of the lattice. Both dissipation processes result in the creation of defects and hence a confined modification imprinted in the glass structure.

Figure 1.1 depicts the typical time-scale of key laser-matter interaction mechanisms. The events triggered by an ultrashort pulse last for relatively long times compared to the pulse duration. For example, the typical relaxation time for fused silica is around 1 μs. To avoid entering into an energy accumulation regime (referring to pulse-to-pulse cumulative effects - and labeled '*cumulative regime*'), the interval between two subsequent pulses should be higher than 1 μs, which implies that the repetition rate of the laser should be set below 1 MHz, typically.
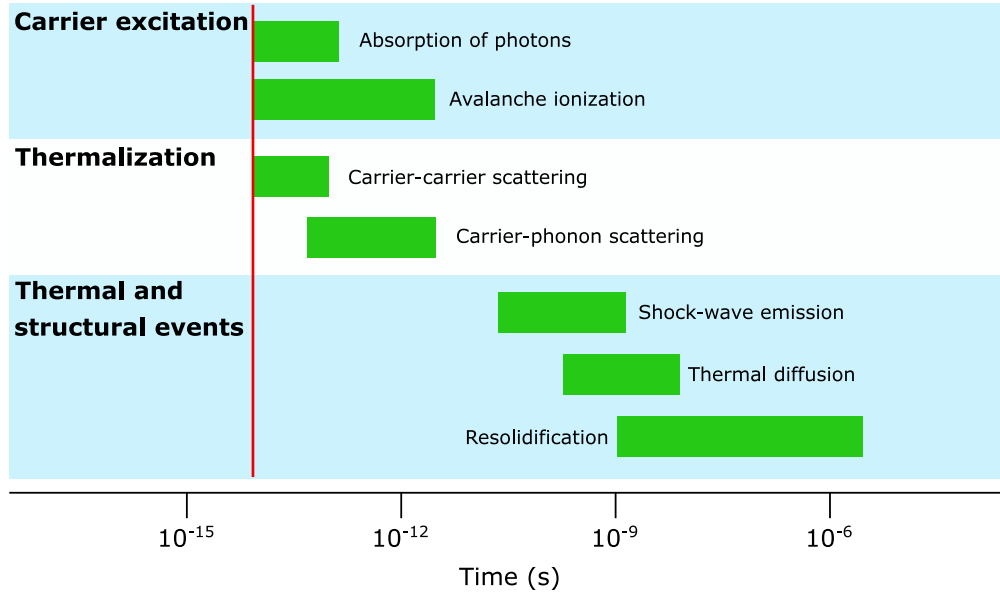
Figure 1.1: *Typical timescale of physical laser-matter interaction mechanisms between a femtosecond laser pulse and a transparent material, reprinted from [79]. The red line shows the typical pulse width used in this work, i.e. 270 fs. However, the material undergoes changes over a time frame order of magnitude longer than the pulse itself.*

Non-ablative and non-cumulative femtosecond laser interaction with fused silica leads to permanent defects in the glass-matrix when the material comes at rest. At a molecular level, oxygen deficiency centers (ODCs), non-bridging-oxygen-hole-centers (NBOHC), color centers (E' centers) and others [80] form and are considered precursors for the formation of morphological defects and notably for the presence of free molecular oxygen trapped in nano-pores [68, 81, 82]. At a microscopic *morphological* level, depending on the laser parameters and focusing conditions, different types of modification can be obtained. Figure 1.2 shows the three main regimes identified for fused silica.

Type I modification occurs for short pulse width (below ≃ 200 fs) and pulse energies, just above the modification threshold. The region irradiated by the laser undergoes an homogeneous densification that results in a refractive index increase typically in the range of 10^{-3} [1].

Type II modification occurs for higher pulse energies (above ≃ 200 nJ) and/or longer pulse widths (above ≃ 200 fs) than the type I. In this case, the laser-modified region exhibits an anisotropic and periodic structure of sub-wavelength nanoplanes known as *nanogratings* [64]. These structures present a strong form birefringence [83, 84] and an enhancement in etching rate with respect to the pristine material that, as understood later, enables selective etching, as first observed by [3].

Type III modification occurs for long pulse widths (above ≃ 200 fs) and high pulse energies (above ≃ 300 nJ). With such conditions, the modified region is formed by disrupted nanogratings [85].
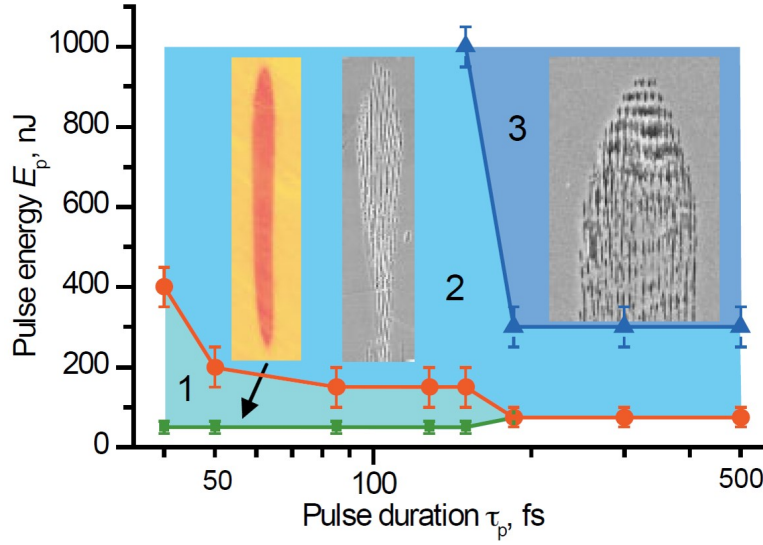
Figure 1.2: *Graphical view of the three types of modification regimes obtainable by irradiating fused silica with a femtosecond laser with different pulse energies and duration. The insets show the morphology of the laser modified region for each type through a cross-sectional view [86].*

1.1.2 Type I - Homogeneous modifications

In 1996, Davis *et al.* demonstrated that by exposing fused silica with low energy ultrashort pulses, a local increase of the refractive index of the material occurs, and this, while inscribing freeform 3D patterns inside the substrate [1]. The refractive index increase is in the order of 10^{-3} and enables 3D direct-writing of optical waveguides that demonstrated low optical losses ($\simeq 1$ dB/cm) [1, 87–90].

This homogeneous modification regime, later on associated with *type I* modification, has drawn attention in the last decades, both in the academic and industrial environments. Different applications have been explored, ranging from waveguides-coupling [9, 10] to photonic lanterns [17, 18], and from Bragg gratings [11–14] to waveguide amplifiers [91]. Figure 1.3 shows few selected optical devices fabricated in silica by femtosecond laser direct-writing.

1.1.3 Type II - Nanogratings

The type II modification is associated with the formation of nanogratings in the laser-modified regions. These nanoplanes orientation can be tuned by controlling the electric field orientation (i.e. the polarization) of the incoming laser beam [92]. Although several hypotheses have been proposed, the origin of these self-assembled nano-planes remains debated. The first model explaining the formation of nanogratings was presented by Shimotsuma *et al.* [64] in 2003. Their hypothesis is that interference between the laser field and the laser-induced plasma waves is responsible for the periodically organized structure. According to this model, the nanogratings period depends on plasma properties and has a predictable periodicity
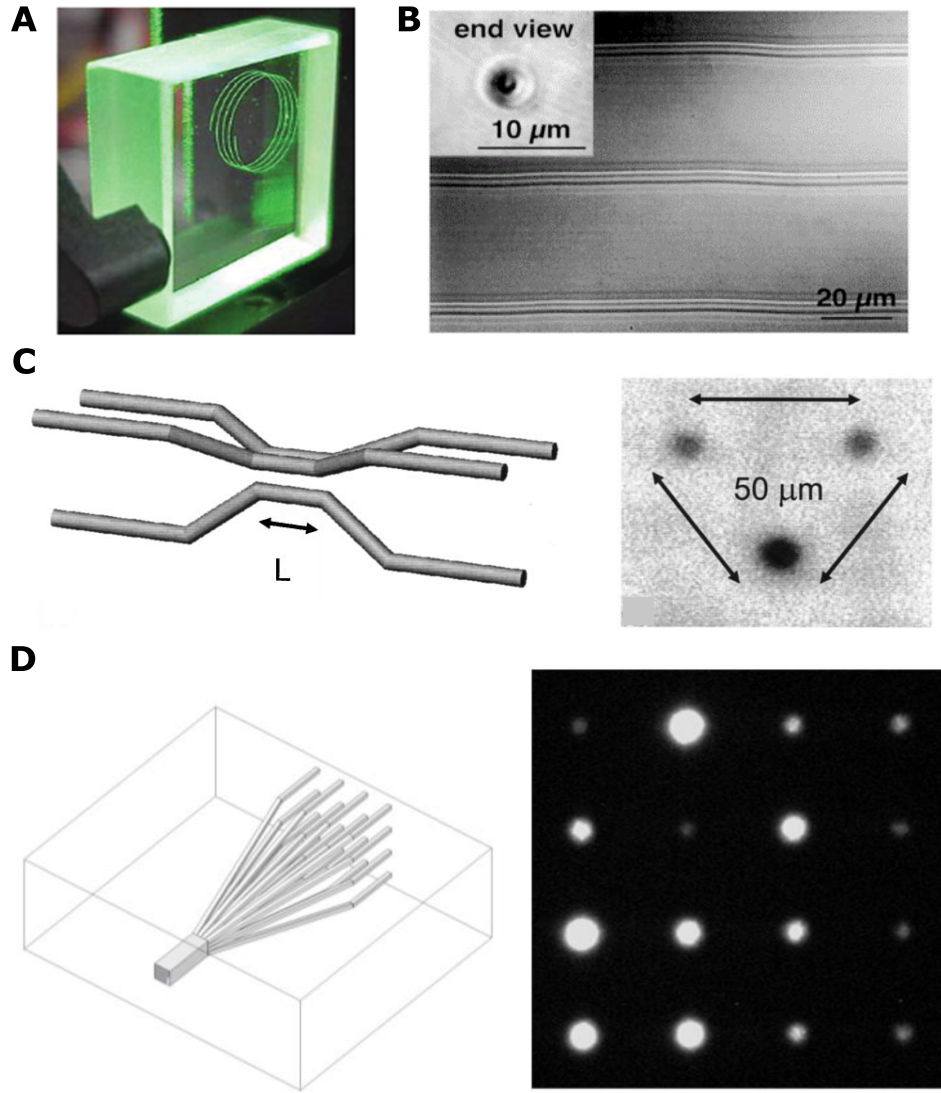
Figure 1.3: *Femtosecond laser written optical devices integrated in fused silica. (A) Spiral optical waveguide fabricated by Translume inc. [88] (B) Optical micrograph of linear waveguides [38]. (C) Triple waveguide splitter design (left) and tested output intensity (right) [10]. (D) Photonic lantern design (left) and tested output intensity (right) [18].*

proportional to the incoming laser wavelength. Some other researchers also suggested a similar dependence based on a different model [92, 93]. However, more recent studies show that this correlation is not proven and evidence contradicts this hypothetical correlation [65, 67]. In parallel, it has been found that nanogratings' period decreases continuously with the number of applied pulses [64, 67, 82] and can be controlled by tuning the temporal pulse envelope [94]. Another model was proposed by Taylor *et al.* [86] in 2008 and is based on the evolution of spherical 'nanoplasmas' from hot spots arising around randomly spread defects and/or color centers that results in anisotropic multiphoton ionization. Despite the apparent validity in predicting a half-wavelength nanogratings period (later observations of shorter

periodicity were not known at that time), it fails to explain the influence of the number of pulses. Recently, a study from Rudenko *et al.* [95] provides a model that can explain both periods and orientation of the nanogratings and help to identify the physical origin of these self-organized structures. However, further experimental studies are needed to conclude once for all this quest around the nanogratings origin. For example, as we will see in Chapter 2, the common belief that self-organization concerns only nanogratings might be incorrect since evidence of self-organization was found for modifications with a remarkably low number of overlapping laser pulses (that does not produce the classical nanograting morphology).

Application-wise, nanogratings present two main characteristics: (i) they induce a strong form-birefringence ($\simeq 10^{-2}$) [84, 96], and (ii) they present an enhanced etching rate, compared to the pristine material, enabling selective etching with HF [2, 3], KOH [97], and NaOH [98]. For the latter, the classical interpretation of etching selectivity being driven only by the presence of the porous nanogratings is rebutted by the discovery of extreme etching rates for modifications induced with exceptionally low laser fluence, for which, no nanogratings are observed.

On one hand, by combining the induced form-birefringence with the 3D capability of femtosecond laser modifications, sophisticated optical retardance patterns have been engineered for the integration of waveplates or polarizers [15] as well as for high-density data storage [34, 35]. In parallel, others exploited the stress originating from imprinted nanogratings in bulk glass [99, 100] to induce a birefringent behavior and engineer specific retardance patterns [16]. Few selected examples are shown in Figure 1.4.

On the other hand, the possibility to write any 3D-pattern and etch it selectively has opened to freeform micromanufacturing of glass for high-precision components. Along the years, to cite few examples, this technology enabled the fabrication of geometries impossible to produce with conventional methods as the cross-pivot in Figure 1.5 A [101], microfluidic devices [19–25] and many different micromechanical devices for instance actuated by electrostatics [4], dielectrophoresis [5, 8], or laser-induced deformations [6, 7] (few examples are shown in Figure 1.5). As a side note concerning micro-mechanics and optomechanics, fused silica components fabricated by femtosecond laser micromachining followed by chemical etching have shown to sustain extreme stress levels, higher than their metallic counterparts, eventually reaching 2.4 GPa [102].
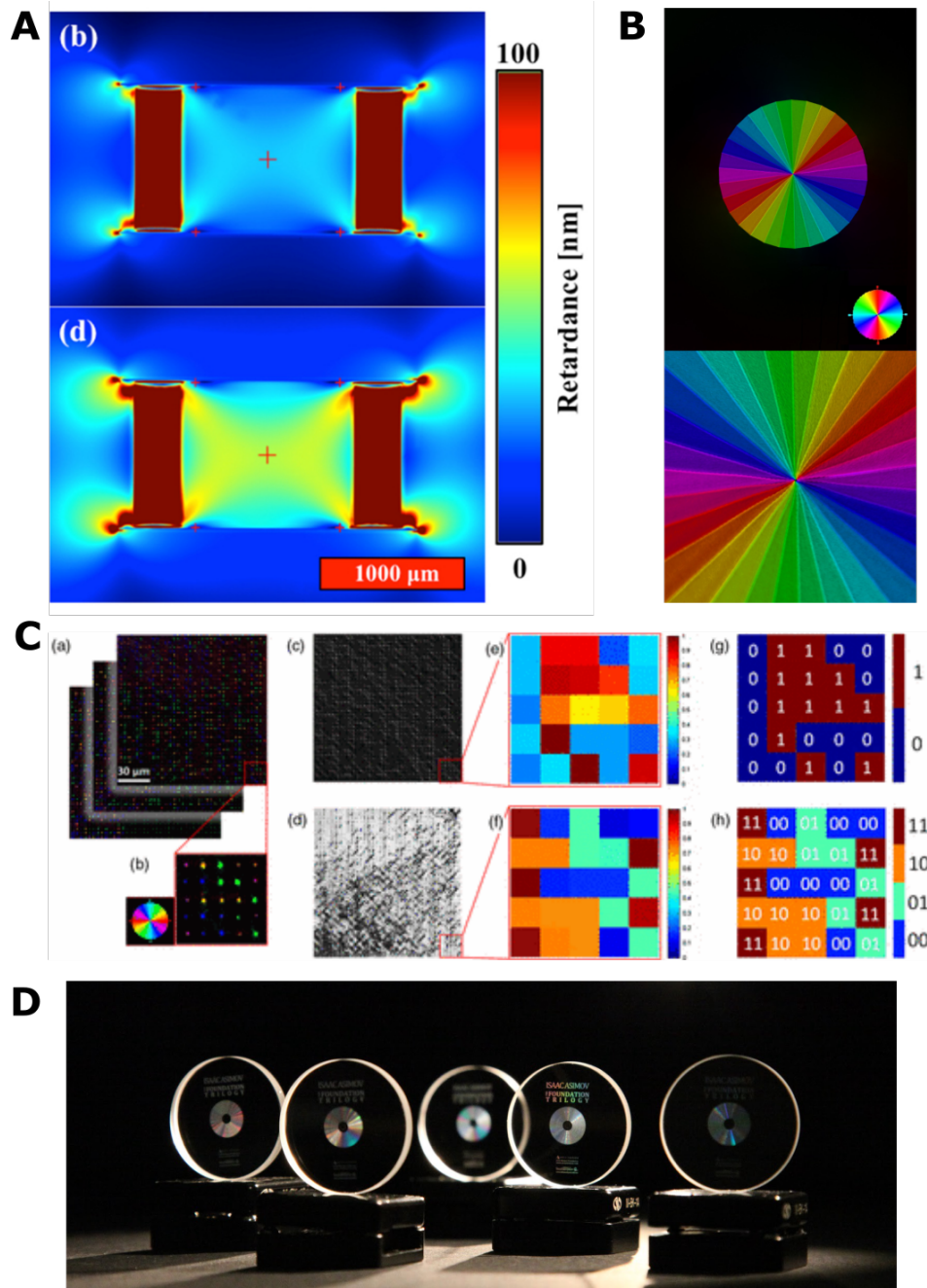
Figure 1.4: *Femtosecond laser inscribed retardance patterns (A and B) and their application for 5D data storage (C and D). (A) Stress-induced optical retardance pattern of two waveplates with a different number of 'stressors' [16]. (B) Color-coded retardance map of a radial polarization converter [15]. (C) 5D optical storage readout concept taking advantage of 3D inscription, intensity, and nanogratings orientation [35]. (D) Fused quartz discs containing the three books of the Isaac Asimov Foundation Trilogy (from Arch Mission Foundation).*

Figure 1.5: *Examples of micro-devices fabricated by femtosecond laser irradiation followed by wet chemical etching. (A) Scanning electron micrograph of a cross-pivot hinge [101]. (B) Schematics (top) and optical images (bottom) of a microfluidic device with a movable plate to switch flow direction [23]. (C) Scanning electron micrograph of a comb-array electrostatic micro-actuator [4]. (D) A monolithic gimbal micro-mirror fabricated and finely tuned with femtosecond laser [7].*
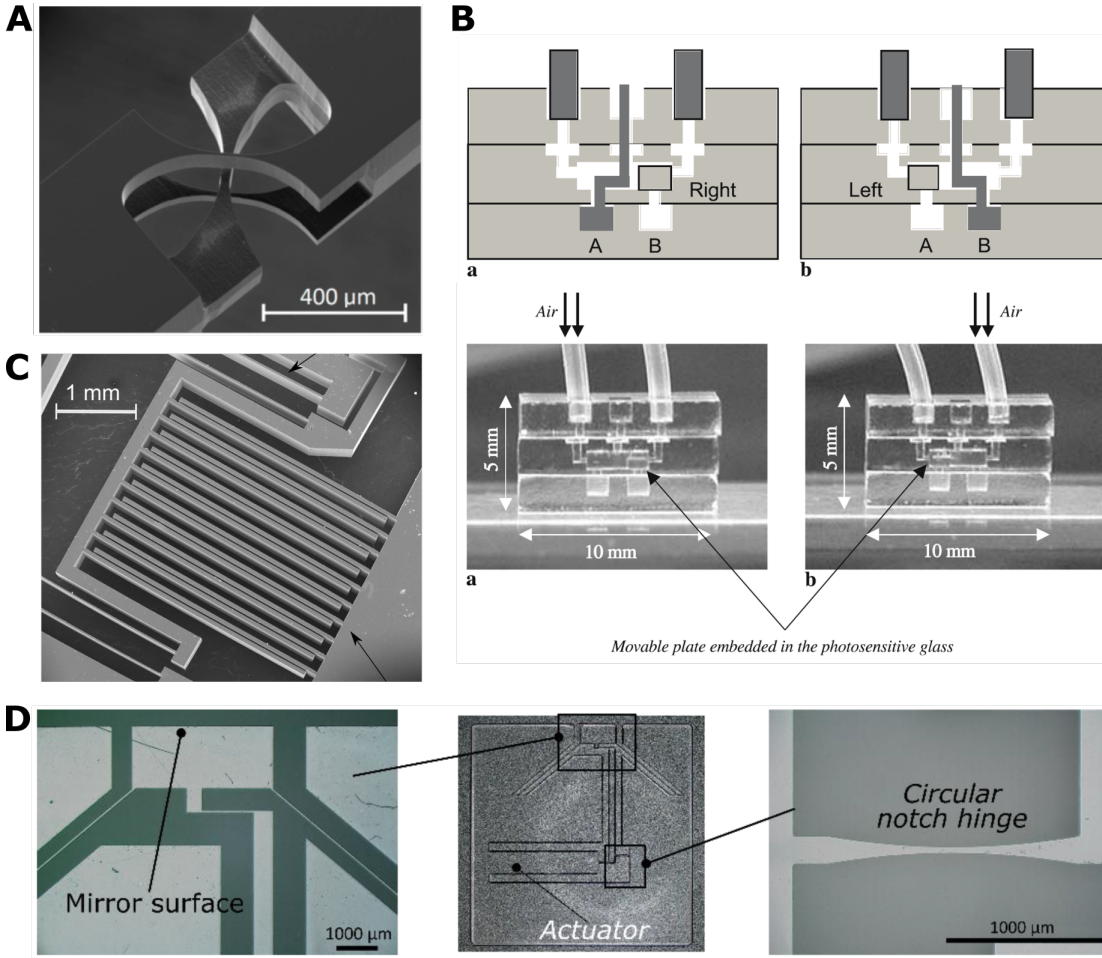
1.1.4 Monolithic multifunctional devices

The combination of Type I and Type II modifications enables the fabrication of multifunctional devices combining freeform waveguides with micromechanics [106] and/or microfluidic channels [107, 108] for numerous applications in the field of optical sensing and microbiology [29, 32, 33, 109]. In particular, the femtosecond laser technology has been extensively studied for lab-on-a-chip applications ranging for example from algae detection [33] to cell sorting [26–28], and trapping & stretching [30, 31]. Haque *et al.* demonstrated the fabrication of a lab-on-a-fiber [104], while with a combination of micromechanics and microfluidics Zanaty *et al.* presented a programmable eye-surgery device [105]. Figure 1.6 shows a few selected examples of multifunctional devices monolithically fabricated combining femtosecond laser glass micromachining and waveguide direct-writing.
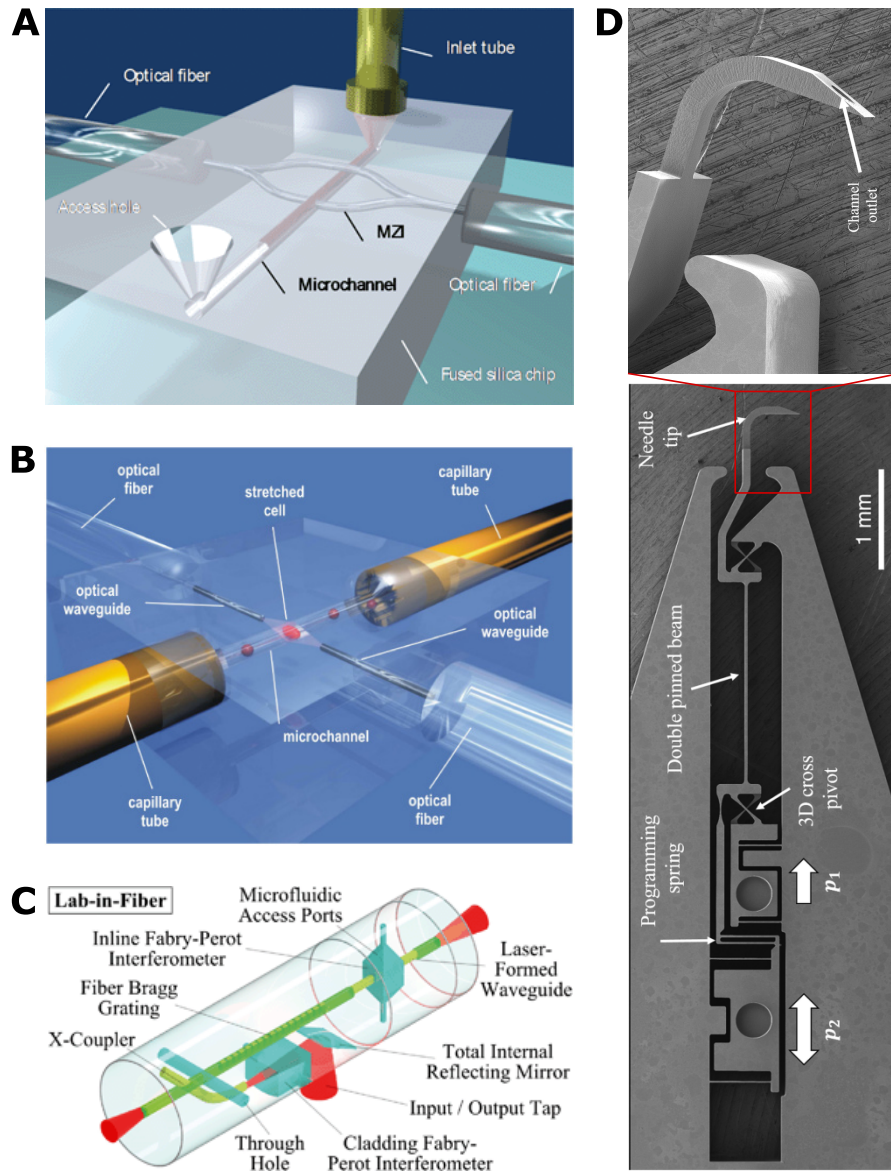
Figure 1.6: *Examples of multifunctional micro-devices fabricated by combining femtosecond laser Type 1 and Type 2 modifications. (A) Schematic of a microfluidic channel and an integrated Mach-Zehnder interferometer (MZI) for optical sensing [103]. (B) 3D representation of a monolithic device for cell trapping and stretching [30]. (C) Schematic of a lab-on-a-fiber indicating the different integrated optical elements [104]. (D) SEM micrograph of an eye-surgery device combining complex micromechanics and microfluidics. [105].*

Despite the remarkable progress in fabricating integrated monolithic devices in a single glass substrate, additional functions, such as electrical ones, require the combination of different materials. As an example, by embedding freeform metallic structures in the substrate, it would be possible to create arbitrary electric and magnetic fields distribution, which is of interest

for actuation or sensing. Likewise, combining different glass would enable the fabrication of high-index-contrast devices and/or with different spectral responses. Finally, combining 3D metallic structures with glass having high nonlinear Kerr coefficients would open up opportunities for miniaturized and geometrically complex electro-optic devices.

Towards this goal, we explore micro-infiltration techniques enabled by femtosecond laser glass micromachining and their capability to integrate 3D structures of different materials in a single fused silica substrate.

1.1.5   Summary

Let us summarize the key messages of the preceding paragraph *Ultrafast laser processing of transparent materials.*

- Femtosecond laser processing of glass is based on non-linear absorption phenomena, which allow to introduce modifications smaller or confined in the focal volume. Thanks to this process, 3D freeform writing of arbitrary patterns in the bulk of a substrate is possible.

- This laser-matter is generic and is compatible with various transparent substrates, being amorphous or crystalline.

- In fused silica, different types of modifications depending on the laser parameters can be introduced. Specifically, two main regimes are of particular interest in the functional integration: (i) *Type I - homogeneous densification*, to direct-write 3D integrated waveguides and other optical components; (ii) *Type II - nanogratings*, to integrate stress-engineered devices for phase retarders and high-density memory storage, and to fabricate 3D glass micro-components by preferential chemical etching of laser-modified regions.

- Type I and type II modifications can be effectively combined in the same substrate. This versatility of the process, together with the 3D freeform writing capability, enables the fabrication of monolithic multifunctional devices, combining optics, micromechanics, and microfluidics.

1.2 Multi-materials 3D structural integration

Rephrased in more generic terms, the objective of this study is to explore manufacturing techniques to integrate micrometric 3D structures of arbitrary materials inside another substrate. Specifically, and it will be developed further in this manuscript, we use femtosecond laser-enabled *micro-infiltration* processes to integrate arbitrary freeform structures of metals and infrared glass in a fused silica substrate.

In this paragraph, we introduce various casting techniques and explore how and why it is an interesting approach for micron-scale integration of devices in a single substrate. Note that in the sequel, we do not consider alternative processes based on lithography and deposition/galvanic growth as it is used for instance, in some processes based on LIGA patterning methods, be it with UV or Xray radiations. Unfortunately, these methods are intrinsically limited to 2.5D geometries and cannot be used to create complex 3D-structure embedded in a host substrate.

1.2.1 Introducing casting

Casting, and in particular metal casting, is one of the oldest manufacturing processes with evidence of its existence dating back from six millennia [110]. It became common in the early Bronze age in Mesopotamia [111]; since then, and throughout all ages of human civilization, casting has been an essential vehicle for technological progress as well as an important means of artistic expression. Metal castings – estimated today to be present in up to 90 % of all durable goods [112] – are therefore ubiquitous in our daily life.

Casting is a manufacturing process that consists of 3 main steps: (i) pouring or pushing a molten material (usually a metal, a thermoplastic, or a curing material) into a mold that contains a desired shape hollow cavity, (ii) solidifying the cast part - that will thereafter be called *casting*, and (iii) freeing the obtained part from the mold - a step also known as *demolding*. Such a technique is most often used for the production of complex geometries that would be complicated or uneconomical to produce by other methods and for heavy and large equipment to avoid the - otherwise required - production and joining of several smaller pieces [113]. Some of the casting processes, namely die-casting or variants such as metal injection molding are usually chosen for large-scale production, due to their scalability and repeatability. They provide flexibility both in terms of design (provided that the molds can be manufactured) and materials choice. Casting requires post-processing steps, for instance, to detach the castings from the mold or to improve surface finish, which can be poor depending on the casting technique used. Typical challenges related to casting are the dimensional accuracy, due to solidification and thermal shrinkage, the melting and handling of high melting point materials, and the possibility of having impurities and pores, that, together with the heat treatment forced on the cast material, can result in low strength products.

Over centuries, a large number of variations of this technique have been envisioned and, among those, we select the three main ones for which we provide a short description of the working principle and discuss their main advantages and disadvantages.
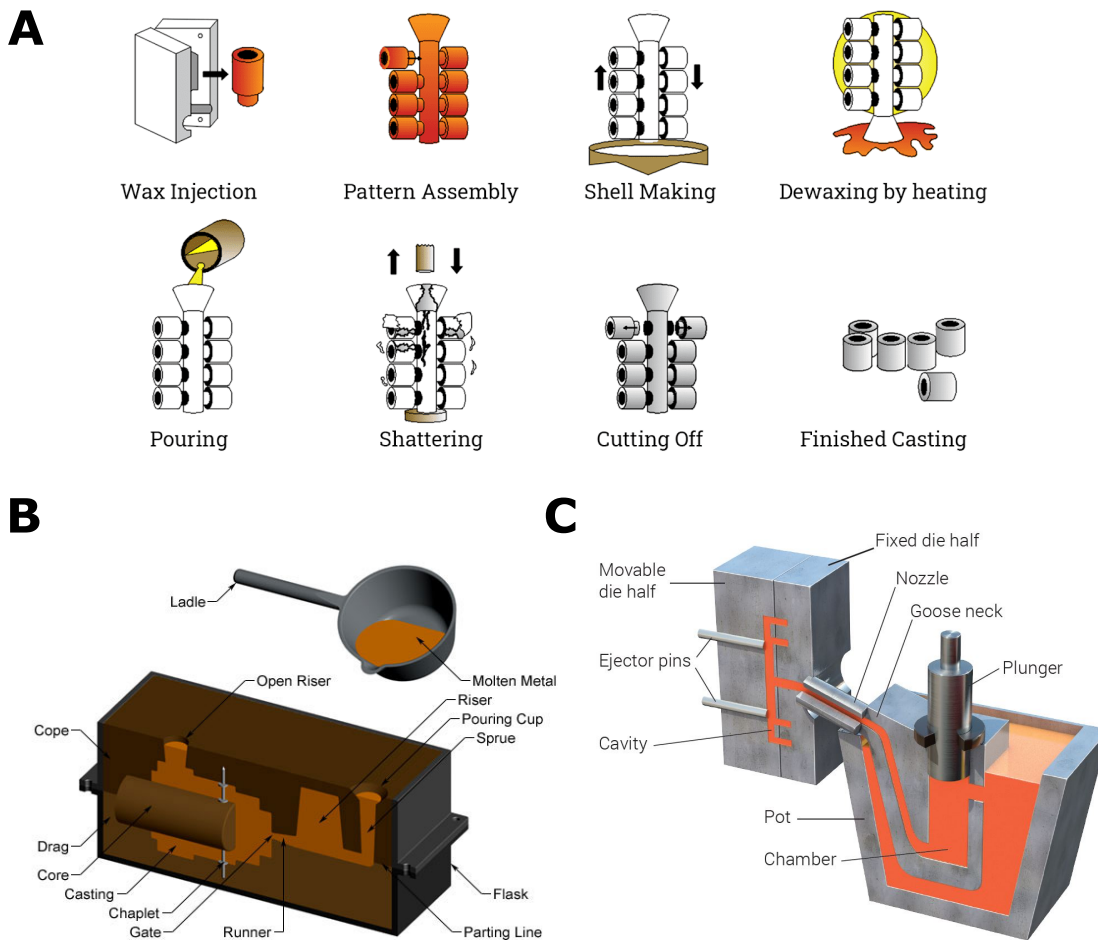
Figure 1.7: *Schematic of three main casting processes. (A) Investment casting (image from [114]). (B) Sand casting (image from [115]). (C) Die casting (image from [116]).*

Investment casting , shown in Figure 1.7 A, is also known as lost-wax casting and is one of the most ancient casting techniques. The process consists in (i) forming a wax pattern for example by molding with the so-called *master die*; (ii) assembling multiple wax patterns in a large part to achieve a batch pour; (iii) applying ceramic coatings until the desired thickness, achieving a mold (the *investment*) that envelops the assembled patterns; (iv) de-waxing the patterns by melting or vaporizing the wax; (v) pouring the molten infiltrant; (vi) shattering the ceramic mold; (vii) cutting of single patterns; and (viii) finishing the parts. Among the main advantages of this method are the excellent surface finish and the dimensional accuracy, even for intricate parts and the possibility to cast almost any metal [113]. The main drawback is the elevated cost due to the multitude of steps and the price of the ceramic coatings.

Sand casting , shown in Figure 1.7 B, is characterized by the use of sand (plus a resin binder) as the mold material and is the most common casting technique, accounting for over

the 60 % of all metal castings [117]. The process can be described in six steps: (i) a pattern is placed in the prepared sand compound to imprint the desired shape and thus, create a mold; (ii) the mold is cured to a more resistant ceramic state; (iii) two molds (as in shell casting) are combined in a flask and, if needed, a *core* is inserted; (iv) the molten metal is poured inside the mold; (v) after solidification, the casting is freed by breaking the sand mold; and (vi) post-processing steps are used to finalize the parts, for example removing *gate*, *runner*, and *riser*. Sand casting presents all the common advantages of other casting techniques, such as the production of large and/or complex shapes, flexibility on material selection, and low tooling and equipment cost. However, it produces parts with poor surface finish and tolerance and has a low production rate due to the complicated demolding.

Die casting, shown in Figure 1.7 C, is characterized by forcing the molten metal under high pressure in a mold cavity (the non-metal counterpart is commonly referred to as *injection molding*). The following four steps are traditionally identified in die casting: (i) two dies are prepared in a highly resistant material and lubricated; (ii) the dies are closed and a molten infiltrant is injected into the cavities by high pressure (10 to 150 MPa) and the pressure is maintained until solidification is reached; (iii) the casting is ejected from the mold; (iv) post-processing steps are used to obtain the final desired part. Die casting shows the highest surface finishing compared to other casting techniques and enables the recycling of the excess infiltrant by remelting it [113]. The casting equipment for high-pressure infiltrations and the production of the dies represent a large capital cost. As a consequence, die casting is commonly used for high-volume or high-end productions.

1.2.2 Bringing casting to the micron-scale

Moving from the macro- to the micron-scale, few technical challenges arise when attempting to transpose the same manufacturing concept while maintaining its advantages, namely multi-(engineering)materials compatibility, single-shot production of any intricate 3D geometry, scalability, and repeatability. The miniaturization of metal casting - and casting in general - apart from the challenge of preparing a precise 3D micrometric mold of a resistant material (ideally a ceramic), has been prevented by the dominance of surface effects over volume ones, contrary to what happens at the macro-scale. In fact, in micro-casting capillarity issues coupled with high atom-mobility rates interfere to disrupt the process. Specifically, (i) for poorly wetting materials (e.g. molten metals have high surface tensions and wet poorly nearly all ceramics [118]), capillary forces oppose infiltrant ingress into micron-scale mold cavities, and (ii) coupled with high atom mobility at elevated temperatures deform the surface of conventionally used crystalline precision molds. Capillary force equilibrium creates micron-scale depressions on the mold surface wherever crystal defects such as dislocations,

interfaces, or grain boundaries are present. Those depressions result - once infiltrated - in relatively large protuberances along the cast surface. (iii) When the process is carried on at high temperature, chemical reaction rates increase and it becomes fundamental that there is no chemical affinity between the mold's and the infiltrant's atoms. Finally, (iv) heating-cooling dynamics are radically different due to much higher surface-to-volume ratio and so lower thermal inertia than at the macro-scale.

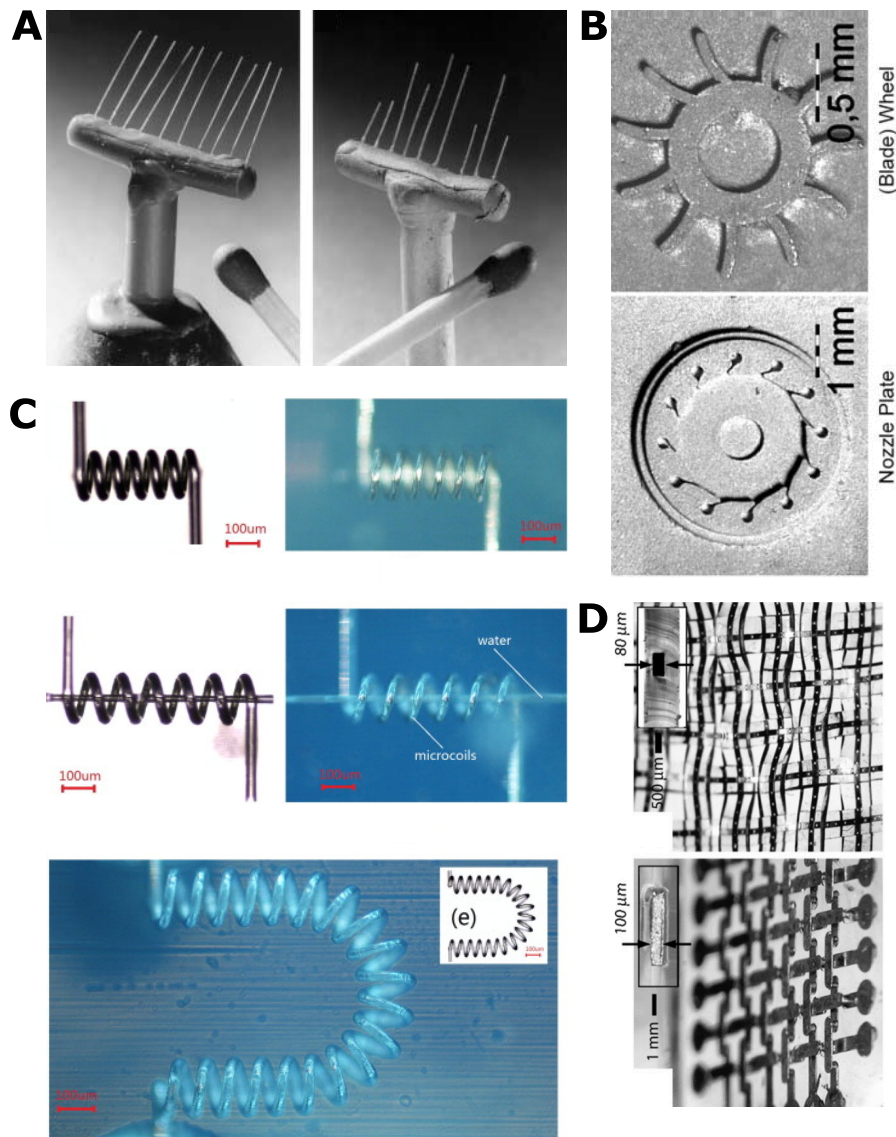Figure 1.8: *(A) Masterpiece used for the mold preparation (left) and vacuum pressure infiltrated part (right) made of a gold base alloy [119]. (B) Sub-centimeter-scale castings of turbine parts made of a gold base alloy [120]. (C) Infiltrated micrometric gallium coils integrated into fused silica molds together with a microfluidic channel. (D) Intricated grid structures made of solder metal infiltrated in a PDMS mold [121].*

As a prerequisite for implementing casting at the microscale, a manufacturing technology able to structure interesting molds materials in 3D is needed for the preparation of the mold. Then, to overcome capillary forces of poorly wetting molten infiltrants, one has to apply pressure to surmount surface tension and force the infiltrant into the mold cavities. Finally, to avoid the presence of crystal defects and unwanted chemical reactions, the material to produce the mold should be highly chemically- and thermally stable. Suitable candidates for this purpose are ceramics and glass, the latter having the additional advantage of not having any crystalline structure. Micron-scale variation of die-casting will be referred to as *micro-infiltration* in this thesis.

One of the first attempts to downscale casting was in early 2000 when Baumeister *et al.* infiltrated fibers with a minimum diameter of 100 μm (Figure 1.8 A - right) and few turbines part (Figure 1.8 B) with a gold base alloy by a variation of die casting labeled as vacuum pressure casting [119, 120]. These results proved that it was possible to cast metal 3D parts at the micron scale. However, the crystalline ceramic material of the mold and the investment casting technique used to produce it limited the average roughness to 1.13-0.27 μm and the minimum feature size to 100 μm. A different approach was developed in 2007 by Siegel *et al.* (see Figure 1.8 D), who poured liquid solder metals into poly(dimethylsiloxane) molds that are rendered wettable by the use of surface chemistry. With such a technique, intricate and flexible metallic structures with a minimum dimension of 50 μm were realized out of low melting point (< 250 °C) solder metals [121]. In 2014, a similar concept was used by Liu *et al.* to infiltrate Gallium into fused silica molds fabricated by femtosecond laser-assisted chemical etching [122]. This process shows an advanced 3D capability (see Figure 1.8 C), but cannot fill 'dead-end' channels and remains limited in terms of resolution. Further, while it can produce dense metal parts, it is notably limited to low melting point metals (e.g. gallium, indium, or tin), which are of limited engineering interest.

An alternative method for building metal structures into femtosecond laser micromachined cavities is based on electroless plating instead of infiltration (Xu *et al.* [123, 124]). Specifically, they take advantage of the higher surface roughness (compared to the optical quality roughness of the pristine substrate) of femtosecond laser ablated surfaces to have a selective metal deposition of copper and gold films [123] in the inside of 3D-shaped cavities. The method is demonstrated inside a photo-etchable glass (Foturan® from Schott). They also demonstrated the capability of this process to produce electrofluidic devices for manipulating (Figure 1.9 A) and moving (Figure 1.9 B) biological samples [123, 124]. While interesting, this deposition method is limited in terms of achievable geometries due to the need to post-processing the device by scanning the target surfaces to ablate them and locally increase their roughness. As a consequence, the deposited layers have a larger roughness than their counterparts machined by laser-assisted chemical etching and in turn, a poor mechanical stability [124]. More important, it is not possible with this method to produce dense metal parts. Furthermore, the deposition rates are limited to a maximum of 1.15 and 0.55 μm/h for copper and gold, respectively. In conclusion, despite being an interesting process for electrofluidic applications,

it cannot be compared to micro-infiltration in terms of the intricacy of the patterns, structural quality of the parts, and processing speed.
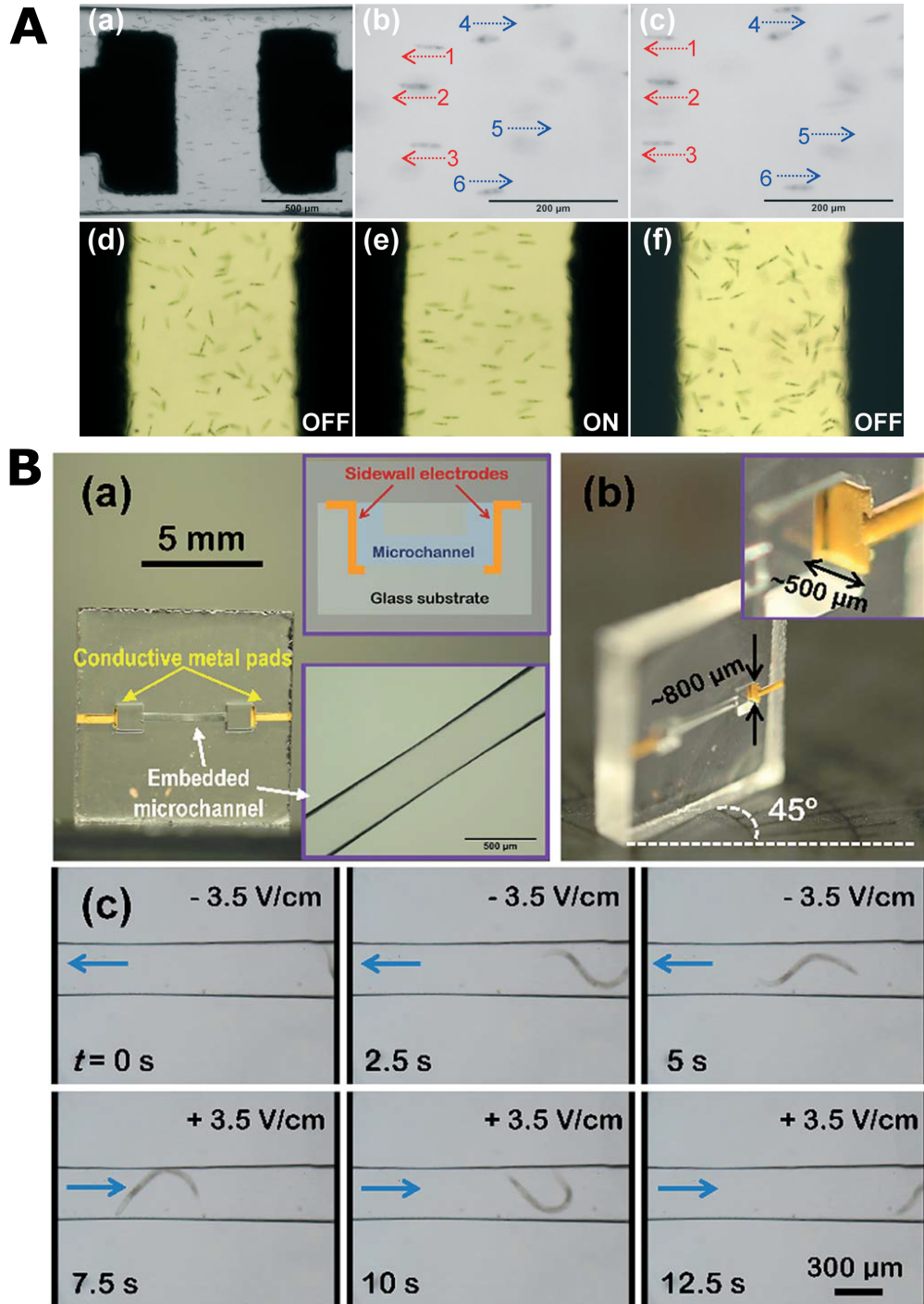

Figure 1.9: *(A) Electroorientation of Euglena cells in a microfluidic channel [123].(B) Electrofluidic glass chip to move a C. elegans worm along the direction of the electric field [124].*

1.2.3   Micro-infiltration

In the following sections, we focus on *micro-infiltration* and explore the main parameters involved and the various process' stages to achieve a functioning methodology.

1.2.3.1   Key parameters

A micro-infiltration process involves a multitude of parameters of importance for a successful implementation. In this paragraph, we introduce the main framework and discuss the influence of each item on the process.

Materials

The first specification regards the materials chosen, both as a substrate and as an infiltrant. The substrate material should ideally be amorphous, and hence microstructurally featureless, to avoid surface defects. It could theoretically also be crystalline if eventual protuberances along the cast metal surface are negligible. The infiltrant itself can either be amorphous or crystalline, but depending on the choice, it is fundamental to carefully define the cooling rate after infiltration to avoid or facilitate crystallization with controlled grains nucleation and growth. The materials selection defines the temperature and pressure ranges to be applied during infiltration. On one hand, the chosen substrate sets the temperature upper limit, i.e. the temperature should not overcome the substrate's softening point if made of glass, or if crystalline, its melting point. On the other hand, the infiltrant's softening or melting point (depending on its nature) along with its viscosity and surface tension (commonly inversely proportional to the temperature), defines the temperature and pressure needed for successful infiltration. Finally, the difference in coefficients of thermal expansion (CTE) between the substrate and the infiltrant determines the amount of stress build-up during cooling of the infiltrated components (assuming perfect adhesion at the substrate-infiltrant interface). It should be noted that such stress depends on the CTE difference, the difference between initial and final temperature, and the cooling rate when dealing with amorphous material. It does not depend however on the dimensions, but can be amplified, depending on the infiltrated geometrical shapes, in the proximity of stress concentrators, as for example a sharp corner.

Figure 1.10 presents an overview of (A) thermal expansion versus Young's modulus and (B) strength (i.e. elastic limit) versus maximum service temperature for commonly used materials [125]. In particular, the combination of these two graphs gives a birds-eye view of the regimes of stress and temperature in which each material (class) is usable and the order of magnitude of thermal expansion to expect. It should be noted that even the strongest polymers have a low elastic limit above 200 °C and at the same time a relatively large CTE (> 100 μm/(mK)); most metals become very soft above 800 °C and have a CTE of 5-35 μm/(mK); and only ceramics maintain high strength above 1000-1500 °C while presenting the lowest CTE of 0.4-10 μm/(mK).
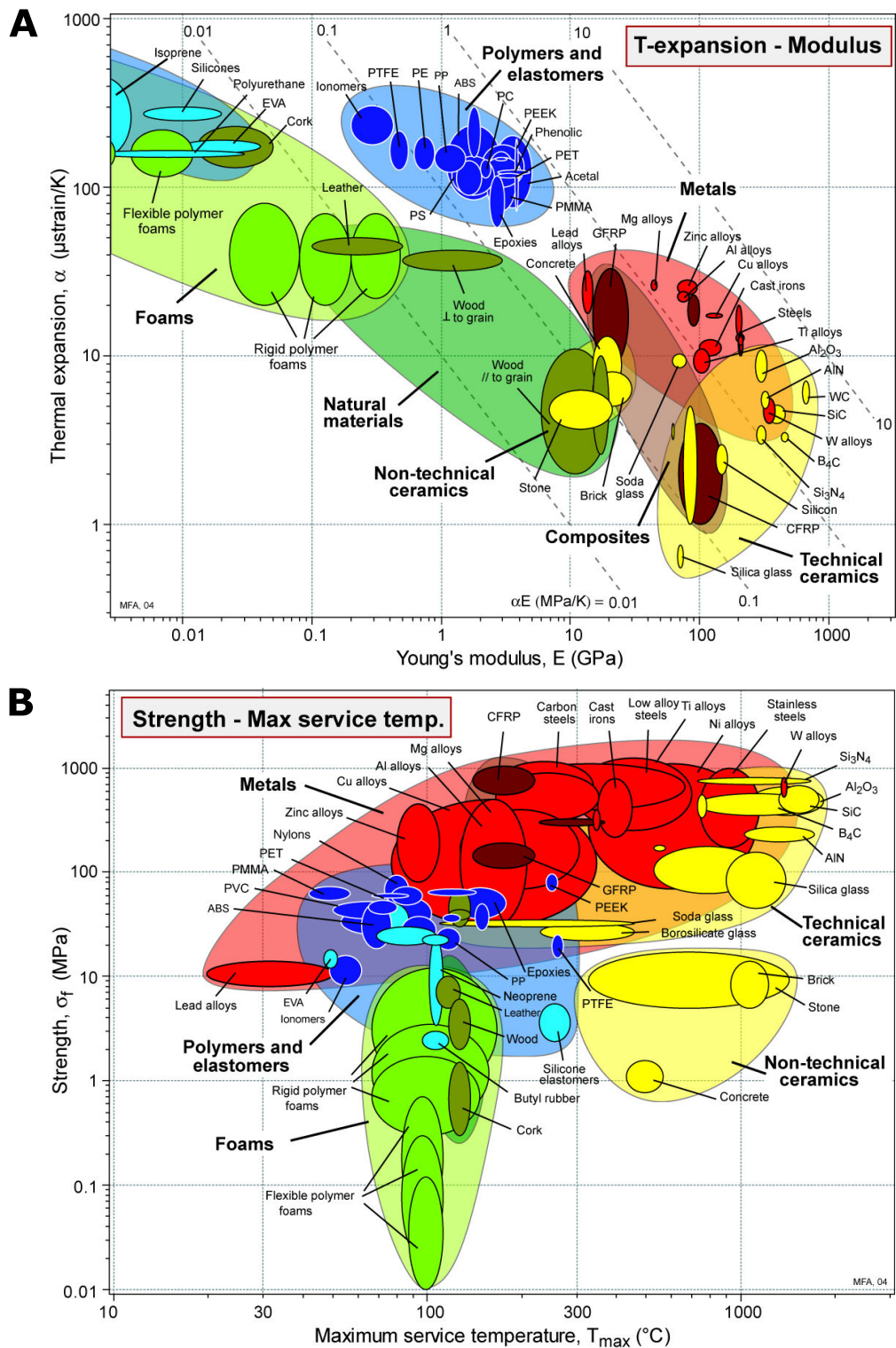
Figure 1.10: *Material selection charts (i.e. Ashby charts) representing (A) thermal expansion versus Young's modulus, and (B) strength versus maximum service temperature [125].*

In the context of micro-infiltration enabled by femtosecond laser processing, an optimal material selection combines (i) an amorphous and chemically stable substrate, with (ii) a low CTE mismatch between substrate and infiltrant to limit the amount of thermal stress during cooling. It further requires a substrate (iii) that maintains its strength at high temperature to enable the infiltration of more materials, (iv) high strength substrate and infiltrant to limit the possibility of plastic deformation or fracture of the casting or the mold under the eventual thermal stress originating during cooling, and (v) that is compatible with femtosecond laser micromachining to enable the preparation of geometrically complex 3D micron-scale cavities to be infiltrated.

In this thesis, the material selected as a substrate is fused silica, which presents a softening point of $\simeq 1200\,°$C, a CTE of $\simeq 0.5\,\mu$m/(mK), and Young's modulus of 72.5 GPa. Despite having one of the lowest CTE and in turn, a high CTE mismatch with potential infiltrants, fused silica is amorphous and presents a high Young's modulus, along with excellent thermal and chemical stabilities. It is also the most mature substrate for femtosecond laser micromachining. As infiltrants, we tested different noble metals with a melting point typically $\simeq 900$-1100 $°$C and a CTE around $\simeq 10-25\,\mu$m/(mK) and a chalcogenide glass with a softening point of $\simeq 200\,°$C and a CTE around $\simeq 22\,\mu$m/(mK).

Shape
The dimensions and shape of the cavities to be infiltrated play an important role in the definition of the process parameters. Primarily, the dimension of the smallest cavities' entry, together with the surface tension (γ) of the infiltrant, defines the minimum pressure required to overcome the capillary force and successfully infiltrate the cavities. To estimate the required pressure for infiltration, a few results from fluid dynamics can be considered.

In fluid dynamics, the so-called Eötvös or Bond number is used as a dimensionless measure of the importance of gravitational versus capillary forces:

$$Eo = Bo = \frac{\Delta \rho g L^2}{\gamma}$$

Where: $\Delta \rho$ is the difference in density of the two phases (kg/m^3), g is the gravitational constant (m/s^2), L is the characteristic length - i.e. in our case the channel width - (m), and γ is the surface tension (N/m). A large value of this number indicates a system dominated by gravitational forces (i.e. the entry is large and capillary forces are negligible); while a low value represents a system dominated by surface tension (i.e. the entry is narrow and gravitational forces are negligible).

The Young-Laplace nonlinear partial differential equation describes the capillary pressure across the interface between two static fluids, and in turn, defines the minimum pressure required to overcome the capillary force and successfully infiltrate the cavities. For a narrow or low Bond-number cavity of circular cross-section (see schematic in Figure 1.11 A), the

equation can be simplified as [118]:

$$\Delta \rho \approx \frac{\gamma}{L}$$

This simple formulation is used to estimate the pressure requirements. For example, considering the infiltration of metals, which commonly have surface tensions on the order of 1 J/m^2, a pressure of 1 MPa can achieve the infiltration of cavities as narrow as 1 μm, while with a pressure of 10 MPa, 100 nm can be achieved (note that pressures above 100 MPa are routinely used in conventional macro-scale casting).
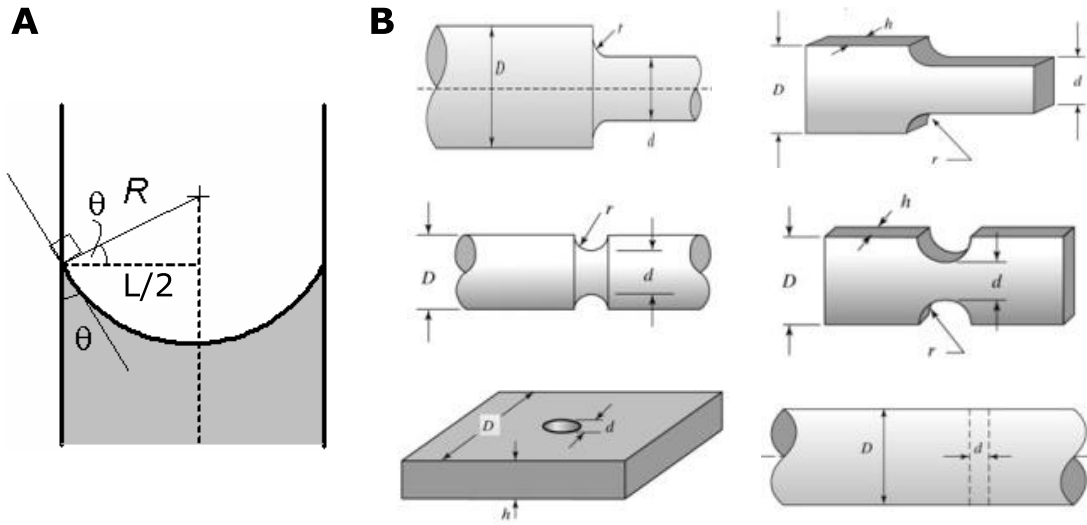
A

B

Figure 1.11: *(A) Schematic of a spherical meniscus with an acute wetting angle. (B) Few schematic examples of geometries (specifically, shoulder fillets and holes) causing stress concentration (image from [126]).*

After applying a pressure able to overcome the capillary forces of the narrowest cavity and if the viscosity of the molten infiltrant is low enough, the infiltration can theoretically proceed smoothly and almost unaffected by the shape and aspect ratio of the mold's cavities. However, during first, solidification, and later, cooling, the geometry of the infiltrated parts determines the shrinkage direction and the resulting thermal stress. In particular, two main issues may emerge: (i) solidification shrinkage creates voids and defects in the cast parts, and (ii) the thermal stress, magnified by stress-concentrating geometries (few examples are shown in Figure 1.11 B), becomes higher than the elastic limit of the materials or causes delamination of the infiltrated parts from its mold's surfaces. Note that these are common issues in casting independent of the scale of the mold. A common principle to control or avoid solidification is to force a directional solidification, for example by creating a reservoir of molten infiltrant that compensates the shrinkage while the solidification front advances. Stress concentrators can be limited by structural design and thermal stress can be dealt with careful control of the cooling strategy after solidification.

Chemistry

During the whole infiltration process, any chemical reaction should be avoided. Specifically, the infiltrant should be selected among compounds with an oxide less stable than the one of the mold (in our case silicon oxide). To evaluate the stability of different oxides in metallurgy, it is common to use the Ellingham diagram (shown in Figure 1.12) that displays the Gibbs free energy (ΔG) for each oxidation reaction as a function of temperature [127].
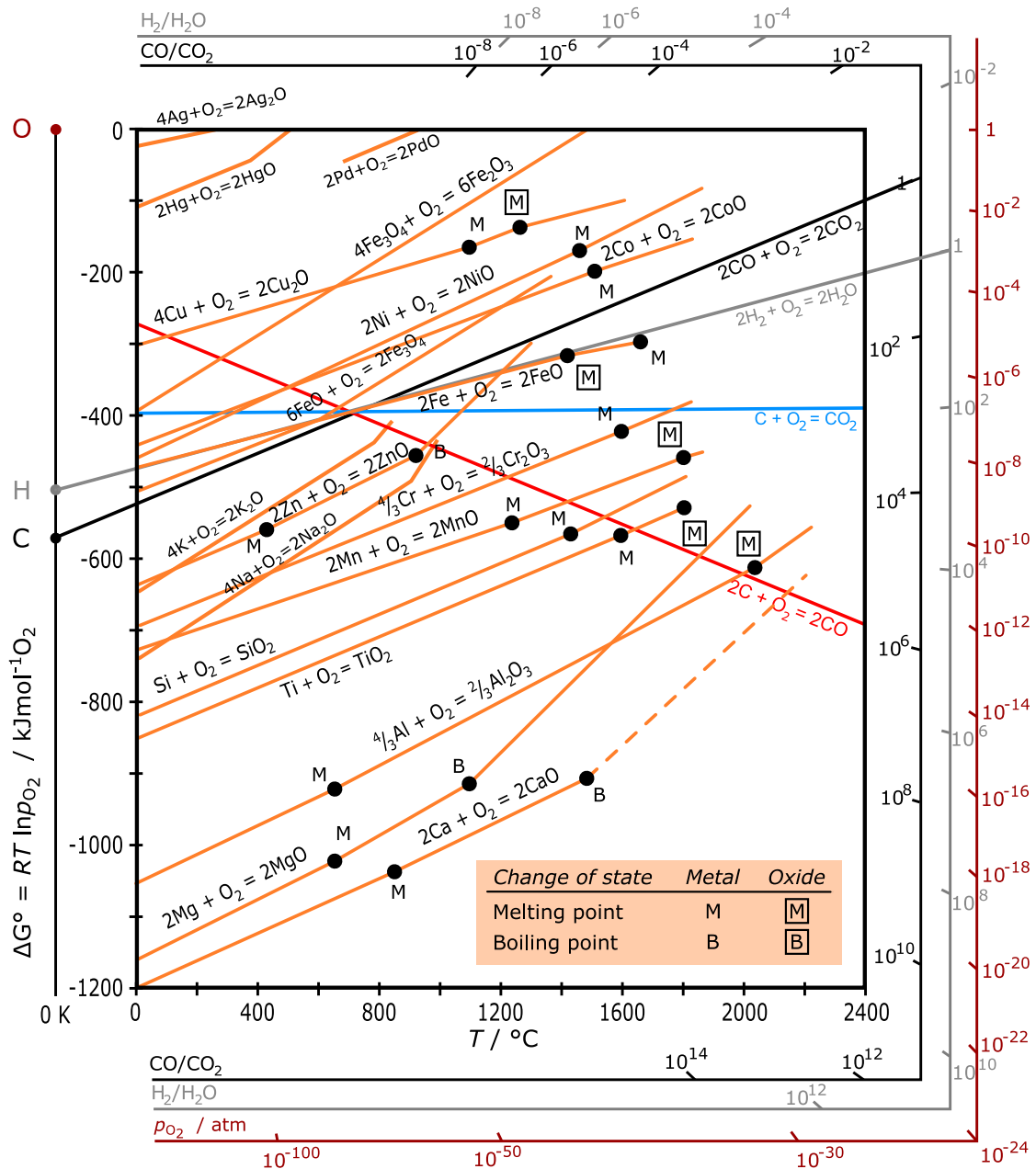

Figure 1.12: *Ellingham diagram, i.e. Gibbs free energy of formation of metal oxides and corresponding oxygen partial pressure at equilibrium, for several metals (image from [128]).*

In practice, the lower the position of a metal line, the greater the stability of its oxide. If two metals are compared at a given temperature, the metal with the lower Gibbs free energy of oxidation can reduce the oxide of the metal with higher Gibbs free energy of formation. For example, metallic aluminum - which forms one of the most stable oxides - can reduce silicon oxide to metallic silicon, while being oxidized to aluminum oxide. Finally, the wider the gap between the two lines, the more effective is the reduction reaction.

From Figure 1.12, it can be noticed that fused silica is among the lowest compounds in terms of Gibbs free energy and thus is chemically very stable. The only materials with even more stable oxides are titanium, aluminum, magnesium, and calcium. However, as of today, it is not possible to machine in three-dimensions at the micron-scale any of them.

The last considerations in terms of chemical stability concerns the infiltration chamber and eventual holders for mold and/or infiltrant. There too, any reaction should be avoided by choosing the appropriate materials. In the work presented here, graphite or fused quartz containers are used when infiltrating noble metals or chalcogenide glass, respectively.

1.2.3.2 Process stages

The process of micro-infiltration can be simplified to four main manufacturing stages: (i) the mold preparation, (ii) the pressure-assisted infiltration, (iii) the solidification and cooling of the infiltrant, and (iv) the demolding to eventually free the castings from the mold. The following sections describe these stages and indicate how each of them is related to the key parameters presented in the previous paragraph.

Mold

The first step, as in any casting technique, consists in preparing the mold. This can be approached by manufacturing either a masterpiece or a master mold of the required complexity, precision, and finishing. However, at the micron-scale, due to the increased capillary and surface tension forces, preparing a mold starting from a masterpiece can become extremely complicated, if not impossible, since thin features of the final part could be bent or fractured during the shell making (for investment casting) or the sand imprinting (for sand casting). Therefore, the remaining option is to directly manufacture the master mold. Then, after the infiltration of the castings and depending on its design and cost the mold can be either destroyed (as done in investment and sand casting) or disassembled for re-use (as in the case of die casting).

The production of a geometrically complex piece at the microscale can be achieved with different innovative 3D printing techniques such as selective laser sintering (SLS), two-photon polymerization, and femtosecond laser-assisted chemical etching. However, considering the need for the mold material to be highly stable, both chemically and thermally, polymers have to be excluded as well as most metals, which tend to have a relatively low maximum service temperature and chemical stability.

In this work, we explore femtosecond laser micromachining followed by chemical etching

as a method to prepare fused silica molds with complex cavities.

Infiltration

The second step is the infiltration of a molten infiltrant inside the prepared mold. At the microscale, the molten infiltrant needs to be forced by applying pressure to overcome capillary forces, for example with a mechanical *plunger* as in die casting, or by pressurized inert gas as in this work. The pressure and temperature needed are defined by the minimum feature size to be infiltrated and the viscosity and surface tension of the material.

Another important consideration is the atmosphere to be used during infiltration. In particular, the presence of air would not only prevent the infiltration of dead-end cavities as pockets of trapped gas would form, but could also initiate chemical reactions at elevated temperature or create porosity (particularly detrimental for fatigue resistance) in the castings. To prevent all these possible issues, the infiltration should be carried on under vacuum and the eventual pressurized inert gas used to force the infiltration should be gently released in the chamber.

Finally, the infiltration chamber should be designed taking into account the chemical reactivity of all the components involved in the manufacturing process to avoid contaminations and unexpected chemical reactions.

In this work, we achieve the melting of the infiltrant under vacuum. We then use pressurized argon gas to force the molten infiltrant inside the cavities. The elements in contact with the mold and/or the infiltrant are produced out of graphite or fused quartz to avoid any possible chemical reactions.

Solidification

The third step consists in controlling the solidification and cooling of the infiltrated parts. As in conventional casting, challenges such as solidification shrinkage and thermal stress are omnipresent during this stage and can be mitigated by applying known engineering recipes for larger-scale casting.

Solidification shrinkage indicates a volume change due to the liquid-to-solid phase change of the infiltrant. It is prevented, or at least limited, (i) by designing running systems with risers that ensure a continuous flow of liquid infiltrant, (ii) by inserting chills and imposing local heat dissipation to obtain a directional solidification, and (iii) by implementing shrinkage allowances into the pattern design before casting.

Thermal stress arises after solidification, during the cooling of both the mold and the infiltrant. In particular, the two materials (infiltrant and mold) generally have different coefficients of thermal expansion and thus, shrink at different rates. Thermal stress is proportional to both temperature and CTE difference. Thus, the larger the CTE mismatch or the temperature, the greater the stress will be. Intuitive solutions to limit this effect consist in choosing (i) materials with low CTE mismatch, and/or (ii) a low melting/softening point infiltrant. Alternatively, when the choice of materials cannot be further optimized, careful control and design of the cooling curves, as well as possible post-infiltration annealing steps, can promote thermal stress relaxation.

In this work, the chosen mold material is fused silica that has an extremely low CTE and for which infiltrants with melting points up to 1100 °C are tested. As a consequence, thermal stress cannot be avoided and needs to be taken into account. A controlled cooling rate and the implementation of annealing steps often prevented the development of catastrophic stress levels that compromise the integrated final device.

Demolding

The fourth step is called demolding, namely the release of the casting(s) from the mold. In certain cases, such a stage is not needed, because the infiltration is used to integrate an additional component inside a substrate that needs to be preserved. If instead, the objective of the process is the production of free-standing castings, the mold can either be opened to release the infiltrated products and then, be re-used, or carefully shuttered or dissolved without damaging the final products. In both cases, this process can be consuming in terms of time and labor-intensive.

In this work, the castings are usually components to be integrated into a fused silica substrate, however, when needed, the demolding step is achieved by dissolving the glass mold in a high-concentration hydrofluoric (HF) bath. Note that this strategy is only applicable if the castings are made of materials inert to the acid solution, for example, gold and silver.

1.2.4   Summary

This section summarizes the key messages of this paragraph *3D multi-materials structures integration*, with a special focus on micro-infiltration.

- Casting, and in particular, vacuum pressure-assisted infiltration is a scalable and repeatable manufacturing process that is compatible with a multitude of substrates and infiltrants. Quasi-final low-roughness structures with almost any level of intricacy can be produced efficiently both in terms of cost and time. All those advantages make it a perfect candidate for integrating 3D multi-materials structures in a single substrate.

- The main challenge of casting is dealing with shrinkage. On one hand, solidification shrinkage can create pores and defects in the castings; on the other hand, thermal shrinkage, coupled with the difference in CTE between mold and infiltrant, creates thermal stress that can ultimately induce cracks nucleation, leading to the failure of the product.

- To downsize casting to the micron-scale, four main challenges have to be faced: (i) producing a precise 3D micrometric mold out of a thermally-resistant material, (ii)

forcing often poorly-wetting molten infiltrants in the mold's cavities against capillary forces, (iii) avoiding conventionally used crystalline precision molds (and in turn surface deformations in the proximity of any crystalline defect), and (iv) preventing chemical reactions among the components even at high temperatures.

- Up to date micron-infiltration techniques are either restricted in resolution to 100 μm or can only be applied to low melting point metals, which are of limited engineering interest. Other techniques based on deposition - and aiming at integrating 3D structures of different material into a substrate - are instead confined to thin metallic layers of low geometrical complexity.

- To achieve high-resolution micro-infiltration applicable to a broad range of materials, the mold needs to be stable, both thermally and chemically, and at the same time maintain mechanical properties at high temperatures, which further restrict the choice among the possible class of materials.

- Having in mind the constraints enunciated above, the most appropriate materials to use as a mold, by order of increasing stability, are silicon oxide, titanium oxide, aluminum oxide, magnesium oxide, and calcium oxide. Among those, silicon oxide is to date the most promising, considering its compatibility with a highly efficient 3D-manufacturing process (specifically, femtosecond laser-assisted chemical etching).

- The micro-infiltration of poorly wetting materials (almost all molten metals with ceramics) requires vacuum pressure infiltration. The required pressure can approximately be defined as the ratio of the surface tension over the channel width. For example, for metals a pressure of 1 MPa can infiltrate cavities of 1 μm, 10 MPa cavities of 100 nm, and theoretically 100 MPa (about the pressure used in conventional macro-scale casting) cavities as narrow as 10 nm.

1.3 Objectives and thesis outline

In this thesis, we *investigate new ways enabled by femtosecond laser micromachining of glass to integrate complex geometries of different materials, in particular glass and metals, in a single fused silica substrate.* We focus our research on the miniaturization of pressure-assisted casting and we explore its capabilities at the micron scale. We use femtosecond laser-assisted chemical etching as a technique to manufacture fused silica molds. In this context, and to further optimize the mold fabrication process in particular in terms of aspect ratio, we study the origin of femtosecond laser-induced etching selectivity.

Specifically, the objectives are:

1. To investigate the origin of femtosecond laser-induced etching selectivity for process optimization.

2. To explore micro-infiltration techniques to infiltrate freeform metal structures in pre-machined glass substrates for 3D metal parts micro-manufacturing, glass-metal composite fabrication, and 3D integration of metal-parts in a glass substrate.

3. To demonstrate micro-infiltration techniques to infiltrate infrared glass in a pre-machined fused silica substrate for 3D micro-optical composite components fabrication.

Beyond this first introductory chapter, the thesis is composed of four additional chapters:

Chapter 2 , based on [98], addresses our investigation of femtosecond laser-induced etching selectivity, and studies the effect of both laser parameters and etching solutions on the etching rate and the maximum achievable aspect ratio.

Chapter 3 , based on [129], presents micro-infiltration techniques for the freeform fabrication of metal micro-components, glass-metal composites, and metal architectures integrated into a glass and explores their potential and limitations.

Chapter 4 , based on [130], shows how to apply the developed micro-infiltration technique to integrate freeform infrared glass components in a more stable and resistant glass substrate and illustrates the process capabilities, by demonstrating the infiltration of chalcogenide glass in fused silica molds.

Chapter 5 offers a summary of the main results of this work and proposes a few possible follow-up research directions.

2 High efficiency 3D glass micromachining

Advanced three-dimensional manufacturing techniques are triggering new paradigms in the way we design and produce sophisticated parts on demand. Yet, to fully unravel its potential, a few limitations have to be overcome, one of them being the realization of high-aspect-ratio structures of arbitrary shapes at sufficiently high resolution and scalability. Among the most promising advanced manufacturing methods that emerged recently is the use of optical non-linear absorption effects, and in particular, its implementation in 3D printing of glass based on femtosecond laser exposure combined with chemical etching. Here, we optimize both laser and chemical processes to achieve unprecedented aspect ratio levels. We further show how the formation of pre-cursor laser-induced defects in the glass matrix plays a key role in etching selectivity. In particular, we demonstrate that there is an optimal energy dose, an order of magnitude smaller than the currently used ones, yielding to higher process efficiency and lower processing time. This research, in addition to a conspicuous technological advancement, unravels key mechanisms in laser-matter interactions essential in chemically-based glass manufacturing and offers an environmentally-friendly pathway through the use of less-dangerous etchants, replacing the commonly used hydrofluoric acid.

2.1   Laser-assisted etching of fused silica

Laser-based method for fabricating three-dimensional structures at micro/nano-scales has been a long-time endeavor embraced by researchers since the 80s. From advanced stereolithographic concepts [131, 132] to the reporting of sub-laser wavelength resolution in polymers [133, 134], it rapidly expanded towards glass materials at the turn of the millennium, with the demonstration of micron to sub-micron femtosecond laser processing of glass [2, 3, 19, 135]. This two-step process consists of first, exposing a substrate to femtosecond laser irradiation to define patterns of arbitrarily shapes throughout the material volume, and second, placing the substrate in an etchant that dissolves laser-exposed volumes. The laser does not remove any material but instead locally modifies it, introducing self-organized nanostructures [64] consisting in a series of nano-planes parallel one to another that are preferentially etched according to their orientation [21]. Contrary to laser-induced photopolymerization that defines the final shape of the object by direct-laser writing, the glass-based exposure-etching method is a negative process as the laser-exposed volume is removed, and what is left is the non-exposed region. As a result, while sub-wavelength resolution exposure patterns can be imprinted using just-above-the-threshold pulse energies, the ultimate feature size and process capability depend not only on the chemical etching selectivity between laser-affected zones and non-affected ones but also on the etchant diffusion process since its concentration is depleted as it infiltrates the material through the laser-exposed volumes. Achieving the highest possible aspect ratio with the smallest possible feature sizes is therefore directly correlated to the ability to produce laser-modified zones exhibiting the highest possible etching rate enhancement with respect to the etching rate of the pristine material, and yet, with the lowest possible pulse energies so that the non-linear affected zone remains the smallest possible.

To date, two chemical solutions have been reportedly used. The first one consists of using a

low-concentration (typically 2.5 to 5 %$_{vol}$), room-temperature-bath of hydrofluoric acid (HF) [3], while the second is to use a high molar concentration solution (8 to 10 M) of potassium hydroxide (KOH) brought at a temperature between 80 and 90 °C [97]. While HF achieves etching contrast in the order of 1:50 to 1:100, KOH exhibits significantly higher values [136]. Both methods pose difficulties in terms of implementation, not only for the operators' safety but also in terms of environmental impact. HF acid is one of the most hazardous acids to manipulate and requires specific recycling procedures. KOH, like all alkali metal hydroxides, remains highly corrosive and hazardous when used at high concentrations.

Here, we investigate sodium hydroxide (NaOH) as an etching solution. Our observations demonstrate an etching contrast, four and two times higher than HF and KOH, respectively. The highest etching rate with NaOH is also observed for very low net exposure doses ($\simeq$ 1.5 J/mm^2), an order of magnitude lower than the ones conventionally used. This specific observation enables ten-fold accelerated laser-exposure velocity than the current state of the art [137] as fewer overlapping pulses are required. We further demonstrate that at least in the very low exposure dose regime, etching enhancement mechanisms by HF, NaOH, and KOH are driven by the presence of defects such as non-bridging oxygen hole (NBOHC) and oxygen deficiency centers (ODC), and not primarily by the presence of nanogratings [25].

2.2   Experimental protocol

Fused silica substrates (Corning 7980 0F, OH 1000 ppm, 1 mm-thick, and 25 mm-square) are exposed to a femtosecond laser in a regime where no ablation occurs. In practice, we use a Ytterbium-fiber amplifier laser (Yuzu from Amplitude), emitting 270 fs-pulses at a wavelength of 1030 nm and a constant repetition rate of 333 kHz, chosen far-away from the regime where thermal accumulation is observed ($\simeq$ 1 MHz). Laser-exposure patterns are written by translating the substrate with linear stages (PI-Micos, UPS 150) under a 0.4-numerical aperture microscope objective that focuses the beam down to a measured optical waist of 1.94 μm. The etching rate efficiency is assessed by measuring the etchant progression in straight line patterns passing through the entire specimen and buried under the material surface at a fixed depth of 70 microns. A digital microscope (Hirox KH-8700) is used to measure the length of the etched patterns after an etching time of four hours for the three etchants considered here.

Lines-patterns are written in back and forth directions, and under two different linear polarization states, aligned and perpendicular to the writing direction, respectively. The pattern lengths are chosen to exceed the actual specimen size to exclude acceleration and deceleration phases of the moving stages, ensuring a constant cruising speed and hence, a constant exposure dose throughout the specimen.

Although near the absorption threshold (found at pulse energies of $\simeq$ 160 nJ), the laser-pattern width at the focal point can effectively be smaller than the spot size itself (due to non-linear absorption effects), in what follows, for comparative purpose, we use the optical beam waist as the metric for calculating the net laser exposure dose (or deposited energy)

according to the following formula [137]:

$$\Phi = \frac{4 E_p f}{\pi \omega v} \tag{2.1}$$

Where Φ is the exposure dose (in J/mm^2), f the repetition rate of the laser (in Hz), ω is the optical beam waist (in mm), v is the velocity of translation of the substrate (in mm/s) and Ep the pulse energy (in J).

A quantitative comparison between hydrofluoric acid (HF, 2.5 %$_{vol}$), potassium hydroxide (KOH, 45 %$_{wt}$), and sodium hydroxide (NaOH, 5 %$_{wt}$) as chemical etchants is performed. HF etching is carried at room temperature, while KOH and NaOH etching are performed at 90 °C. Six different pulse energies are explored from 160 to 260 nJ (with a step of 20 nJ), spanning across a region where the laser modified zone stretches from $\simeq 6$ μm to $\simeq 17$ μm along the laser propagation axis. These pulse energy conditions correspond to a pulse-irradiance at the focus $\Psi = E_p / (\Delta t \pi \omega^2 / 4)$, where Δt is the pulse duration (in s), of $\simeq 200$ to $\simeq 326$ GW/mm^2.

For each pulse energy, the exposure dose or net fluence is varied 30 times between $\simeq 0.5$ and $\simeq 100$ J/mm^2 by tuning the laser-scanning speed between 0.5 and 85 mm/s while keeping the repetition rate constant (333 kHz). The samples are cut into two perpendicularly to the sets of lines to expose the laser affected zones directly to the etchant, avoiding the beam-clipping effects that occur on the edges of the specimens. In this fashion, two samples are produced for each specific combination of parameters for statistical purposes. Comparison between etching solutions: HF, KOH, and NaOH.

2.3   Effect of pulse energy

Figure 2.1 shows the etching rate comparison of the three etchants for a given set of pulse energies and as a function of the exposure dose for a fixed polarization, chosen perpendicular to the writing direction. This polarization is reportedly the one that leads to the highest etching rates [21].

The three etchants follow a similar overall trend, with noticeable and significant differences in the moderate pulse energy regime, found around 240 nJ. For the near-absorption threshold pulse energy ($\simeq$160 nJ), a single peak of etching efficiency is observed at doses around 10 J/mm^2, followed by a decay. There, the three etchants display a remarkably identical etching efficiency, with NaOH decaying at a faster rate towards higher doses. This trend - a sharp increase followed by a decay - is consistent with what we reported in [137].

As the pulse energy is further increased, we observe the gradual appearance of a second peak at significantly lower doses, centered on 1.5 J/mm^2. While this peak eventually reaches the same amplitude that the one at 10 J/mm^2 for HF, it is double in magnitude for the bases, KOH and NaOH. In general, NaOH and KOH etching efficiencies are higher than HF for nearly all the exposure doses, with NaOH reaching the highest recorded etching rate value of >300 μm/h, about four times more than for HF and twice more than KOH under similar exposure conditions. Figure 2.2 shows the sets of lines written with 260 nJ of pulse energy after etching.
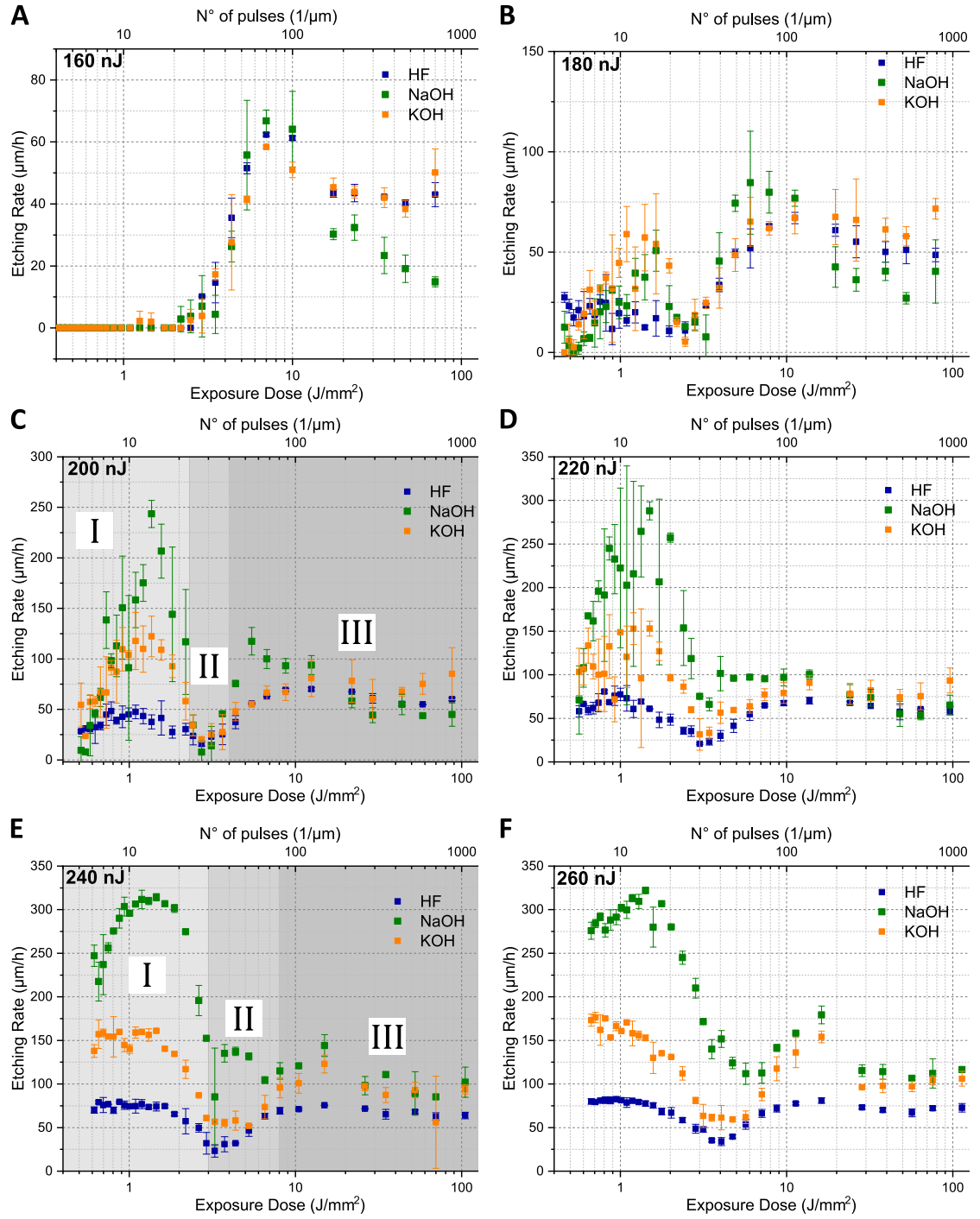
Figure 2.1: *Etching rate versus exposure doses for three different etchants: HF 2.5 %$_{vol}$, KOH 45 %$_{wt}$, and NaOH 5 %$_{wt}$. Six different pulse energy levels are explored: 160 nJ (A), 180 nJ (B), 200 nJ (C), 220 nJ (D), 240 nJ (E), and 260 nJ (F). In each graph, the squares represent the mean value and the bars the standard deviation for the two measurements performed.*
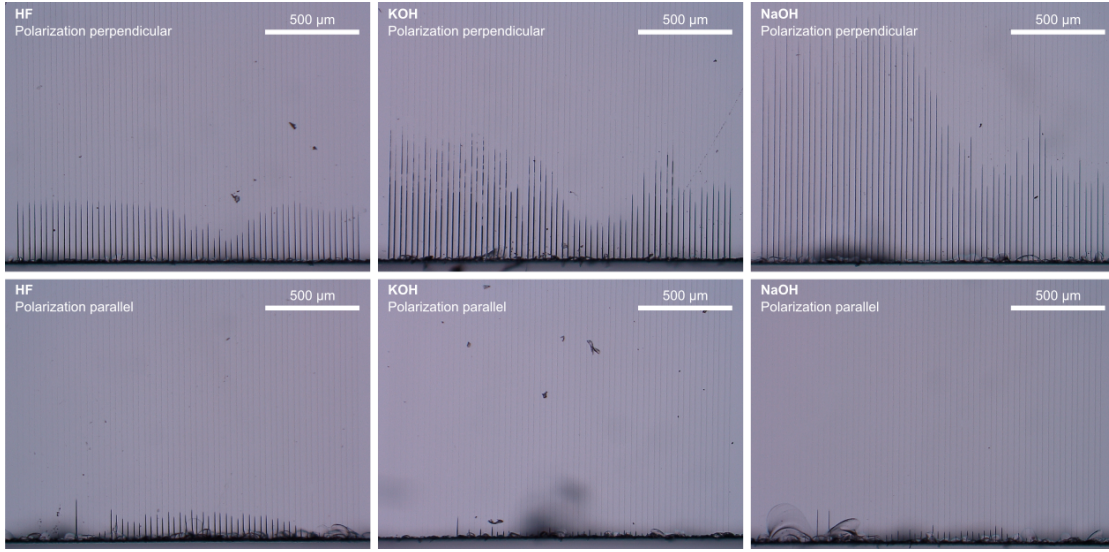
Figure 2.2: *Optical microscope image of the sets of lines written with 260 nJ of pulse energy for both polarizations after 4 hours of etching with HF, KOH, and NaOH. For each image, the exposure dose increases from left to right.*

A salient feature, common to all three etchants, is the presence of a valley, where the etching rate efficiency significantly drops before recovering to higher values. This region is consistently found around 3-4 J/mm^2 and defines a transition zone, signaling a dramatic change in the mechanism promoting an accelerated etching in laser-affected zones between low (1.5 J/mm^2) and high (10 J/mm^2) exposure doses. It is remarkable to observe that the highest etching rate is observed at the lowest doses, where only a few pulses overlap, in a number not sufficient for the formation of clear distinguishable nanogratings to be observed [86, 93].

Figure 2.3A shows the lines aspect ratio, i.e. the ratio between the measured etched length and the width at the entrance point of the etched tunnel (see inset of Figure 2.3C), for the two characteristics etching rate peaks ($\simeq$ 1.5 J/mm^2 and 10 J/mm^2, respectively) defining local maxima, for the three etchants and each pulse energy. While HF seems to show a weak dependence on the pulse energy, both KOH and NaOH show a clear maximum around 220-240 nJ. This maximum is particularly pronounced for NaOH - where an impressive aspect ratio approaching 400 is observed, while it does not exceed 100 and 50 for KOH and HF respectively (consistently with what previously reported in [97, 137]). To visualize the difference between the etchants, grid structures are laser-inscribed and etched for around 18 hours and shown in Figure 2.3B. Here the access for the etchant is defined by a vertical plane that intersects the lines. It is clear that NaOH and KOH etch the laser-modified lines faster and are more affected by the laser polarization than HF and, at the same time, NaOH is the most selective of the three.
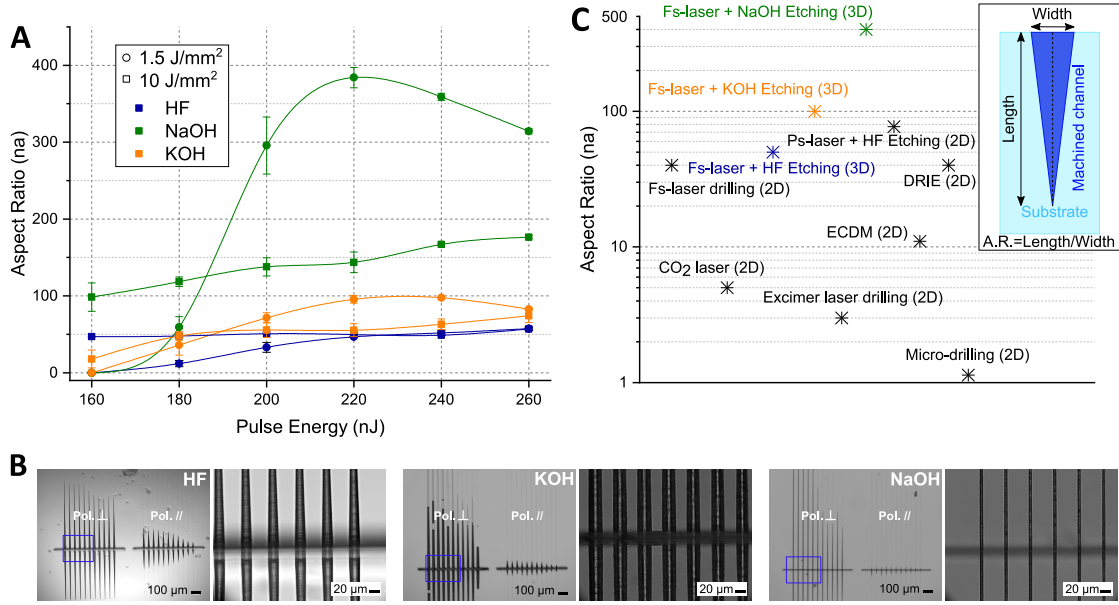
Figure 2.3: *(A) Aspect ratio of the etched lines at two characteristic exposure doses, for the three etchants and six different pulse energies. (B) Visual comparison of the etching progress for different laser parameters depending on the etchant used after 18 hours. (C) Comparison of the aspect ratio obtainable with various subtractive glass micromachining techniques. In the inset, a schematic of the aspect ratio definition used.*

Finally, in Figure 2.3C the performance of the most common subtractive glass micro-manufacturing methods are compared, taking as reference the highest aspect ratio values reported in [97, 137–146]. The presented version of femtosecond laser-assisted chemical etching with NaOH stands out in terms of aspect ratio and unlike all the other techniques mentioned, enables the manufacturing of arbitrary 3D geometries, and this, independently from the etchant chosen.

Each etchant naturally etches pristine fused silica, albeit at different rates. For similar etching conditions as in here, it is typically about $\simeq 3$ μm/h for HF [8], it is about three times less for KOH ($\simeq 0.9$ μm/h) [17] and only $\simeq 0.5$ μm/h for NaOH. A comparative study on the surface quality after etching of both pristine and machined glass is performed (Figure 2.4). An atomic force microscope (easyScan 2 AFM, from nanoSurf) is used to measure the average surface roughness (R_{avg}) on areas of 25x25 μm^2. After 15 hours, the pristine glass roughness degrades from below 5 nm to around 20 nm with HF and KOH, and to 35 nm with NaOH. On the other hand, under the same etching conditions, a laser-patterned vertical wall shows a $R_{avg} \simeq 80$ nm after HF etching and $\simeq 125$ nm after either KOH or NaOH etching. These results suggest that although leading to higher selectivity and etching speed, the alkali bases produce parts with around 50 % larger roughness compared to HF. To take the best from each etchant, one can for example think of etching a structure with NaOH and then put it in HF for a quick bath to improve the surface quality.
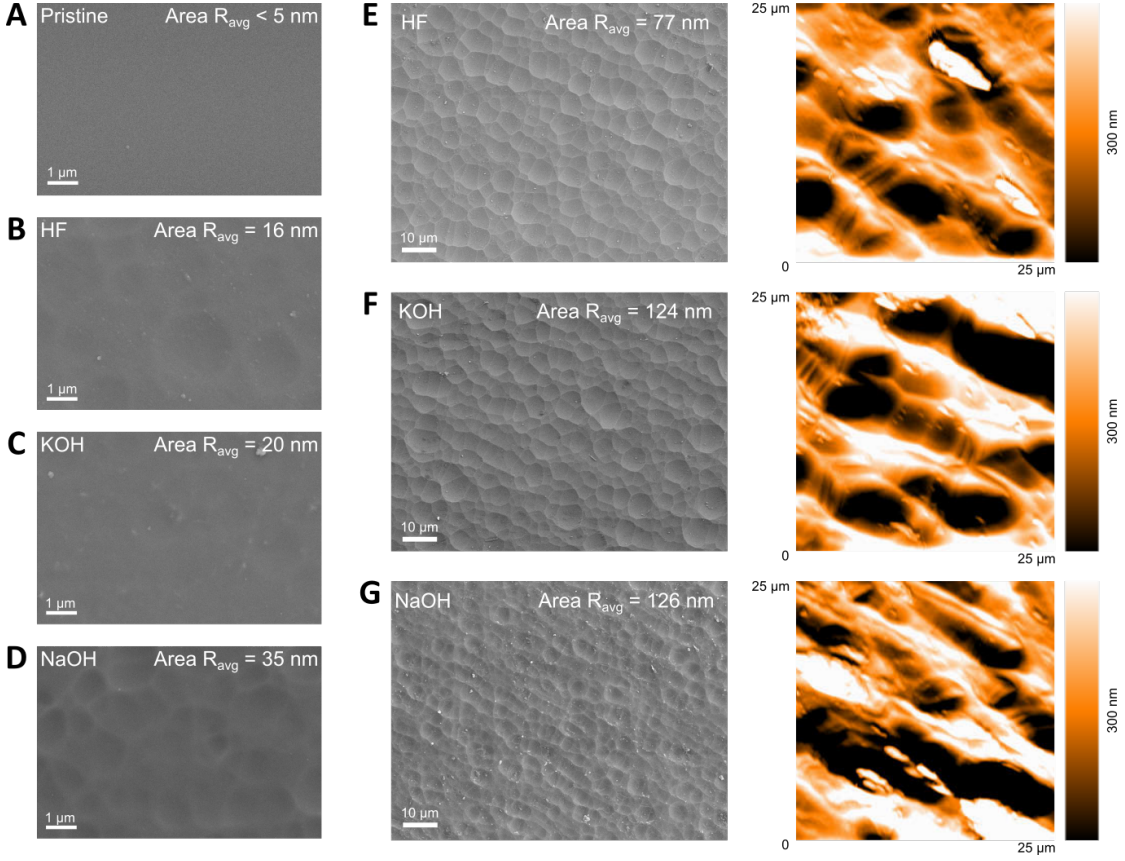
Figure 2.4: *Scanning electron micrographs of pristine fused silica (A) before etching, and after 15 hours in HF (B), KOH (C), and NaOH (D). Micrographs and related average surface roughness measurements of a vertical wall laser-machined and etched for 15 hours in HF (E), KOH (F), and NaOH (G).*

2.4 Effect of polarization

The polarization has a direct effect on the orientation of the nanostructures [64] and is known to affect the etching rate both for HF [21] and KOH [97]. Figure 2.5 shows the etching polarization contrast, defined as the difference between etching rates for the two orthogonal linear polarization directions, defined as parallel and perpendicular to the writing direction. Like the other etchants, NaOH turns out to be also polarization sensitive. Interestingly, the polarization dependence drops to near-zero (or even inverted) for doses corresponding to the low-etching-rate valley ($\simeq$ 3-4 J/mm^2, see Figure 2.1), where the material removal rate drops to a few tens of micron per hour. At very low doses, the difference between the two polarization states is the most pronounced and culminates at 300 μm/h for NaOH, for pulses of 240 nJ and doses of $\simeq$ 1 J/mm^2, value at which the etching rate for parallel polarization is near zero.

The etching rate contrast is actually the highest at very low doses even though only a handful of pulses do overlap, not allowing for a clear formation of self-organized nanogratings as visible through structural changes (see [86, 93] and further in this manuscript).

An important consequence of this observation is that there is an inherent anisotropy in
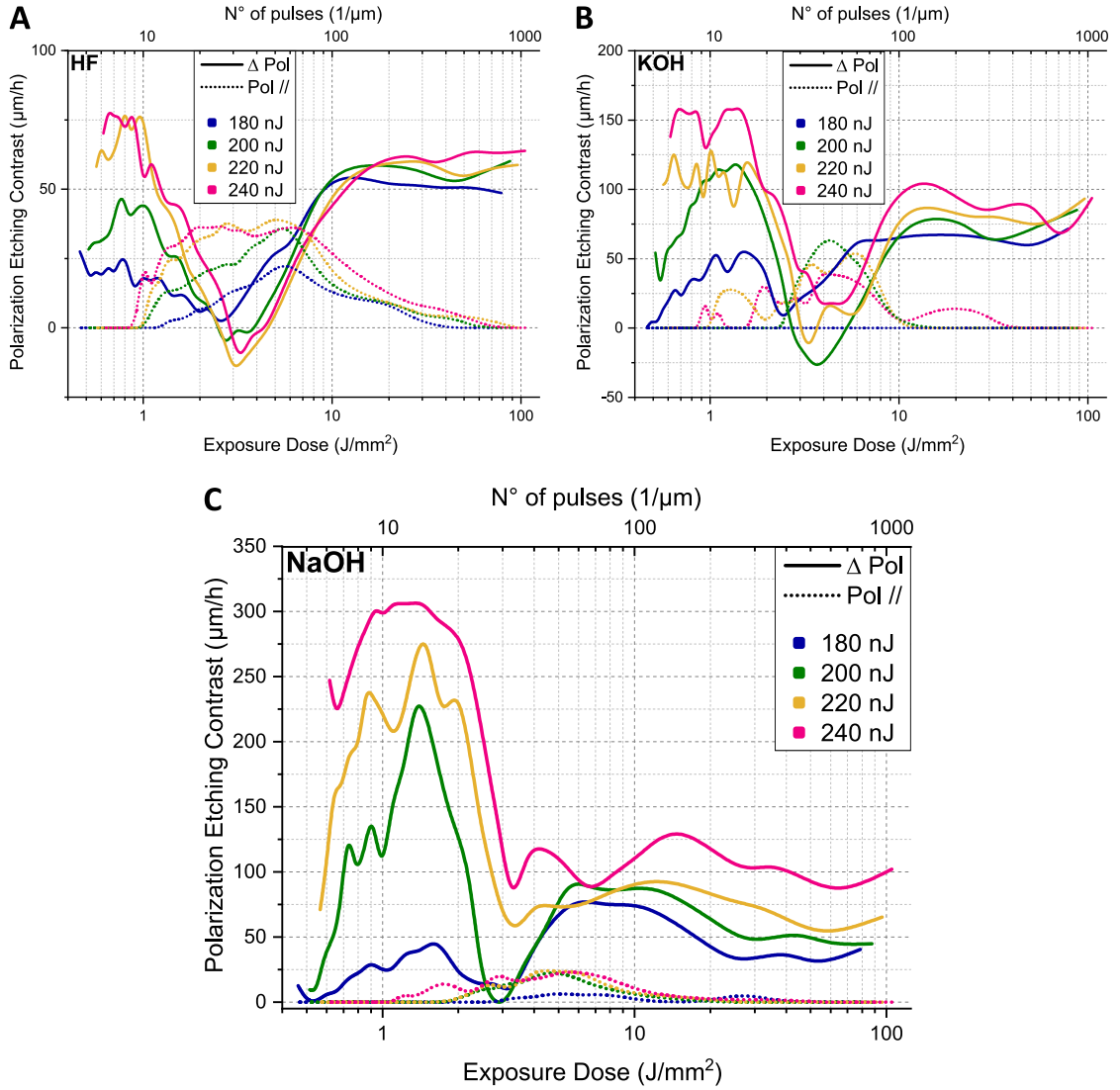
Figure 2.5: *Etching contrast between perpendicular and parallel laser polarization (defined with respect to the writing direction) versus exposure doses for different pulse energies and the three etchants: (A) HF, (B) KOH, and (C) NaOH. For visual purposes, the lines represent the average trends based on the many experimental points. The solid lines show the etching contrast, while the dotted ones give the etching rate for parallel polarization.*

the laser-affected zones already from the very first pulses, and well before nanogratings are formed.

The large polarization contrast has a direct implication on the process implementation as it requires ensuring that the polarization has consistently the same orientation with respect to the writing direction, which can for instance be achieved by mounting a half-wave plate in the beam path and rotating it to follow an arbitrary trajectory. A similar study is performed on the effect of the writing direction (see Figure 2.6). Even if the writing direction should in theory not impact the laser-induced material modifications if we assume an ideal optical beam, it

was noticed during the experiments that it does influence the etching rate. In particular, the writing direction differential remains between +/- 25 μm/h for HF but reaches up to 100 μm/h for KOH and 150 μm/h for NaOH. This effect decreases for increasing deposited energy and might be due to the presence of a pulse-front-tilt in the laser beam.
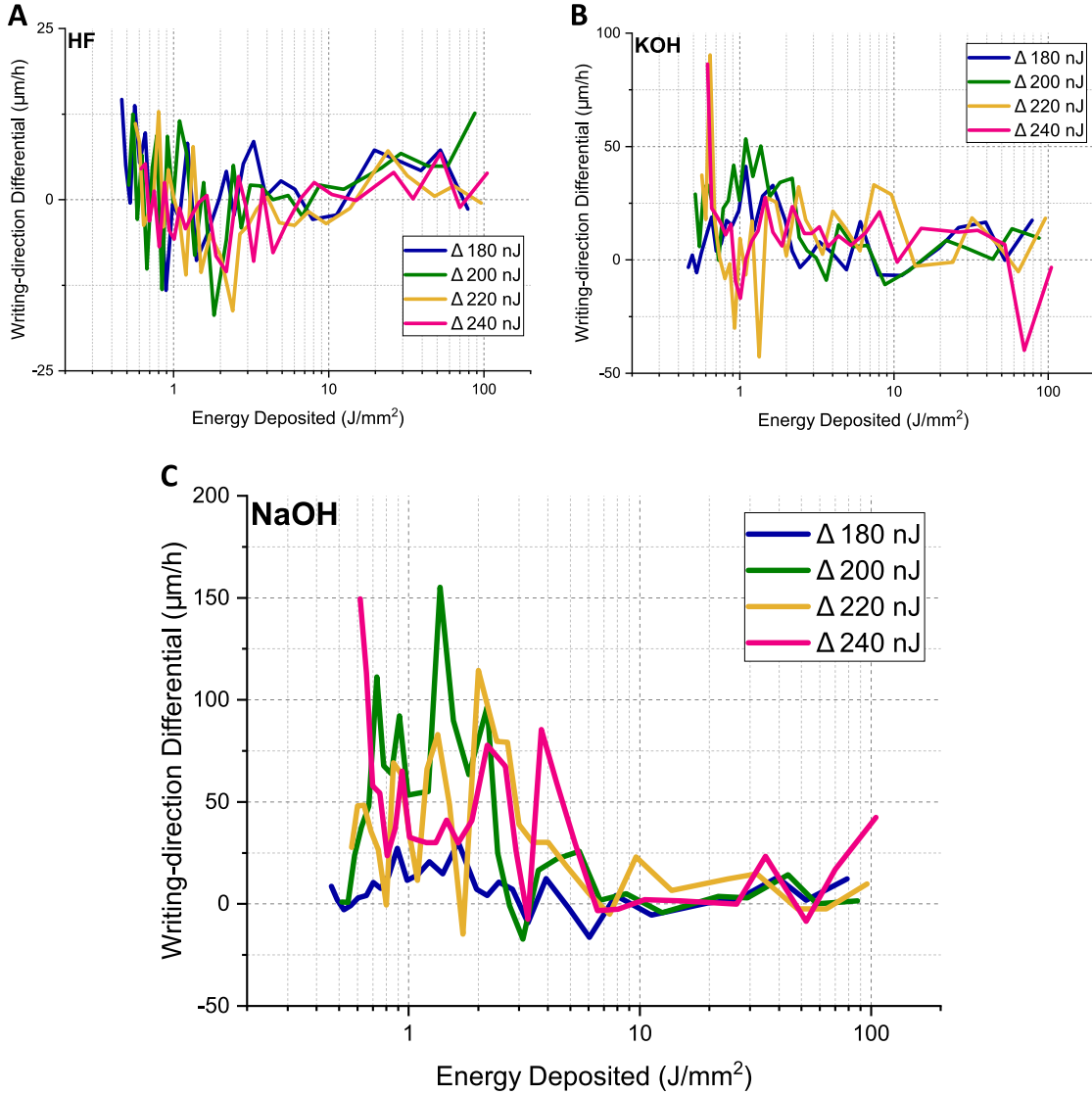

Figure 2.6: *Etching contrast between opposite writing directions (along the same axis) versus exposure dose for different pulse energies and three etchants: (A) HF, (B) KOH, and (C) NaOH. The polarization is constantly kept perpendicular to the writing direction. For visual purposes, the lines represent the average trends.*

2.5   Cross-sectional analysis of laser-written patterns

To further understand the nature of the material changes under varying pulse exposure conditions and to correlate it with etching observations, one sample with the same set of parameters tested is finely polished and etched in HF for three minutes to reveal the cross-sectional view of the laser written lines. Pictures of the specimen are taken using scanning electron microscopy (Zeiss® SEM Gemini 450 operated at 5.0 kV and 100 pA) and assembled in Figure 2.7 to investigate morphological correlations between exposure dose and pulse energies with the etched patterns. In Figure 2.7, the red-highlighted values correspond to the largest etching rate region for each pulse energy, while the blue-highlighted values indicate the energies deposited that lead to the formation of nanogratings, whether it is partial or complete. Interestingly, the highest etching rate does not match with the formation of well-structured nanogratings for pulse energies equal to or above 200 nJ. The first etching rate peak (found around 1.5 J/mm^2) has no direct correlation with morphological traits of nanogratings or possible micro-cracks. Interestingly, at very few overlapping pulses, the connection between porous zones is poor and does not form a continuous pattern as highlighted elsewhere [147, 148]. Yet, the etching rate is among the highest observed suggesting an etching mechanism unrelated to the completeness of porous structures, interconnected or not.

2.6   Effect of annealing on etching rate

Non-ablative femtosecond laser interaction with fused silica leads to permanent defects in the glass matrix when the material comes at rest. At a molecular level, oxygen deficiency centers (ODCs), non-bridging-oxygen-hole-centers (NBOHC), color centers (E' centers) and others [80] form and are considered precursors for the formation of free molecular oxygen trapped in nano-pores [68, 81, 82].

On one hand, nanogratings (forming 'microscopic morphological defects') resist to extreme annealing temperatures (above 1000°C) [149, 150] (even though they undergo a slight degradation above 400°C [151]), while other localized laser-induced structural changes such as laser-induced densification, vanish around 900°C [152, 153]. On the other hand, defects at the atomic glass matrix level that require much less energy to form, can be suppressed at 300°C [153] and be fully annealed at 500°C [81].

We take advantage of these observations to differentiate between morphological/structural versus glass-matrix defects as potential contributors for the observed accelerated etching, in particular in the low-dose exposure regimes. In practice, three specimens with a set of lines exploring different laser parameters were prepared as in the previous experiment, but considering only two pulse energies (200 and 240 nJ) and maintaining a polarization state perpendicular to the writing direction for optimal etching. The specimens were annealed at 300°C for 10 h, with a 1 °C/minute heating/cooling rate constant to limit the creation of defects during cooling [154]. Substrates were then etched for two hours in different etchants and the etching rate was measured according to the same principle described in the previous

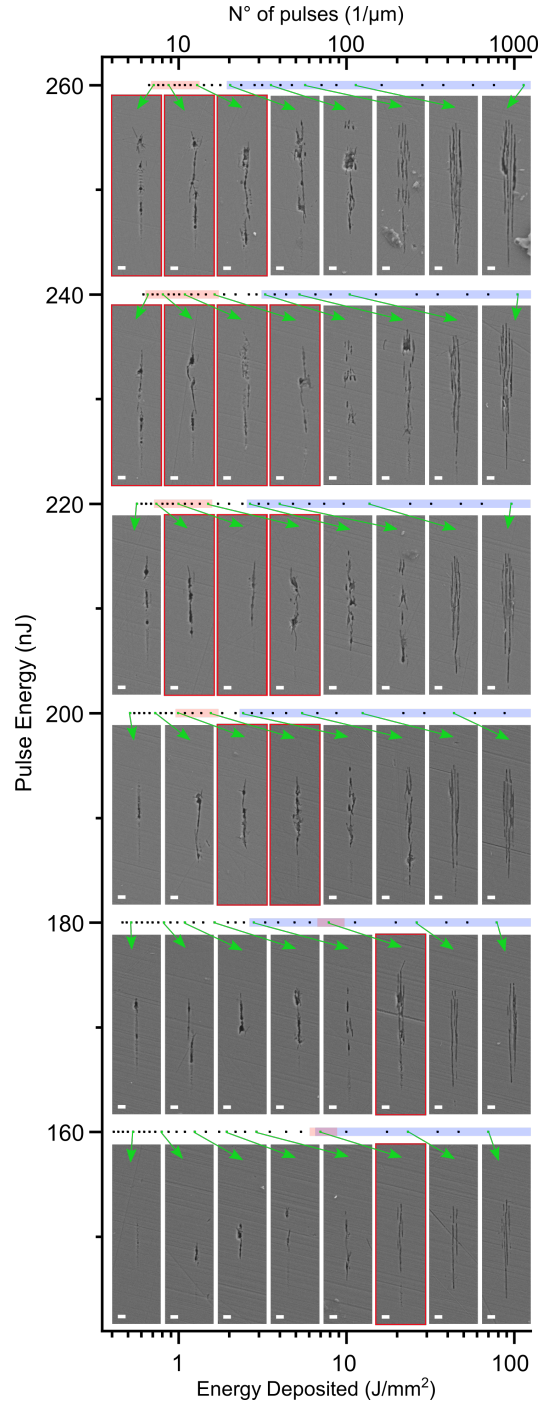Figure 2.7: *Scanning electron microscope pictures of the cross-section of laser written lines for different pulse energy and energy deposited values. The squares represent the energy levels tested, with the green ones corresponding to the indicated images. The parameters highlighted in blue led to the formation of clearly visible nanogratings. The ones highlighted in red correspond to the largest etching rate. The scale bar is 1μm.*

paragraphs. Polishing was then performed to remove the portion of material containing etched lines. This procedure is repeated four times to test the effect of annealing at 300, 500, 700, and 900°C on the etching rate. The results are shown in Figure 2.8.
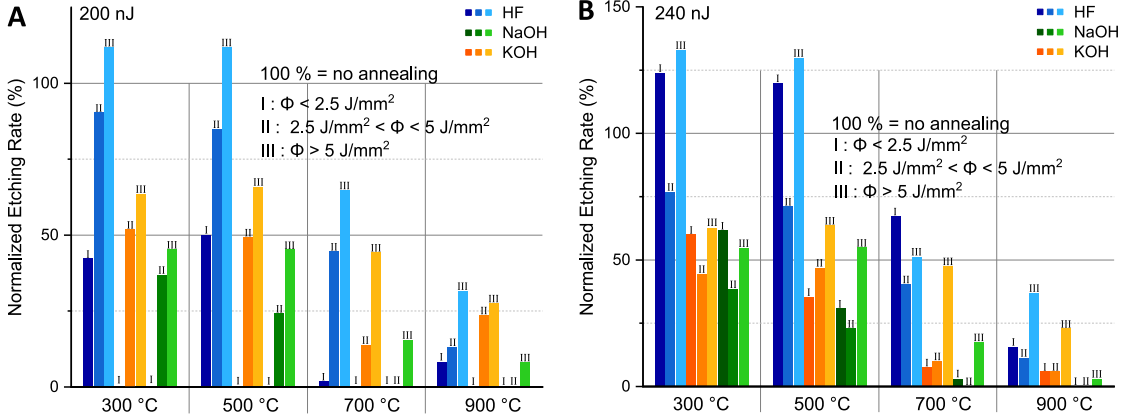

Figure 2.8: *Comparison of etching rates versus energy deposited before and after annealing for a fixed pulse energy of 200 nJ (A) and 240 nJ (B), for the three etchants (HF, KOH, and NaOH), and the three distinct zones of interest defined in Figure 2.1. The etching rate is normalized to the etching rate before annealing.*

Let us first consider the effect of the annealing on the HF etching rate (Figure 2.8A-B, blue bars). The annealing up to 500°C – reported to quench defects [81, 153] – reduces the etching rate only in the case of lower exposure doses and pulse energies (region I for 200 nJ), but does not decrease nor the higher-energy deposited peak nor the etching rate for a pulse energy of 240 nJ.

In both cases, we assist to a fictitious increase of the rate (only in region III for 200 nJ while in both region I and III for 240 nJ), which is due to a capillarity-driven degradation in etching selectivity of HF [97] and the decreased etching time from 4 h to 2 h for the measurements done before and after annealing, respectively. Such discrepancy among 200 and 240 nJ can be attributed to the creation of a larger amount of defects when higher pulse energy (i.e. field strength) is used, which can also explain the sharp decrease of noise in the etching rate measurements of Figure 2.1 for increasing pulse energy and is in line with the stochastic essence of non-linear absorption phenomena. In other words, we assume that the decrease in defects' density, after annealing at 300°C and 500°C for 240 nJ of pulse energy, increases the mean distance between neighboring defects to a value that impacts minimally the HF.

The annealing temperature is further increased to values at which possible localized densification effects on the silica matrix are relaxed into larger and more stable ring structures (i.e. 700 and 900 °C) [150–153]. At this point, the HF etching performance degrades down to 50 and 30 % of the original etching speed before annealing. Such behavior hints that the HF etching mechanism is driven mainly by porosity and associated localized densification of the glass structure, at least in regions II and III. Indeed, structural changes locally cause a sharp increase in active surface and densification, suggested by the presence of small member rings,

which augments the chemical reactivity of the Si-O bonds [155–157].

KOH (orange bars in Figure 2.8) and NaOH (green bars in Figure 2.8) show radically different behavior. At pulse energies of 200 nJ, the first annealing at 300°C almost completely cancels the low-energy deposited etching rate peak, while it halves it in the case of 240 nJ. As before, we interpret the different behaviors between pulse energies as due to the initial density of defects, larger for higher pulse energy, and assume that the annealing is not enough to cancel out all the defects for 240 nJ. Although to a lower extent, the etching peak corresponding to the highest energy doses ($\simeq 10$ J/mm^2) starts decreasing already at 300°C. When the annealing temperature is further increased, the decrease in etching rate continues smoothly for KOH and sharply for NaOH. Those trends indicate that the etching mechanism of KOH and NaOH is different from the one of HF and driven mainly by the presence of defects in the matrix and only partially by the presence of porosity or associated densification effects. In this context, NaOH tends to be the most selective and the most affected by the laser polarization state, the writing direction (see Figure 2.6), or the annealing conditions. Finally, it should be noticed that even if mainly defects-driven the etching rate of NaOH and KOH is highly dependent on the laser polarization (as shown in Figure 2.5B-C), which indicates that a self-organized structural configuration of the defects does exist at the very first stage of the laser interaction, and before the occurrence of pores and nanogratings forming a pathway for the etchant to progress.

We interpret these observations as follows. For low exposure dose (region I in Figure 2.9), the etching enhancement is due to the presence of defects localized within the laser-affected zone. With the pulse duration considered here, it is known that defects mostly consist of NBOHCs and E' centers (see in particular [158]). Both the cross-sectional analysis (Figure 2.7) and the annealing study (especially for 200 nJ of pulse energy) support this hypothesis. Further insights could be obtained from defects density estimation through electron spin resonance (ESR) spectroscopy [1, 159]. The lower (or none in case of HF) decrease in etching rate after 300°C and 500°C annealing of modifications with 240 nJ of the pulse energy is linked to the density of defects created versus the amount canceled by the annealing. We assume that the mean-free(of defects)-path is reduced to a value that starts to influence the etching rate of KOH and NaOH, but not the one of HF, due to their difference in etching rate of pristine silica (see vectors of Figure 2.9).

Further increasing the exposure dose (region II in Figure 2.9) leads to a sharp decrease in etching rate which we attribute to the transition from defects to pores. A possible explanation is that higher exposure doses result in the quenching of defects, suppressing the etching enhancement effect. This interpretation remains speculative and further analysis is required to unravel the cause behind the dip in etching rate for region II. Finally, in the high exposure dose (region III in Figure 2.9) the nano-pores start coalescing and forming coherent networks with a preferential orientation and ultimately the so-called nanogratings. In this fashion, an accelerated etching is recovered, but this time is driven mainly by the inherent porosity of the material and to a lesser extent by possible additional stress-induced etching-enhancement effects within the laser modified regions [99, 137, 160]. Due to the difference in etching pristine material, in the case of hydroxide-based etchants, this second etching mechanism is significantly less favorable than the one driven by oriented defects, while it results in a similar

enhancement for HF-based etchant.
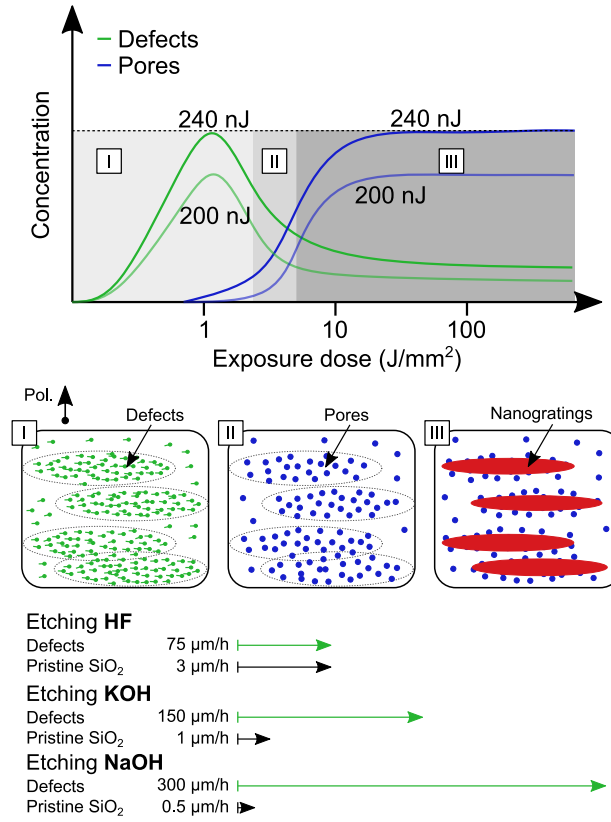
Figure 2.9: *Schematic interpretation of the etching mechanism in the region of interest defined above. Top to bottom: the graph shows a qualitative representation of the variation in defects' and pores' quantity depending on exposure dose and pulse energy; the three panels provide a visualization of the modifications induced in each regime with a fixed vertical polarization; and the colored vectors display the etching rate of dense of defects versus pristine* SiO_2 *for HF, KOH, and NaOH.*

2.7   Summary and conclusion

Let us summarize the main findings of this study:

- For the three etchants investigated, similar phenomenological behavior is observed: a first regime in the low-exposure doses corresponding to around ten overlapping pulses ($\simeq 1.5\,\text{J/mm}^2$), followed by a second regime defined with a local minimum in etching rate and then a third regime, at higher dose, where an etching maximum is recovered.

- For the three-etchant investigated, the local etching maximum corresponding to the low exposure doses ($\simeq 1.5\,\text{J/mm}^2$) with few pulses overlap, the so-called nanogratings are not yet distinctly observed. This first exposure regime at low doses is observed only above a given pulse energy threshold (here at $\simeq 180$ nJ), higher than the one for

observing modifications. Despite the absence of a visible self-organized pattern after etching, depending on the linear polarization orientation a strongly anisotropic etching behavior is observed. It is particularly pronounced in the case of NaOH, where an anisotropic ratio of $\simeq$ 1200 to 1 μm is observed after only 4 hours.

- HF acid-based etchant displays a different behavior than hydroxides-based etchants. While KOH and NaOH's highest etching rates are observed for the low-exposure dose regime, for HF similar local maxima in etching rate are found in both the low- and high-exposure dose. Annealing below 500°C has a dramatic effect on the low-exposure dose etching behavior, eventually completely canceling the etching enhancement for NaOH and KOH at low pulse energy, while it has limited effects on the HF etching behavior.

- Sodium hydroxide (NaOH) as an etchant for femtosecond laser-assisted 3D micro-manufacturing shows superior performances compared to known alternative methods, based on HF and KOH solutions. It reaches an unprecedented etching rate of 300 μm/h, twice more than KOH and near four times more than HF. As the natural etching rate of silica by NaOH is very low, the contrast between exposed and unexposed etching rates yields an extreme aspect ratio approaching 1 to 400, for tunnel-like patterns.

In conclusion, from a technological point of view, the observation of an optimal etching rate surpassing the previously reported ones and this, at very low doses, offers a boost in achievable laser-exposure writing speeds larger than one order of magnitude. Moreover, while maintaining an optimal etching rate and selectivity, the aspect ratio obtainable is significantly increased, which is of practical importance for fabricating slender and denser structures.

3 3D-microcasting

Despite the remarkable progress made in recent years, producing freeform three-dimensional micro-components out of copper, silver, or gold and their alloys remains an engineering challenge: current processes are either too slow to be economically viable or produce porous or otherwise imperfect metal microstructures. Here we introduce an alternative, faster approach for the freeform fabrication of metal micro-components amenable to the processing of noble metals. The process begins with the 3D, micron-resolution, carving of arbitrarily shaped interconnected molds into amorphous silica using femtosecond laser micromachining and selective etching. This is followed by pressure infiltration of the mold with the molten metal, which is subsequently solidified. Metal architectures produced by this process have a micron-scale resolution, are fully freeform and multiscale in geometry, and are made of dense metal, while the processing speed largely exceeds what is achieved in current alternative metal microfabrication approaches. The resulting glass/metal combinations enable new micro-device architectures. Alternatively, by mold dissolution, self-standing micron-scale 3D metal parts are produced, of high metallurgical quality and with features sizes down to $\simeq 2\,\mu$m.

3.1 3D micromanufacturing of metals

Many domains of technological progress, including microelectromechanical systems (MEMS), microsensors, metamaterials, integrated optical devices, microfluidic, medtech micro components, or microelectronic devices, rely on the availability of geometrically complex structures made to micrometric resolution [161]. Most established manufacturing processes at such a small scale have geometrical constraints that limit them to two dimensions or particular geometry types with specific symmetry properties, such as cylindrical or spherical. The production of truly freeform 3D shapes at the microscale, i.e. with no geometrical constraint across all three spatial dimensions, with micron to sub-micron resolution, has been an ongoing quest for decades.

In particular, the 3D freeform production of metallic structures to a micron and sub-micron level of precision remains challenging. Current selective powder-melting or sintering methods do not reach such resolutions, the smallest features achievable being currently limited by the size of the powder to roughly 20 μm [162]. Other methods fit for the production of metallic micro-components include the electroplating-based LIGA process [163, 164], micro-beam machining [165–167], micro/nano-forming [168] and processes that add metal to the surface of patterned glass [123, 124, 169, 170]. None of these technologies, however, provides full geometrical design freedom in all three dimensions. To these, recent years have seen the addition of a wide range of novel, generally, still experimental but truly three-dimensionally freeform, additive manufacturing processes, of which a detailed and extensive recent review can be found in References [171, 172].

Current cutting-edge additive 3D freeform micromanufacturing processes include (i) metal-ink 3D printing followed by annealing, metal lift, and deposition, (ii) locally triggered chemical vapor deposition or chemical reaction, as well as (iii) high-precision in-situ electrolytic deposition. Most of these 3D metal additive micromanufacturing methods afford full 3D design

freedom, but often produce parts of porous or irregularly shaped metal (e.g., [173–178]), with the exception of local electrodeposition methods, which have in recent years demonstrated the production of complex, high aspect ratio, smooth-surface 3D freeform structures of dense metal shaped to sub-micrometric resolution [171, 172, 179–181]. Point-by-point local electroplating has, however, the limitation that volumetric metal deposition rates remain low, limiting that method to prototyping or niche applications.

We present here an alternative approach that enables the fabrication of dense noble metal micro-components to micrometric resolution and has the potential for far higher production rates than current alternative processes: multiscale structures of size up to a few millimeters that have micron-scale features, unprecedented 3D complexity, and sub-micron surface roughness are demonstrated. In this approach, freeform processing is first conducted in subtractive mode, starting with a glass substrate that is carved, using 3D femtosecond (fs) laser microfabrication followed by selective etching, to create a hollow that has the shape of the metal structure that one aims to produce. The hollow is then filled with molten silver, copper, gold, or their alloys. This is achieved using elevated-temperature pressure infiltration to create, once the metal has solidified, what amounts to a cast metal structure freely shaped to micrometric resolution.

Seen differently, the present process is indeed a miniaturized variant of metal casting. Metal casting has resisted miniaturization down to sub-millimeter size scales mainly because, at the microscale and at the elevated temperatures characteristic of molten engineering metals (on the order of 1000°C), capillarity coupled with high atom mobility rates interfere to disrupt the process. Interference of these phenomena with the casting process is manifest on three fronts: (i) capillary forces oppose metal ingress into fine-scale mold cavities because molten metals have high surface tensions and wet poorly nearly all ceramics [118]; (ii) capillary forces coupled with high atom mobility at metal casting temperatures deform the surface of crystalline mold materials conventionally used to make precision molds. Indeed, wherever the mold surface intersects crystal defects (dislocations, interfaces, or grain boundaries), capillary force equilibration creates micron-scale depressions along the mold surface. Those depressions matter little in conventional macroscale casting; at the microscale, however, once filled with metal, such depressions become as many unwanted, comparatively large, protuberances along the cast metal surface. (iii) At temperatures such as 1000°C, chemical reaction rates are high. This leads to an additional limitation, namely that there must be no chemical affinity between atoms that make the mold and those that make the metal.

We overcome here the first physical limitation (i) by pressurizing the hot molten metal in a way that forces it against capillary forces to fill micron-scale mold cavities. We address the second limitation (ii) by using an amorphous, and hence microstructurally featureless, material, namely glass, to make the mold. Finally, we overcome the chemical limitation (iii) by working with metals made of elements that have an oxide less stable than that of silicon; this includes noble metals, which are of prime interest in microtechnology by virtue of their corrosion resistance and high conductivity.

With those features, the present process goes well beyond previous attempts to push down the resolution of metal casting. Those have produced parts on the order of a few tenths

of a millimeter ($\simeq 100\,\mu$m) in size, but have not reached micrometric freeform resolution [119, 120, 182, 183], or are restricted to casting one of the few metals or alloys that melt near room temperature [121].

3.2 Process concept

Process steps that lead to producing 3D structures of dense engineering noble metal with a sub-micron resolution are detailed in Figure 3.1. As an illustration, we show the production of a micrometric classroom containing a series of miniature chairs and desks. Step 1 in Figure 3.1 consists in exposing quartz glass to femtosecond laser irradiation according to a freely designed interconnected geometrical pattern that defines the material to be removed by altering locally the glass structure. This alteration causes the glass to be preferentially etched where it has been exposed to laser irradiation.

This process is based on nonlinear absorption phenomena. These events are observed in otherwise transparent substrates when the incoming laser beam locally exceeds a peak irradiance level (typically around GW/mm^2), triggering a chain of events leading to the ionization of the matter. As the effect is non-linear and depends on a threshold value, the effective size of the ionized volume can be smaller than the beam waist itself and the laser wavelength [2, 3, 19]. In addition, given the extremely short plasma lifetime, the absorbed energy remains confined in the focal volume and no heat is transferred to the surrounding, which thus remains largely unaffected [184, 185]. Combined with high-accuracy beam trajectory thanks to the use of high precision motorized stages (PI Micos with repeatability of 200 nm over a centimeter motion range and a micron over the full travel range), it enables the engraving of arbitrary 3D-shapes made of single-voxel sizes that depends chiefly on the confocal parameters and the pulse energy. In our case, considering a beam waist at the focus of 1.9 μm and a moderately focused beam with an energy of about 240 nJ, a voxel of laser-modified volume has an ellipsoid shape with 1.9 μm and 8 μm on the short and long axis, respectively. Smaller voxel sizes can be achieved by lowering further the pulse energy.

In Figure 3.1 step 2 wet chemical etching of the substrate preferentially removes those regions that were modified by the laser along a path that intersects the mold-free surface. The etching-rate contrast between pristine and modified mold material depends on the chemistry used (namely, with fused quartz, etching with a basic – KOH [97], or NaOH [98] – or with an acidic – HF [3, 19] – solution), on the deposited energy (or net fluence), and on other laser-related parameters such as the laser-beam polarization or the pulse duration [137]. By precisely controlling the exposure and the etching steps, it is thus possible to achieve micrometric resolutions in mold manufacturing. As the etching front progresses inward from the mold surface through the exposed pattern, the final shape of the etched volume becomes diffusion-limited and shows a dependence on the etching rate contrast between pristine and exposed material. This may lead to a dependence of the etched geometry on the time of exposure to the chemical solution, to be compensated for in the design of the path followed by the fs-laser beam.
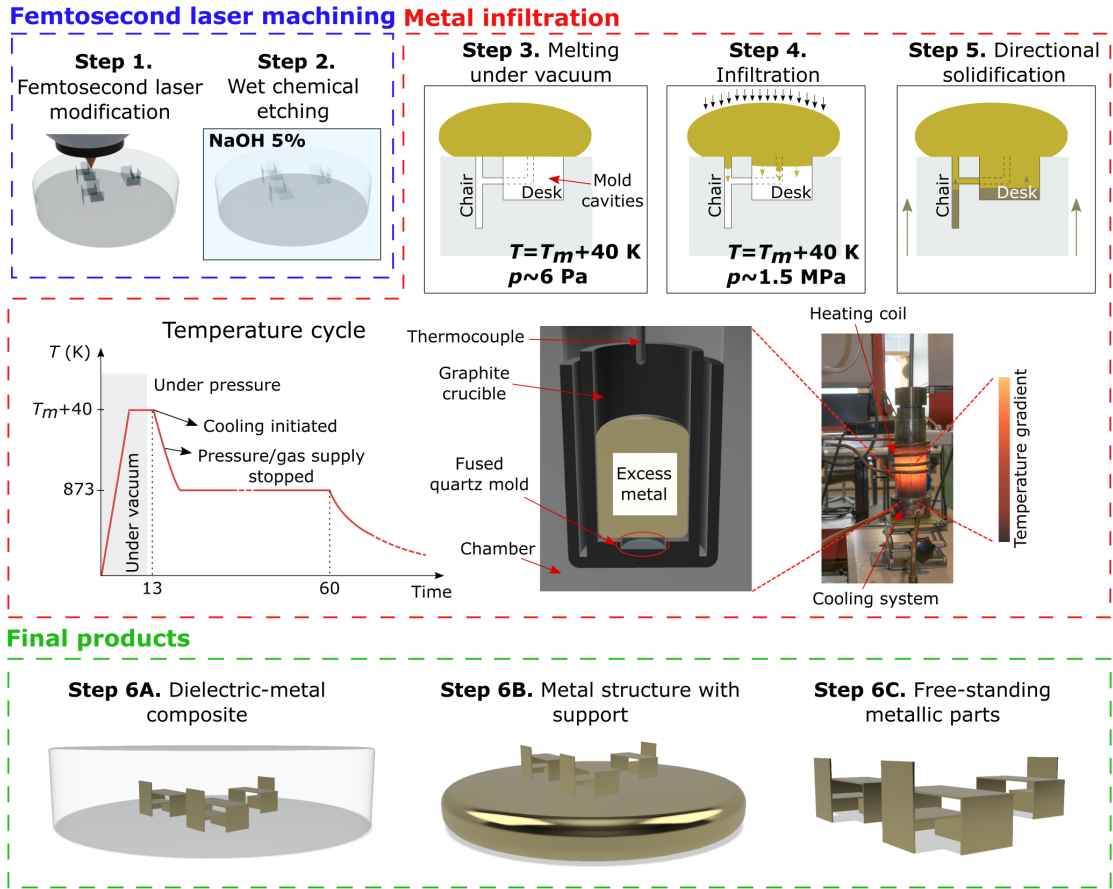
Figure 3.1: *Schematic of the microcasting process. The process comprises two main sequences, one being fs-laser 3D micromachining, and the second being metal pressure infiltration. Step 1 – a pattern defining the 3D structure is inscribed within a fused quartz substrate using a fs-laser. Step 2 - the substrate undergoes wet chemical etching to dissolve interconnected laser-patterned regions that intersect the substrate surface, thus turning the fused quartz substrate into a mold to be filled with metal. Step 3 - the fused quartz mold is positioned in the infiltration chamber, together with a metal load placed over the exposed cavities; the chamber is evacuated and the temperature is raised to melt the metal. Step 4 - pressurized inert gas pushes the metal against capillary forces, driving it to fill the pre-evacuated hollows. Step 5 - while maintaining the pressure, the chamber is put in contact with a chill to promote directional solidification. Step 6 - different final microscopic products can be obtained by varying final steps in the process.*

Filling of the cavities with the metal, Steps 3 to 5 (Figure 3.1), is performed by applying external pressure on the liquid metal sufficient to overcome capillary forces at play and make it flow into the mold. This is achieved using pressurized gas. In experiments reported here, the metal to be infiltrated is placed on top of the substrate, over all exposed cavities. The chamber is evacuated, then kept under a low vacuum, and heated up to slightly above the melting point (T_m) of the metal to be cast. Once it is molten, the metal covers and seals all mold entries along the upper mold surface. At this point, a non-reactive gas, typically argon, is bled into the

chamber. As the gas pressure builds up, the pressure it exerts on the metal eventually drives the latter to flow into the (evacuated) cavities of the mold, filling them. Once the mold is full, mold and metal are cooled to solidify the metal. In doing this, particular consideration must be given to feed metal solidification shrinkage, a classical challenge in casting also present at the microscale. To this end, directional metal cooling is used; this is done by placing a chill in contact with the apparatus along the substrate side opposite to the metal drop. One must also avoid the formation of cracks that may appear in the brittle glass substrate under the action of thermal stresses associated with the difference in coefficients of thermal expansion (CTE) between metal (typically $\simeq 10 - 20\ \mu\text{m}/(\text{m}\cdot\text{K})$) and substrate ($\simeq 0.5\ \mu\text{m}/(\text{m}\cdot\text{K})$). Such cracks were observed in some of our experiments through standard and cross-polarized optical microscopy; they are avoided through slow cooling after infiltration.

After solidification (Figure 3.1 Step 6), a substrate-metal composite is produced. The excess metal can be removed to obtain a microscopic fused quartz/metal composite structure that can, in itself, be of interest in microengineering device fabrication (Figure 3.1 Step 6A). Alternatively, to produce a loose metal casting, the glass mold is dissolved in an etchant to which the metal is inert (for example, an aqueous HF solution when casting silver). Demolding -in the terminology of casting- can either produce miniature structures that are linked to a bulk metal base (Figure 3.1 Step 6B) or if Steps 6A and 6B are combined, it will yield many separated miniature metal castings (Figure 3.1 Step 6C).

3.3 Experimental methods

The glass molds were fabricated using fs laser micromachining followed by wet chemical etching according to a known process described in the literature [19]. We used a Ytterbium-fiber amplifier laser (Yuzu, manufactured by Amplitude, Bordeaux, France) emitting 270 fs pulses at a wavelength of 1030 nm at a repetition rate of 800 kHz, with an energy of 240 nJ (average power after the objective of about 190 mW). The laser is focused in the specimen using a 0.4-numerical aperture objective to a measured waist of 1.9 μm at the focal point. The substrate used is a UV-grade fused quartz plate (Heraeus HOQ 310), 800 μm-thick, and 25 mm-square. The substrate is moved with linear stages (Micos - UPS 150). Following laser exposure, the specimen is etched for several hours in a 5 %$_{\text{wt}}$ NaOH bath at $\simeq$90 °C. To fit the dimensional requirements of the chamber used for metal infiltration, the substrates are cut into circular disks of 6 mm diameter to produce the molds into which the desired shapes to be injected are laser-patterned and subsequently etched.

The setup used for pressure infiltration consists of a refractory stainless steel (UNS S31400) chamber in which an alumina crucible prevents contact of the steel chamber with a graphite crucible that contains both the mold and the metal (see Figure 3.1). Once mold and metal are placed within the graphite crucible, the infiltration chamber is bolted shut at its top. The top of the chamber contains a carbon foil to seal the closure and is connected to a vacuum pump and an argon bottle through a pipe, in which a K-type thermocouple is also introduced to

monitor the temperature during infiltration by placing the thermocouple tip 1 mm above the melt. The chamber is evacuated (usually to $\simeq 0.06$ mbar) and positioned within an induction coil using an overhead crane. A GMF12 CELES (Lautenbach-France) induction furnace is utilized to heat the ensemble, to 1000 °C in the case of silver and 1100 °C for infiltration with copper or gold. Once the target temperature is reached, the chamber is pressurized with an inert gas (Argon N48, typically at $\simeq 1.5$ MPa for structures of minimum feature size exceeding 1.5 μm, or 5 MPa otherwise). Subsequently, the chamber is lowered until its bottom is in contact with a water-refrigerated copper chill, maintaining the pressure and also with the induction furnace turned on, to create a vertical temperature gradient to promote directional solidification. Once the solidification temperature is reached on the thermocouple reading, the chamber is cooled further and then kept at $\simeq 600$ °C during 1 h to relieve internal stresses caused by differential shrinkage between the mold and the metal. Heating is then stopped and the substrate-metal component is removed once it has reached room temperature. Pure silver (Figure 3.2, 3.5A, 3.6A-B, 3.6D), gold (Figure 3.3) or copper (Figure 3.6C), all of 99.99 %$_{\text{wt}}$ purity, were utilized as infiltrant metals as well as a silver-copper alloy (79%$_{\text{wt}}$Ag-21%$_{\text{wt}}$Cu) (Figure 3.5C and D). To produce cast metal structures released from their mold, in a final step the fused quartz mold was dissolved in high concentration HF during approximately 12 h (Figure 3.2, 3.3, 3.6D).

3.3.1   Materials characterization

Scanning electron microscopy images were obtained at 3kV using a Zeiss® GeminiSEM 300 (Oberkochen, Germany) equipped with a standard Everhart-Thornley secondary-electron detector and an Oxford Instrument EDS detector. EBSD images were acquired at 25kV using a Zeiss® SEM Gemini450 (Oberkochen, Germany) equipped with a symmetry CMOS, operating with Aztec acquisition and data treatment software (Oxford Instruments, UK). Optical micrographs were taken with a Hirox digital microscope KH-8700 (Tokyo, Japan).

Composition gradients near the interface of the host substrate/metal, exposed by conventional grinding and polishing of infiltrated beams still embedded in the fused quartz mold, were analyzed by Energy-dispersive X-ray spectroscopy (EDS) in the scanning electron microscope operated at 10 kV (Figure 3.4). The X-ray intensity at the metal-silicon dioxide boundary was modeled with CASINO Monte Carlo software v2.5 (Sherbrooke, Canada) assuming a 10 kV electron beam, beam size 5 nm, and 10000 electrons. A TI 950 Triboindenter (Hysitron® Corporation, Minneapolis, MN) with a load cell of 10000 μN and a diamond Berkovich indenter tip was used to measure both the hardness and elastic modulus of the cast from cross-sections of trusses still embedded in the fused quartz substrate (similar to what is seen in Figure 3.3E). Quasi-static indentations were made to a maximum load of 8000 μN for silver and to 3000 μN for copper, the loads being selected in correlation with the trusses' cross-sections (150x150 μm for Ag silver and 25x25 μm for copper) to minimize the elastic influence of the substrate and to be able to indent 4 times on each specimen. The loading-holding-unloading sequence was of 5-2-5 seconds and the data were analyzed according to the Oliver-Pharr procedure [186].

3.4 Results

Figure 3.2 displays images of such a tiny classroom composed of desks and chairs, all made of pure silver. This particular assembly demonstrates the ability of the present process to produce, at the microscale, complex 3D structures with a shape that is not amenable to metal micromachining. The cast structures have a thickness near 2 μm. The similarity of chair/table pairs shows the reproducibility of the technique, and its resolution is shown by the submicron surface roughness of the mold or casting. In this illustration, to allow for observation in the scanning electron microscope, the fused quartz substrate was dissolved after solidification; this left the final metal chair and table structures linked to the silver that remained above the substrate (as in Figure 3.1 - Step 6B). Figure 3.2C and D show a close inspection of one of the chairs in two different perspectives, to exhibit its thickness and contours. In particular, a rough and wavy finishing of the top edge is observed. This feature is associated with the progressing etching front after laser machining during mold preparation and is later on reproduced by the metal during infiltration and solidification.

Specifically, such imperfections are found if the etching is interrupted before the entire laser-affected region is removed. It is in fact not seen on the other edges of the structures of Figure 3.2 (or in subsequent figures). On the other hand, the slight roughness on the lateral edges of the chair (in Figure 3.2D) derives from the laser machining trajectory followed during mold preparation and can be avoided by optimizing both the laser trajectory and the deposited energy. As shown in Figure 3.2E, the metal grain size far exceeds that of casting features, such that chairs and tables are essentially all monocrystalline – this parallels what was found with cast aluminum microwires cast using molds of grown NaCl single-crystal [182].

The process was also used to fabricate a set of suspended ('H-shape') beams made of pure gold, Figure 3.3. The suspended beams in Figure 3.3 have a 45 x 45 μm^2 square-cross section and a length of 900 μm, demonstrating an aspect ratio (AR) – cross-section over length - as high as 20. Furthermore, in this experiment the AR was not maximized: higher values are likely achievable. Indeed, fs-laser micromachining has demonstrated AR values that exceed 500 with only two entrance points for the etchant [187] and has no theoretical aspect ratio limit if multiple entries can be included [19]. Close inspection of the mold surface along a longitudinal cut through an un-infiltrated mold along the length of the suspended-beams (Figure 3.3C) reveals features typical of fs-laser exposed silica glass etched with hydrofluoric acid [188]: note how those are later on reproduced by the gold (Figure 3.3B). This demonstrates that the pressure infiltration process used here can replicate shapes with a sub-μm-scale resolution, similar to what is obtained in polymer molding [189]. Even though the overall surfaces of the suspended beams are easily correlated to features on the mold, some peculiarities can be distinguished in some structures (red delimited areas in Figure 3.3D). These depressions are particularly smooth and they interrupt surface patterns present on the fused quartz surface; hence, they may have been produced by metal solidification shrinkage or the presence of trapped gas.
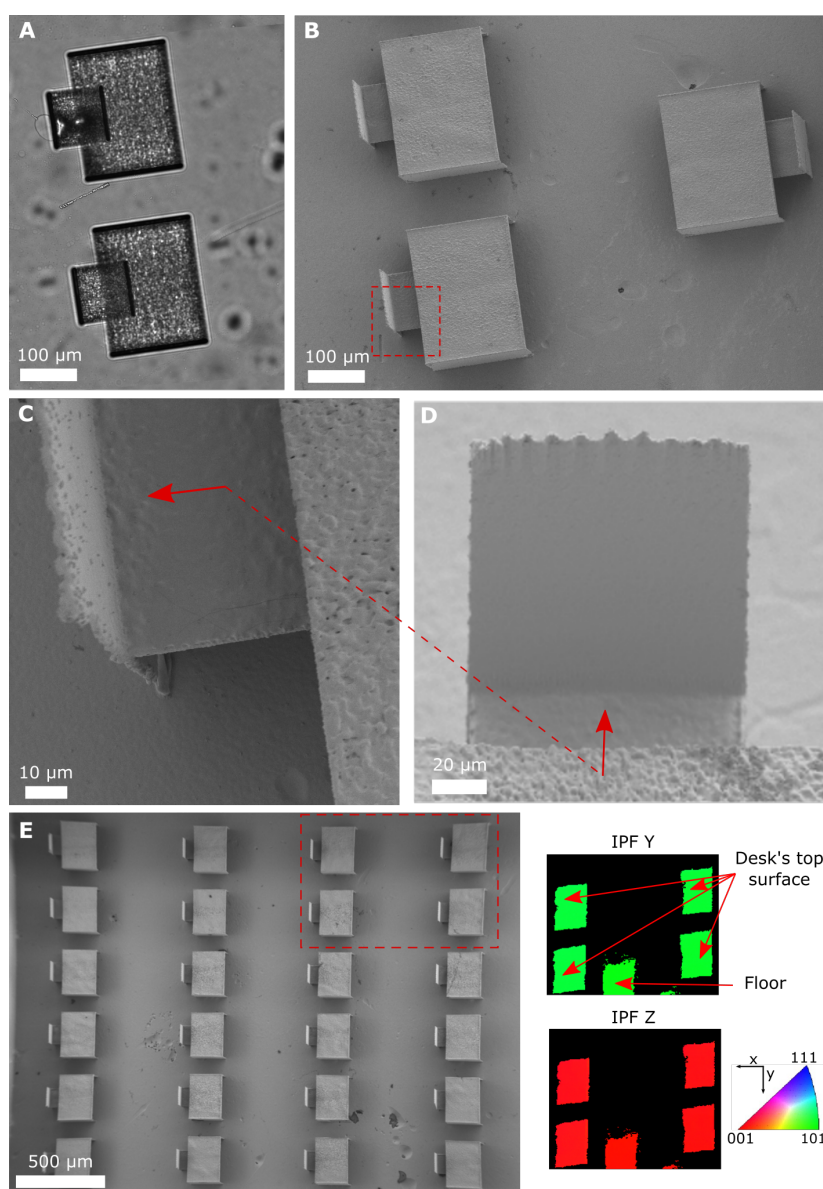
Figure 3.2: *Images of a cast silver miniature classroom. (A) reveals the fused quartz substrate (i.e., the mold) after etching and before metal infiltration (Step 2 in Figure 3.1). In (B) the metal structure is shown after the dissolution of the mold (Step 6B in Figure 3.1). (C) and (D) details at higher magnification the area delimited by the dashed rectangle in (B), the arrow indicates the orientation of (D) with respect to (C). (E) An array of 6x4 'chairs' and 'desks' and inverse pole figures (IPF) of the four 'desks' contained in the red dashed rectangle, evidencing that these, as well as the 'floor' (i.e. the support), are single-crystalline metal structures. (A) Optical microscopy performed through fused quartz, (B), (C), (D), and (E) scanning electron microscopy (SEM) and (E) electron backscatter diffraction (EBSD).*

Local properties of the metal were measured by nanoindentation: for the pure silver of this casting, data yield Young's modulus of 84.1 ± 1.2 GPa, to be compared with 83 GPa for bulk silver [190], in accord with the observation that the microcast metal is fully dense. While for
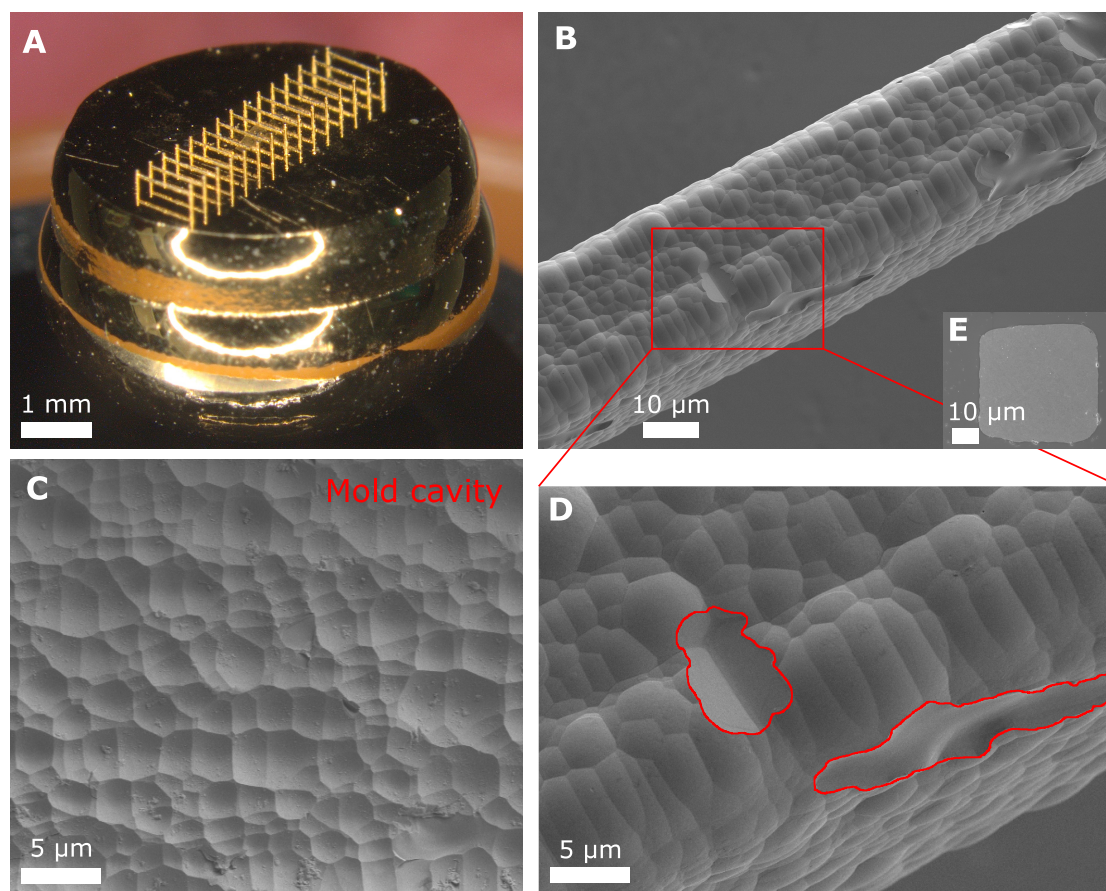
Figure 3.3: *Images of suspended beams made of gold and left connected to the bulk metal. (A) overall view of the piece after the dissolution of the fused quartz mold. (B) SEM close-up image of a single suspended beam showing features typical of a silica glass etched with hydrofluoric acid. (C) SEM images of the internal surface of an etched, uninfiltrated mold cavity. In (D) a portion of the beam in (B) is shown to highlight likely surface casting defects in red. (E) SEM image of a cross-section of a similar silver structure while it was still embedded in the fused quartz mold, showing that the beams are made of pore-free, dense metal.*

similar structures in pure copper Young's modulus of 132 ± 6 GPa is obtained, to be compared with 128 GPa [191]. This shows that the process produces metallurgically sound metal, the flow stress of which can be tailored by alloying. Hardness values were similarly collected, with the consideration of possible size-effects (data in Tables 3.1 and 3.2) [192, 193].

Sample <Orientation>	E (GPa)	STD	H (GPa)	STD
1 <112>	82.4	0.8	1.03	0.04
2 <213>	84.0	0.5	1.07	0.03
3 <213>	84.3	0.4	1.04	0.01
4 <213>	86.0	0.8	1.08	0.04
5 <213>	84.5	0.8	1.04	0.02
6 <212>	83.4	0.9	1.00	0.02
Mean	84.1		1.04	
STD	1.2		0.03	

Table 3.1: *Measured elastic modulus (E) and hardness (H) values for silver trusses produced by microcasting. Four indentations were performed on each specimen. The standard deviation (STD) measured on each sample and the crystallographic orientation along which the sample was indented are indicated.*

Sample <Orientation>	E (GPa)	STD	H (GPa)	STD
1 <304>	135	3.0	1.54	0.06
2 <101>	137	2.5	1.56	0.07
3 <113>	122	2.6	1.54	0.08
4 <113>	132	6.1	1.82	0.25
5 <304>	134	3.6	1.76	0.20
Mean	132		1.64	
STD	6		0.13	

Table 3.2: *Measured elastic modulus (E) and hardness (H) values for copper trusses produced by microcasting. Four indentations were performed on each specimen. The standard deviation (STD) measured on each sample and the crystallographic orientation along which the sample was indented are indicated.*

Figure 3.3E shows a cross-section through a similar structure made of pure silver; as seen, the metal is dense, or in other words exempt of pores. To check that there is no significant chemical interaction between the mold and the metal, we investigated whether there was a penetration of the metal atoms into the glass matrix using energy-dispersive X-ray spectroscopy (EDS) measurements across sections of infiltrated beams, still embedded in its fused quartz mold, near the host-substrate/metal interface. No new phase, and no traces of metal within the fused quartz host, were detected (see Figure 3.4).

Figure 3.5A exhibits an array of silver pyramids, each ending in a much thinner filament, 30 μm-long and $\simeq$2 μm in diameter. The silver substrate was removed by mechanical grinding to obtain, as in Figure 3.1 Step 6A, a final product consisting of the 6 mm-diameter, 800 μm-thick, fused quartz substrate containing an array of embedded silver pyramids each topped by this thin, antenna-like, coaxial filament. This demonstrates that the combination of laser-patterning and infiltration characteristics of the process provides a pathway for the production of multiscale 3D structures that would be difficult if not impossible to achieve by other means. As another prototype giving an example of the innovation potential of the technology, Figures 4B-D show a 3D-array of high-aspect-ratio multiscale silver-copper alloy microelectrodes that are left embedded in the fused quartz mold (visualized here by observation through the glass).

The minimum distance between electrodes is about 6 μm and the total structure length is 5 mm (leading to an aspect ratio of the glass slit between electrodes that exceeds 800). Being able to produce such arbitrarily shaped 3D highly conductive electrodes embedded in a high dielectric constant material host is highly interesting in numerous fields of microtechnology: e.g., implantable devices in medicine, or components for high-voltage, high-frequency electronics.

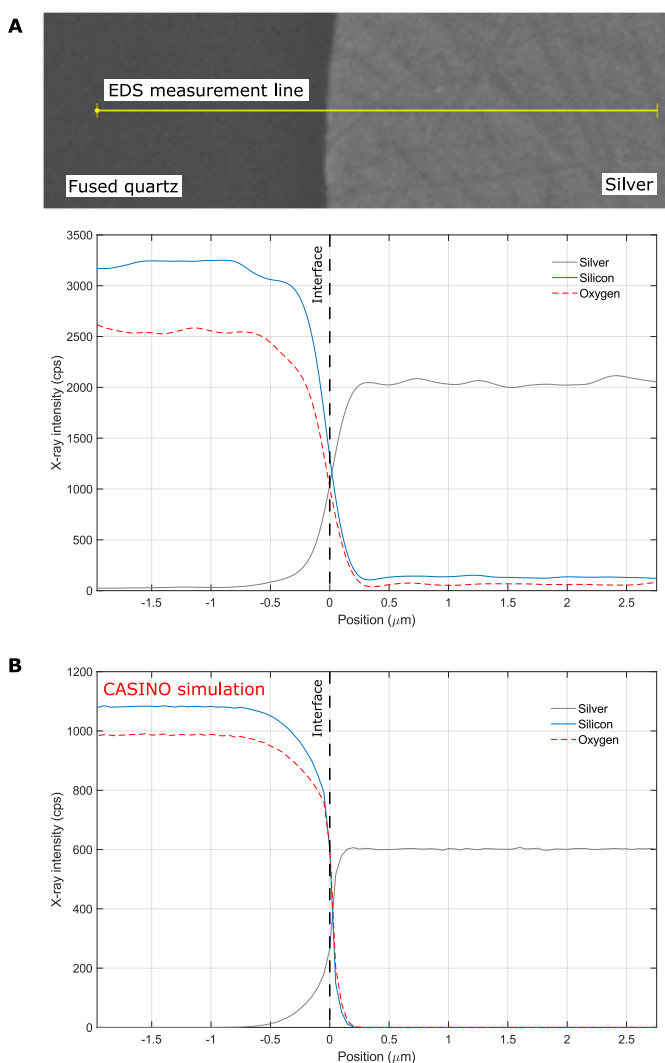Figure 3.4: *Chemical composition analysis normal to the metal/silicon dioxide interface of a sample similar to the one in Figure 3.3, but made of silver. (A) SEM image of the sample's portion analyzed and measured EDS X-ray intensity versus detection position; post-process averaging has been performed on the data before plotting. (B) CASINO Monte Carlo simulation of X-ray intensity from a sharp* SiO_2/Ag *boundary.*
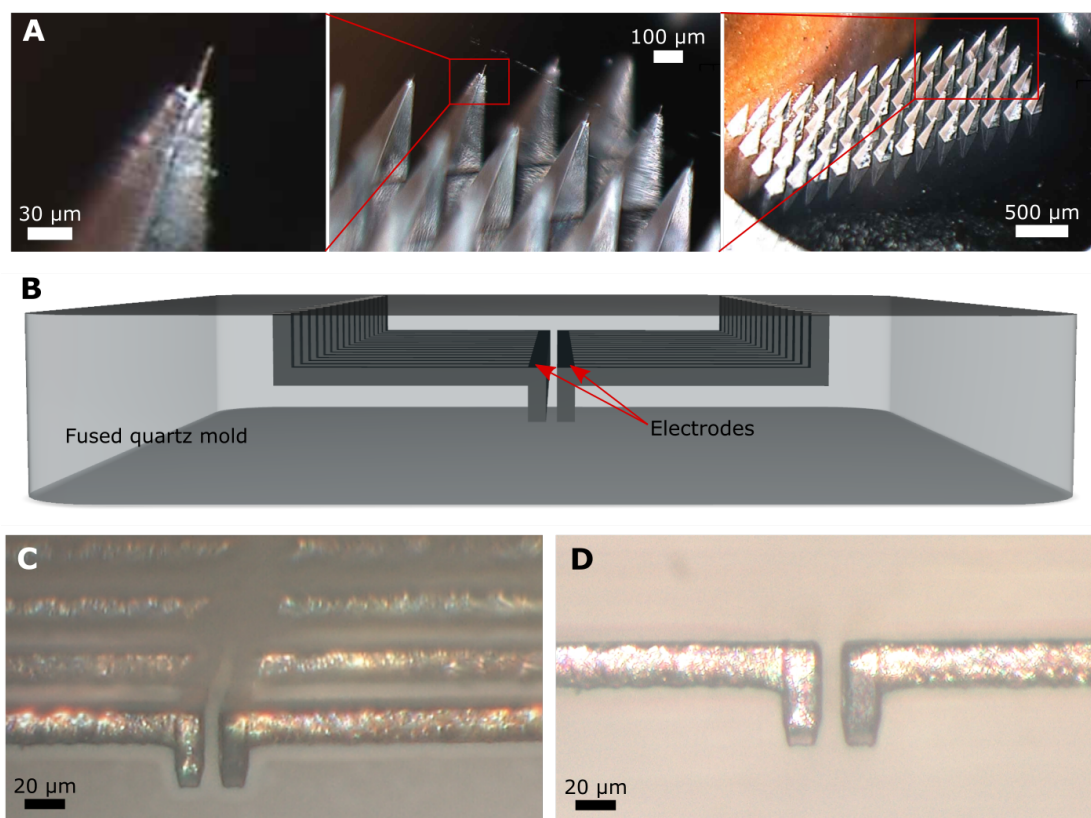
Figure 3.5: *(A) Optical micrograph of a silver pyramid array embedded in fused quartz, each pyramid ending with a thin antenna-like filament extending from its tip, illustrating the multiscale and multi-material capability of the process. (B), (C) and (D) are images of a row of electrode pairs embedded in fused quartz. (B) CAD model of the design (for the sake of clarity, the drawing is out of scale). (C) and (D) are optical micrographs of the resulting structures of $79\%_{wt}$ Ag-$21\%_{wt}$ Cu alloy embedded in fused quartz.*

Figure 3.6 shows a larger, geometrically complex, 3D (Maltese cross) structure fabricated out of copper or silver. Figures 5A-C show the structure still embedded within fused quartz, whilst Figure 3.6D shows the self-standing structure (here made of silver) extracted out of its mold. The beams composing the truss structure have a diameter around 50 μm, while the entire Maltese cross fits within an area of two-by-two millimeters. In this larger casting, there was a higher probability for solidification to nucleate and propagate from different locations of the mold, leading to a polycrystalline structure. Grain boundaries are indeed revealed by the trough that capillary forces have created along the beams composing the structure (Figure 3.6D). This is confirmed by EBSD, which shows the presence of three crystals in the imaged structure, grain boundaries of which are consistent with the location of grain boundary grooves visible in the SEM micrograph. Figure 3.6C shows a larger version ($\simeq$4 x 4 mm) of the same design, this time infiltrated with pure copper and left embedded in fused quartz.

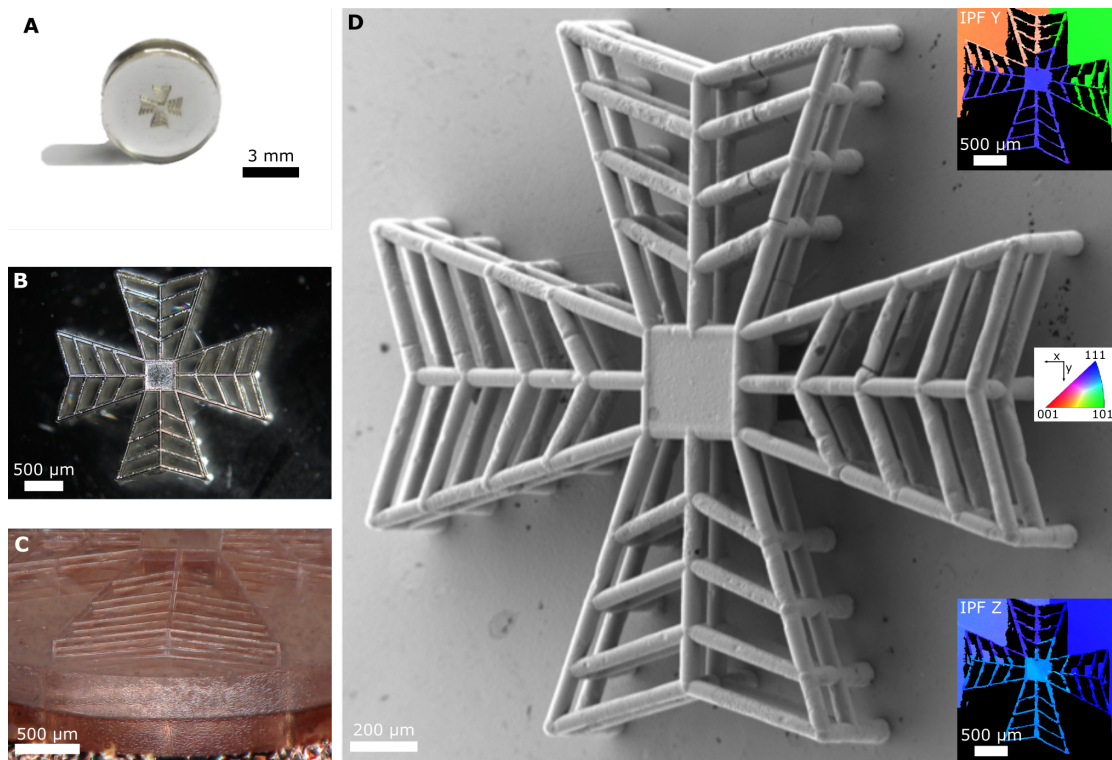Figure 3.6: *Complex (Maltese cross) 3D structure produced in pure silver and pure copper. (A) and (B) optical images of a silver cross embedded within its fused quartz mold. (C) Macroscopic image of a larger version of the same design produced in copper, also still contained within its fused quartz mold. (D) SEM image of the silver cross in (A) and (B) after mold removal. The related IPF images show the presence of 3 distinct grains, whose boundaries are made visible in the SEM image by the typical groove they have created along the casting surface.*

3.5 Discussion

Structures produced in this work, of size ranging from a few tens of micrometer to a few millimeters and with features of size down to around 2 μm, are made out of engineering metals (silver, copper and gold and their alloys) that are among the best electrical conductors and the most corrosion-resistant metals – features of interest for microtechnology in general. It will easily be appreciated that producing those structures would at best be difficult using existing technology, with one exception, namely local electrodeposition. Micromachining would not carve out the space between the tables and the chairs, or between them and the floor of the classroom of Figure 3.2. Layer deposition processes would not, unless the part was of dimensions far above the voxel size, produce in-plane beams of circular cross-section such as those in Figure 3.6. Processes that produce rapidly porous and/or binder-containing metal structures that require subsequent sintering and/or debinding would be unlikely to leave the thin table or chair structures unwarped after annealing. The only process that we believe could rival or surpass what is presented here is local electroplating, as this process also

produces dense metal with nearly total shape flexibility (such processes might, however, be challenged by the sharp, 90° corner, overhangs present in structures of Figures 2, 3 or 5).

As with any process that aims at broad acceptance and potential industrialization, achievable production rates are important. In producing silica molds in larger quantities, the laser-exposure time is the main bottleneck. The time needed to produce the mold for samples presented here was, with laboratory tooling used in this study, on the order of a day for a part such as the Maltese cross in Figure 3.6. In our laboratory, etching represented most of this time. In a production environment, however, the etching process is low-cost and usually parallelized, such that it does not represent an intrinsic limitation on production rates. Casting, meaning pressure infiltration followed by metal solidification, is a relatively rapid process already capable of high production rates; it, too, can be massively parallelized, since larger molds each containing many castings can be infiltrated, solidified, and retrieved simultaneously. Femtosecond laser exposure is therefore the rate-limiting step of the present process if production runs reach sufficiently high volumes.

The femtosecond laser-exposure process can be seen as moving an ellipsoid-shaped interaction zone (resulting from a non-linear laser-matter interaction) across the glass structure to be carved; in our set-up, motion is driven by linear-motor moving stages. The shape and size of the laser-affected zone within the glass depend critically on the focusing conditions, i.e. the numerical aperture of the focusing objective as well as the laser wavelength and the pulse energy. With our apparatus, at the finest level of focusing, we can produce an ellipsoid of diameter $\simeq 2 \ \mu$m on its short axes and length 8 μm on the long one. The velocity of the motorized stages is coupled to the laser pulse repetition rate to optimize the etching rate, as this depends strongly on the deposited energy (or dose, typically expressed in J/mm^2) [137]. Exposure parameters are set by several considerations. On one hand, thermal diffusion beyond the LAZ should be avoided; this limits the repetition rate to a maximum of about one MHz, which is the onset for thermal accumulation in fused silica [41]. Then the optimal deposited energy is set to a value of $\simeq 1.5$ J/mm^2 to achieve the highest etching contrast between laser affected zones and pristine material when using HF, KOH, or NaOH as etchant [98]. Considering a repetition rate of 900 kHz, the maximum optimal writing speed is $\simeq 150$ mm/s [137]. This is a very high value, such that operationally it is inertia and in turn the achievable acceleration of the motorized stages used here (maximum acceleration of $\simeq 50$ mm/s^2) that will confine the maximum attainable speed for μm-scale patterns to values well below the above limit. This adds a dependence of the maximum average glass pattern printing velocity on the intricacy of the pattern. For example, to pattern the structures in Figure 3.2 and 3.6, the average speeds of our stages were $\simeq 1.0$ and $\simeq 1.45$ mms^{-1}, respectively; however, these values are defined by technical limitations of our setup. Other commercial motorized stages can reach accelerations of around 10 m/s^2. This would result in average writing speeds of $\simeq 14.1$ and $\simeq 20.1$ mm/s for the previous examples.

Additional features of the process are also to be noted, on both fronts of limitations and potential. Pressure infiltration is, as expected, capable of intimately replicating nanometric features. The minimum channel size that can be infiltrated is ruled by the pressure required to overcome the molten metal surface tension that opposes its flow into tiny mold cavities.

This is given by the Young-Laplace equation [118], according to which the capillary pressure differential roughly equals the metal surface tension divided by the channel width. Surface tensions of most metals are on the order of 1 J/m^2; hence, a pressure of 10 MPa, which is technically achievable, should drive metal into features as fine as 100 nm. This is in keeping with the observed fidelity with which the infiltrated metal reproduces the carved glass structure in samples of this work.

The present process is therefore limited in terms of resolution by the controllable size of the LAZ which, due to the non-linear nature of the process by which it is formed, can itself be significantly smaller than the optical waist in the focused path of the laser beam (in our case ≃1.8 μm at a laser wavelength of 1030 nm) as illustrated elsewhere [194]. In its versions presented here, the process has a resolution of 2 μm; however, for these reasons, this may be reduced in future work. For example, an additional approach to reducing the laser beam waist further, and in turn, the size of the laser affected zone, is to use shorter wavelengths, for instance by frequency doubling or tripling common Ytterbium-based laser sources, reaching out to the UV exposure regime.

A limitation of the present process is that it is a priori not amenable to process alloys that contain elements, the oxide of which is more stable than silica (for example aluminum, titanium, or magnesium) or to process metals with melting temperature higher than the mold annealing temperature, ≃1200°C for fused quartz. It also tends to produce large-grained structures, which have advantages (e.g., high conductivity) and disadvantages (e.g., absence of grain boundary hardening or the formation of visible grain boundary grooves along the metal surface; see Figure 3.6D). Finally, the process is well suited for the production of multiscale structures (as in Figure 3.5) and it offers, when making multiscale structures, the scope for efficiency gains in production if laser parameters are dynamically adjusted during printing. One could indeed dynamically alter lens parameters (for example by using a spatial light modulator) and beam energy, so as to vary both the laser spot shape and size while maintaining optimal exposure conditions. This possibility might largely increase the volumetric speed and so provide opportunities for the rapid production of multiscale structures. For example, just by tuning the beam energy, the ellipsoidal LAZ can vary from ≃1 to ≃2.5 μm and from ≃8 to ≃20 μm in short and long axis dimensions, respectively; this corresponds to an order of magnitude (dynamic) change in voxel volume [194].

Building on the extensive survey of metal freeform microfabrication that is given in Ref. [171], the production speed of the microcasting process presented here is compared in Figure 3.7 with alternative 3D metal freeform manufacturing techniques. Specifically, in Figure 3.7A, the fabrication speed is normalized by the voxel size, which is in essentially all such processes assumed to be a cylinder with a diameter equal to the dimension read in the horizontal axis. Assuming a roughly equiaxed cylinder, one can obtain estimations of the volumetric production rate (for a more detailed description we refer to [171]). As seen, comparing feature sizes and production rates of the present process with current alternatives places it in the top right corner, showing that it stands out in terms of achievable production speeds. Such higher fabrication rates enable the industrialization of the process and the large-scale production of 3D components.
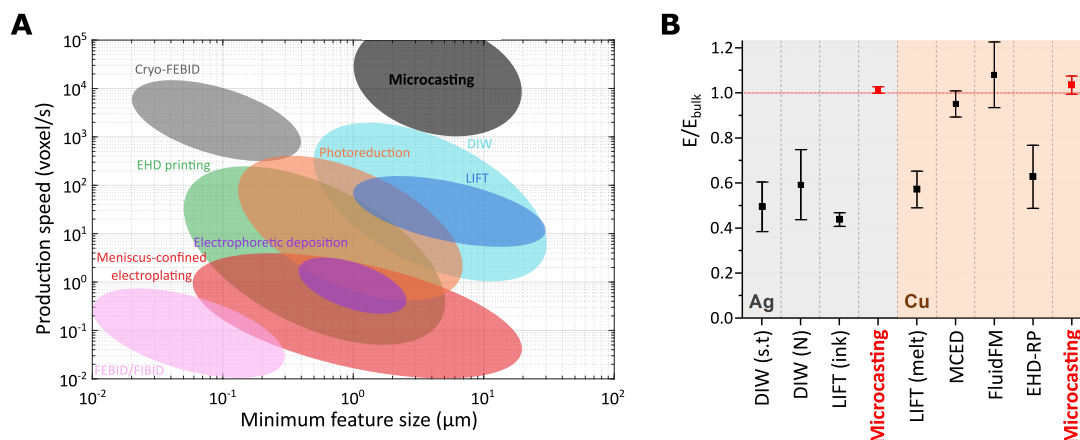
Figure 3.7: *(A) Qualitative comparison of achievable production speeds with alternative 3D freeform metal microfabrication processes (Redrawn from [171]): Direct Ink Writing (DIW), Electrohydrodynamic Printing (EHD printing), Laser-Assisted Electrophoretic Deposition, Laser-Induced Forward Transfer (LIFT), Meniscus-Confined Electroplating, Laser-Induced Photoreduction, Focused Electron/Ion Beam Induced Deposition (FEBID/FIBID), Cryo-FEBID. (B) Comparison of measured elastic modulus normalized by theoretical elastic modulus obtained by different techniques on silver and copper structures: DIW (shear thinning), DIW (Newtonian), LIFT (ink), LIFT (melt), Meniscus-confined electrodeposition (MCED), Confined electro-deposition in liquid (FluidFM), Electrohydrodynamic Redox Printing (EHD-RP). Error bars represent measured standard deviation. (Redrawn from [172])*

In parallel, Figure 3.7B displays a measure of the metal microstructural soundness, namely the ratio of measured to theoretical elastic modulus, for different techniques, using in this graph data and graph formats from Ref. [172], together with data for our samples reported in Tables 3.1 and 3.2. The pronounced porosity, and thus large spread in elastic properties, exhibited by most of the structures obtained by current micron-scale additive micromanufacturing processes other than local electroplating underline another major advantage of the microcasting process, namely the metallurgical soundness of the structures that it produces. For example, the electrical or thermal conductivity in metal structures produced by the present process will be as high as in the same pristine bulk metal, enabling micro-components and devices with optimal electrical or thermal performance. This is a feature that the present process only shares with electrodeposition, a process capable of finer resolution than the present process, albeit with far lower achievable production rates.

Moving forward, a few remaining challenges will have to be addressed for the present process to be improved or for it to enter commercial production. As seen, the pressure infiltrated metal reproduces with precision even minute details, below 100 nm in size, along the inner mold surface, see Figure 3.3; thus, improving the roughness of the molds is the next step in producing even smoother micro-cast products. A challenge, omnipresent in metal casting, is feeding solidification shrinkage of the metal. At the macro-scale, there are well-known recipes to this end, directional solidification towards a riser being one of the main approaches. In the present instance, given the far smaller part dimensions, the influence exerted by capillary

forces may still cause the formation and retention of tiny pores within the metal (perhaps cavities outlined in Figure 3.3 are of this nature) or may lead to other defects, such as the grain boundary grooves apparent in Figure 3.6. Finally, mastering the inner microstructural development of micron-scale cast metals and alloys is an area where much remains to be learned.

3.6 Glass-metal composites

In the context of enabling the fabrication of freeform glass-metal composites, we defined two procedures to produce both metal parts surrounded by a glass shell and glass parts surrounded by a metal layer.
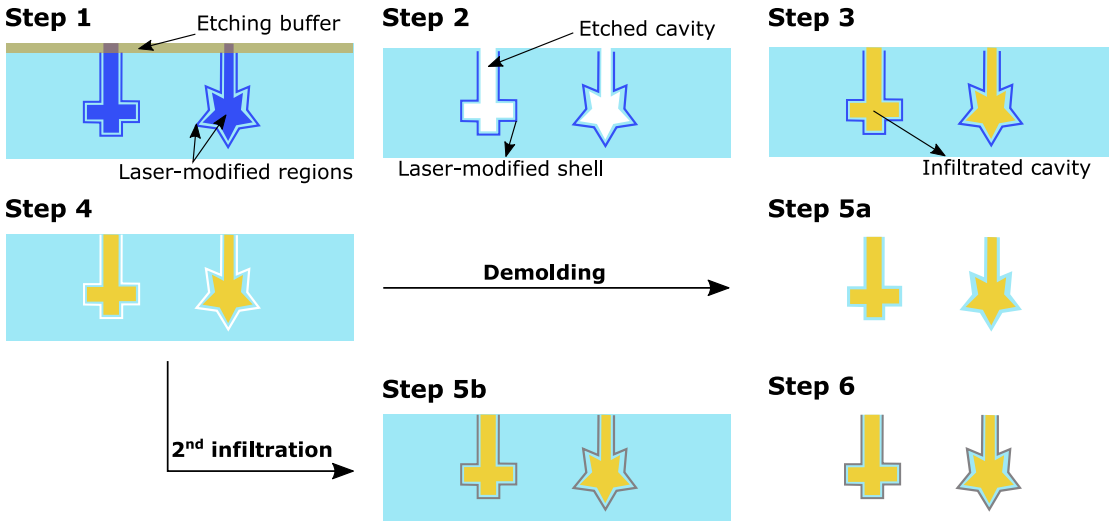
Figure 3.8: *Schematic of an infiltration technique based on sequential etching steps. Step 1, a 3D pattern is inscribed in the glass with a femtosecond laser, leaving an etching buffer preventing the contact with the etchant for the region to be etched only after the first infiltration. Step 2, the modified region exposed to the etchant is removed, resulting in empty cavities. Step 3, metal is infiltrated inside the glass mold cavities. Step 4, after removing the etching buffer by polishing, the remaining laser-modified region is etched. Step 5a, glass metal composite components are obtained after demolding. Step 5b, alternatively to Step 5a, the cavities etched in Step 4 are infiltrated with a different metal. Step 6, after infiltrating two different metals separated by a glass layer, the resulting composites are freed from the glass mold.*

The first technique is based on sequential etching steps, as illustrated in Figure 3.8, and aims at producing metal parts surrounded by a glass shell. The first step consists of the laser modification of both the volume to be removed (and subsequently metal-infiltrated) and the surface that delimits the glass shell around the metal part (shown in blue in the schematic). It should be noticed that the laser patterned shell is (i) machined with a larger laser exposure dose of $\simeq$ 200 J/mm^2 to facilitate the survival of the laser modifications - i.e. the nanogratings - to the metal infiltration, which is carried on in few minutes at around 1100 °C; and (ii) not connected

to the outer surface of the glass substrate to avoid contact with the etchant during the first etching step. In this way, after the etching step, a glass mold with cavities for infiltration plus a pre-machined shell is produced. Then, the pressure-assisted metal infiltration is carried on as described above. Finally, after exposing the remaining laser pattern by polishing the excess glass, during a second etching step, it is possible to preferentially etch the laser-modified shell (step 4). At this point, through demolding either by dissolving or breaking the glass mold, freeform glass-metal composites are obtained (Step 5a).

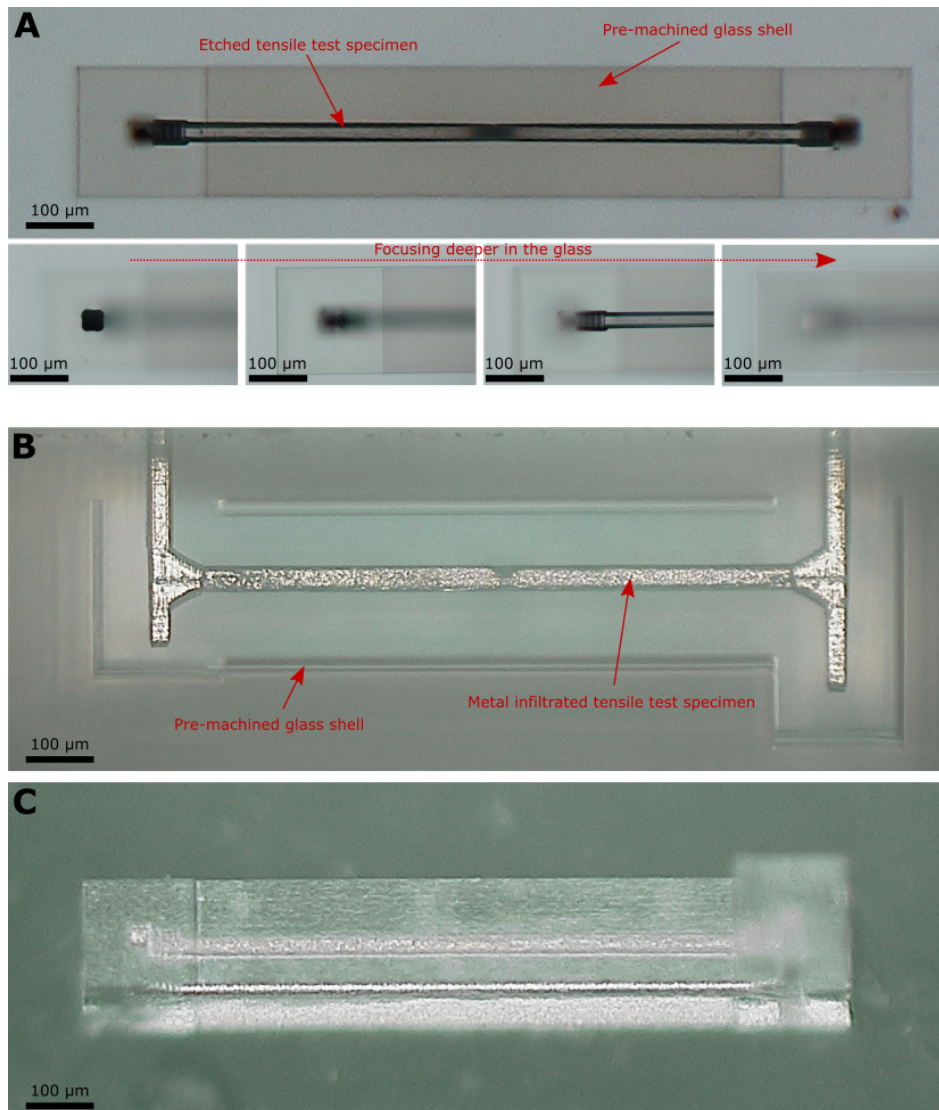Figure 3.9: *Optical micrographs at different fabrication stages of a metallic tensile test specimen surrounded by a glass shell. (A) Top view of the glass mold showing both the etched cavity and the pre-machined shell at different focal planes. (B) Lateral view of the glass mold after the metal infiltration of the specimen. (C) Picture of the final glass-metal composite product after demolding.*

As a proof of concept, we designed a tensile test specimen about 40x40 μm^2, 1 mm long, and surrounded by a glass shell ≃ 90 μm thick. Figure 3.9A shows a top view of the specimen after the first etching bath (Step 2 in Figure 3.8), while Figure 3.9B displays a lateral view of the mold after pure silver infiltration (Step 3 in Figure 3.8). Finally, in Figure 3.9C the final composite product is obtained by etching the laser-machined shell (Step 5a in Figure 3.8).

A variation of the sequential etching steps technique showed in Figure 3.8-Steps 5b&6 can be used to infiltrate different materials in the same substrate. In this case, instead of freeing the final composite product, the subsequent etching steps can be used to etch other pre-machined cavities that in turn can be infiltrated with new material. Even if theoretically there is no limit to the number of iterations of such a process, in reality, there are some limitations. Notably, (i) the order of infiltrations of different materials should go from the one with the highest melting point to one with the lowest to avoid re-melting during subsequent infiltrations; (ii) the different infiltrants should not react with one another; and (iii) the higher the number of infiltrations, the larger the dimension of the 'etching buffer'.

The second technique, designed to obtain glass parts surrounded by a metal layer, is illustrated in Figure 3.10. As usual, the first step consists in modifying glass regions with the laser, but this time the modification is limited to a surface and its design needs to take into account some fixing points to hold in position what will be the glass core of the final glass-metal composite during the metal infiltration (see inset in Figure 3.11C). During Step 2 the laser-machined surface is etched, and in Step 3 the metal is infiltrated in the cavities. At this point, after protecting with a photoresist the surface of the substrate containing the entries to the cavities (Step 4), by etching it is possible to release the glass-metal composites produced (Step 5).
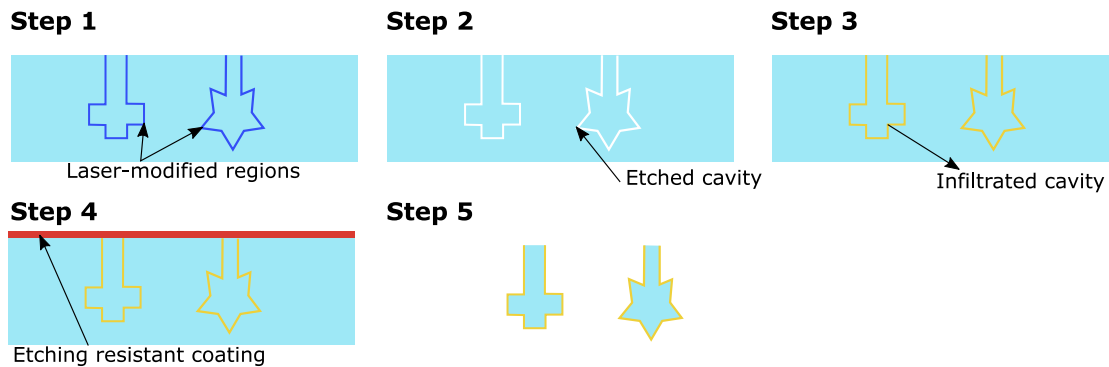
Figure 3.10: *Schematic of an infiltration technique to produce composites made of a glass core and surrounded by a metal layer. Step 1, a 3D pattern is inscribed in the glass with a femtosecond laser. Step 2, the laser-modified region is removed by chemical etching. Step 3, metal is infiltrated inside the glass mold cavities. Step 4, the top surface of the mold is protected with an etching-resistant coating. Step 5, the entire mold is dissolved, resulting in the final composite products.*

In Figure 3.11A, a device similar to the one of Figure 3.9 is machined and etched. Then, the resulting cavities are infiltrated with pure silver (see Figure 3.11B). The outcome is a tensile

test specimen with a glass core and surrounded by a metal layer. With the same technique, a series of micro-pillars is also fabricated and shown in Figure 3.11C-D after etching and metal infiltration, respectively.
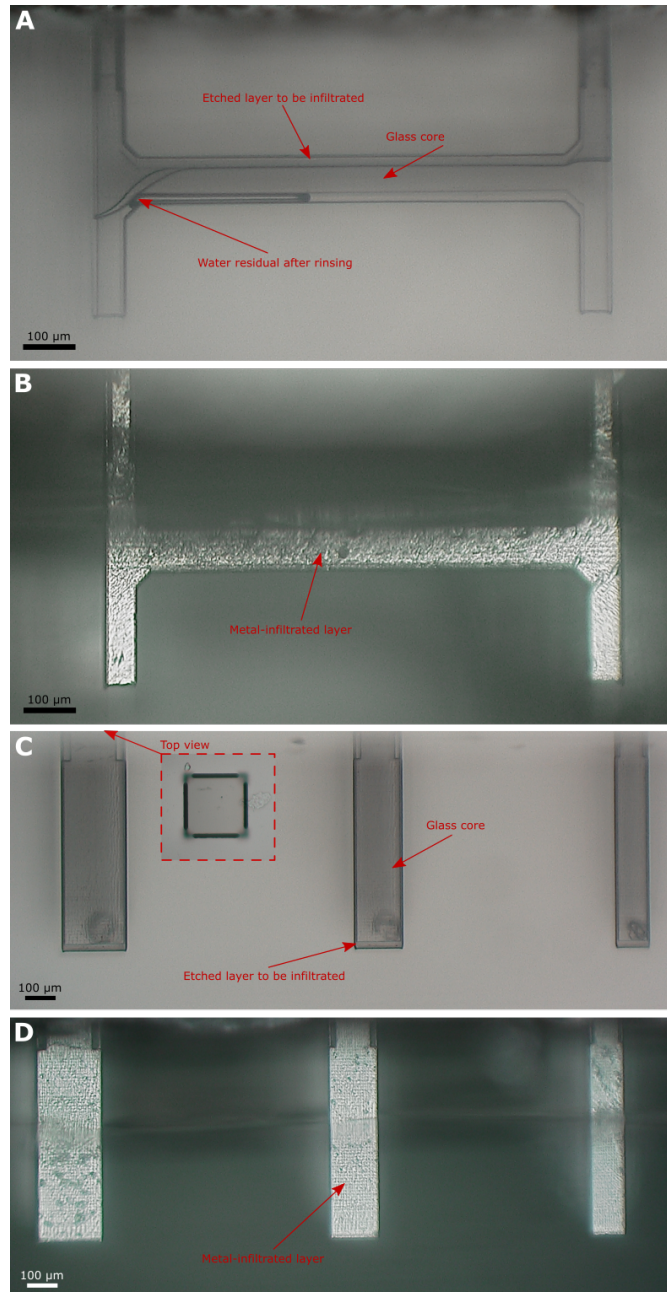
Figure 3.11: *Optical micrographs of composite structures with a glass core and a metal layer around. (A) and (B) tensile test specimen after etching and after metal infiltration, respectively. (C) and (D) set of pillars after etching and after metal infiltration, respectively. The inset in (C) shows the top view of the left pillar, to highlight the fixtures that hold the glass core during metal infiltration.*

3.7 Summary and conclusion

In conclusion, we have demonstrated that geometrically complex interconnected multiscale components up to a few millimeters in size and freely shaped to micrometric resolution can be made of fully dense metal via a novel, freeform manufacturing process that combines fs-laser glass micromachining with metal pressure infiltration. The process is suited for engineering metals that are inert in contact with silica, including silver, copper, gold, and their alloys, and has the potential for higher large-scale production rates compared to existing technology. The resulting glass/metal combinations enable new device architectures for applications in a wide range of areas in microtechnology. Alternatively, by mold dissolution, this process fills a gap in microfabrication because it gives the ability to turn, as is done at the macro-scale, to casting when monolithic metallic parts of high geometrical complexity are to be produced.

4 Glass-in-glass infiltration

Chalcogenide glass exhibits a wide transmission window in the infrared range, a high refractive index, and nonlinear optical properties; however, due to their poor mechanical properties and low chemical and environmental stability, producing three-dimensional micro-structures of those glass remains a challenge. Here, we combine the fabrication of arbitrarily shaped three-dimensional cavities within fused silica molds by means of femtosecond laser-assisted chemical etching, with the pressure-assisted infiltration of a chalcogenide glass into the resulting carved silica mold structures. This process enables the fabrication of 3D, geometrically complex, chalcogenide-silica micro-glass composites. The resulting products feature a high refractive index contrast that enables total-internal-reflection guiding, and an optical quality roughness level suited for applications in the infrared.

4.1   3D micromanufacturing of glass

The use of glass has been ubiquitous in optics since the dawn of the discipline: the combination of two glass with different properties into a single product has been practiced since the late XVIIIth century, both for decorative and scientific purposes. Continuous progress and research in glass science have led to the discovery of a broad variety of glass compositions and formulations covering a wide range of useful physical properties, e.g. transparency spectral window, chromatic dispersion, linear and non-linear refractive indices, surface scratch resistance, brittleness, chemical stability, etc., which have found countless applications in optics and beyond. Yet, as a result of this broad spectrum of properties, great variability in processing methods and their outcomes remains. Specifically, forming glass in complex shapes at the microscale remains challenging, in particular for infrared glass that are notably often fragile and difficult to process.

Combining different glass into one product has been of great interest in early glass craftwork for decorative purposes. Venetians refined and magnified ancient work developing processes such as the *murrina* and the *millefiori*, which remain even nowadays iconic references for ornamental glass manufacturing [195–197]. In parallel, late-XVIIIth century scientific glasswork led to the discovery of achromatic optics ('Crown-Flint' doublets) [198]. The ability to produce freefrom glass-glass composites by novel methods capable of greater geometrical freedom of design than is currently possible could trigger optical component innovations with functionalities that leverage the individual physical properties of its basic constituents. This would offer novel design opportunities, in particular for further miniaturization and system integration. We present here a process allowing for the three-dimensional micro-scale integration of two glass with radically different physical properties. We illustrate this generic concept with free-form chalcogenide glass structures embedded in a fused silica matrix.

Chalcogenide glass has attracted much attention in the last few decades because their exceptionally wide optical transmission window in the infrared and their high nonlinear refractive index [199], for both passive [200, 201] and active [202, 203] photonic applications. Unfortunately, due to their poor mechanical properties and weak chemical and environmental

stability [204, 205], three-dimensional structuring, integration, and packaging of those glass remain challenging tasks. Current pathways to chalcogenide glass fabrication include the production of optical fibers and deposition processes. Chalcogenide glass fiber production was first reported in the 1980s [206] and continues, as such fibers have multiple applications, from sensing to telecommunications [199, 207, 208]. Photonic crystal fibers (PCFs) combining chalcogenide or tellurite glass into silica were produced by a pressure-infiltration technique, exploring both the process and optical properties of the resulting structures [209, 210].By this route, several centimeters long PCFs containing chalcogenide rods down to sub-micron diameter were manufactured [209–212]. Deposition processes such as chemical vapor deposition [213], physical vapor deposition followed by glass melting over etched silicon [214], sputtering [215], and pulsed laser deposition [216] are employed in applications for optical circuits, which require planar waveguides and components. Chalcogenide glass components such as lenses are currently fabricated by glass molding [217] and high-precision diamond-turning [218], restricting shapes to specific 3D geometries [219]. Recently, attempt to 3D print of chalcogenide using the fused-deposition technique applied to fiber preforms in As_2S_3 (one of the commercially available chalcogenides) has been reported [220–222]. This approach remains limited in resolution by the size of the filaments, which currently constrains designs to millimeter-scale geometries and introduces discontinuity between printed layers, which may be detrimental for certain optical applications.

The process that we present here is based on pressure-assisted infiltration of As_2S_3 chalcogenide glass into a fused silica micro-mold fabricated by femtosecond laser machining followed by chemical etching. This method enables the fabrication of arbitrary three-dimensional glass-in-glass elements while maintaining micrometric resolution and sub-micron roughness. The two constitutive materials, fused silica and chalcogenide, offer a high-index contrast combination, in geometries and size scales suited for geometrically complex 3D mid-infrared optics based on total internal reflection optical design principles. In addition to its specific optical properties, fused silica can be used as a mechanically and chemically resistant support and protection for chalcogenide microstructures, and may itself contain additional features of interest for further integration and packaging [106, 223], such as waveguides [1] or flexures [101].

4.2   Process concept

The fabrication process, similarly to its metals infiltration counterpart [129, 224], consists of two main steps. First, the fused silica micro-molds are machined using femtosecond laser modification followed by wet chemical etching (Figure 4.1A-B), according to a process described elsewhere [3, 19]. We use in the present work a Ytterbium-fiber amplifier laser emitting 270 fs pulses at a repetition rate of $\simeq$ 300 kHz, with a pulse energy of 220 nJ. The laser is focused to a measured optical waist of about $\simeq$ 2 μm using a 0.4-numerical aperture objective. The substrate used is UV-grade fused silica (Corning 7980 0F). Following laser exposure, the specimen is etched in a 5 wt% NaOH bath for several hours [98]. Then the

micro-mold is positioned in a glass crucible with the chalcogenide glass As_2S_3 (IRG27, from Schott) to be infiltrated resting on top.

The crucible-glass combination is placed in a pressure infiltration furnace, and then brought to low vacuum ($\simeq$ 0.02 mbar) while the temperature is raised to 600°C (well above the transition temperature of IRG27 at 200°C), according to values previously reported [210]. Thus, the chalcogenide is melted to a liquid form that covers the mold cavities (Figure 4.1C). Note that, given that the chalcogenide glass As_2S_3 contains arsenic, it is important to prevent at this stage of the process any contamination of the furnace by arsenic that may have evaporated while the glass is molten. It is therefore advised to surround (as depicted in Figure 4.1C&D) the molten glass with an inner enclosure within the pressure infiltration furnace, so as to prevent any transfer of arsenic to the furnace.
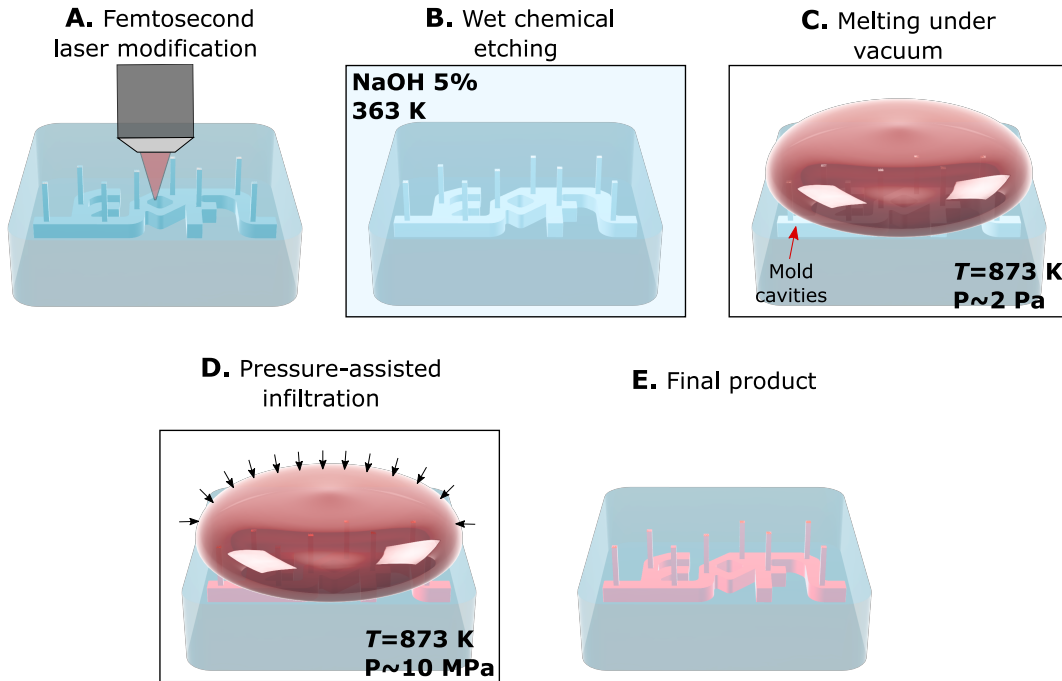
Figure 4.1: *Schematic of the micro-infiltration process. (A) A 3D pattern is inscribed in a fused silica substrate with a femtosecond laser. (B) The glass substrate is etched to remove the laser-irradiated regions. (C) The substrate is placed in a chamber with the glass to be infiltrated on top, the chamber is evacuated and the temperature is raised above the transition temperature of the infiltrant. (D) Pressurized inert gas is let into the chamber (but not mold cavities, which are sealed by the molten glass) and pushes the molten glass into the substrate cavities against capillary forces. (E) A final glass-in-glass composite product is obtained, shown here after removal of the remaining glass drop resting on top of the substrate.*

Then, to force the glass into the mold, a pressure of 10 MPa is applied hydrostatically with Argon gas leaked into the chamber, causing the molten chalcogenide glass to infiltrate the cavities underneath (Figure 4.1D). Finally, the sample is cooled down while maintaining the pressure. After removing the excess chalcogenide by polishing, a final product combining

3D chalcogenide microstructures in fused silica is obtained (Figure 4.1E). A post-processing annealing step is also implemented to minimize –H and –OH bonds and to ensure stress relaxation [34]. Namely, to obtain a high transmission and to avoid crystallization, the specimens are annealed in an inert atmosphere (i.e. nitrogen) at 150°C for 1 hour using a heating and cooling rate of $\simeq 1$°C/min [225–227].

4.2.1   Materials characterization

Optical micrographs are taken with a Hirox digital microscope KH-8700 (Tokyo, Japan) using the Köhler illumination method and, in the case of Figure 4.4E, with a standard linear polarimetry scheme. The samples are polished with diamond lapping films until an optical surface quality is obtained, then they are coated with carbon thin film for high-resolution imaging and elemental analysis with a field emission scanning electron microscope Zeiss SEM Gemini450 (Oberkochen, Germany) equipped with energy-dispersive x-ray spectroscopy (EDS). Images are obtained at 5 kV and elemental analysis is performed at 20 kV.

A Raman spectrometer, LabRam HR from Horiba (Kyoto, Japan), equipped with a 633 nm laser excitation source attenuated down to 4 mW (to prevent damaging the specimen) is used. The linearly polarized Raman laser beam is focused at the surface of the specimen using a 100x and 0.9 numerical aperture objective from Thorlabs (Newton, NJ, USA). Raman spectra at various points are collected at room temperature with an acquisition time of 30 seconds for each point. Spectral transmission data in the visible and near-infrared spectrum (from 350 to 800 nm) are taken with a Perkin Elmer spectrometer Lambda 950 (Waltham, Massachusetts, USA). A mask with a hole of around 90x90 μm^2 is prepared in fused silica using the femtosecond laser machining plus etching process described above, and then coated with aluminum for broadband reflectance. For the measurement, the reference beam power is attenuated to 1 %, to compensate for the presence of the mask and the ensuing effective drastic reduction of the beam size from the original 2 cm in diameter.

A CO laser (model C55 from Coherent, Santa Clara, California, USA) emitting at 5.55 μm is used to measure the transmission efficiency in the mid-infrared spectrum. The power transmitted is filtered with a bandpass filter (FB5500-500 from Thorlabs, Newton, NJ, USA) and is measured with a high sensitivity thermopile sensor (XLP12-3S-H2-D0 from Gentec-EO, Quebec, QC, Canada).   The light-guiding properties of the long channels in Figure 4.2C are tested with an optical set-up comprising a quantum cascade laser (QCL) operating in continuous wave at 8.3 μm with 100 mW of output power, a set of two mid-IR lenses with anti-reflective coating with a focal length of 4 mm (C036TME-F from Thorlabs, Newton, NJ, USA) used for in and out coupling the laser beam, a long wave IR camera (A400 from Teledyne FLIR, Wilsonville, OR, USA) to measure the radiation and scattered light, and a beam profiler working in the range from 2 to 16 μm (WinCamD-IR-BB from DataRay, Redding, CA, USA) to measure the beam profile of the out coupled light.

4.3 Results and discussion
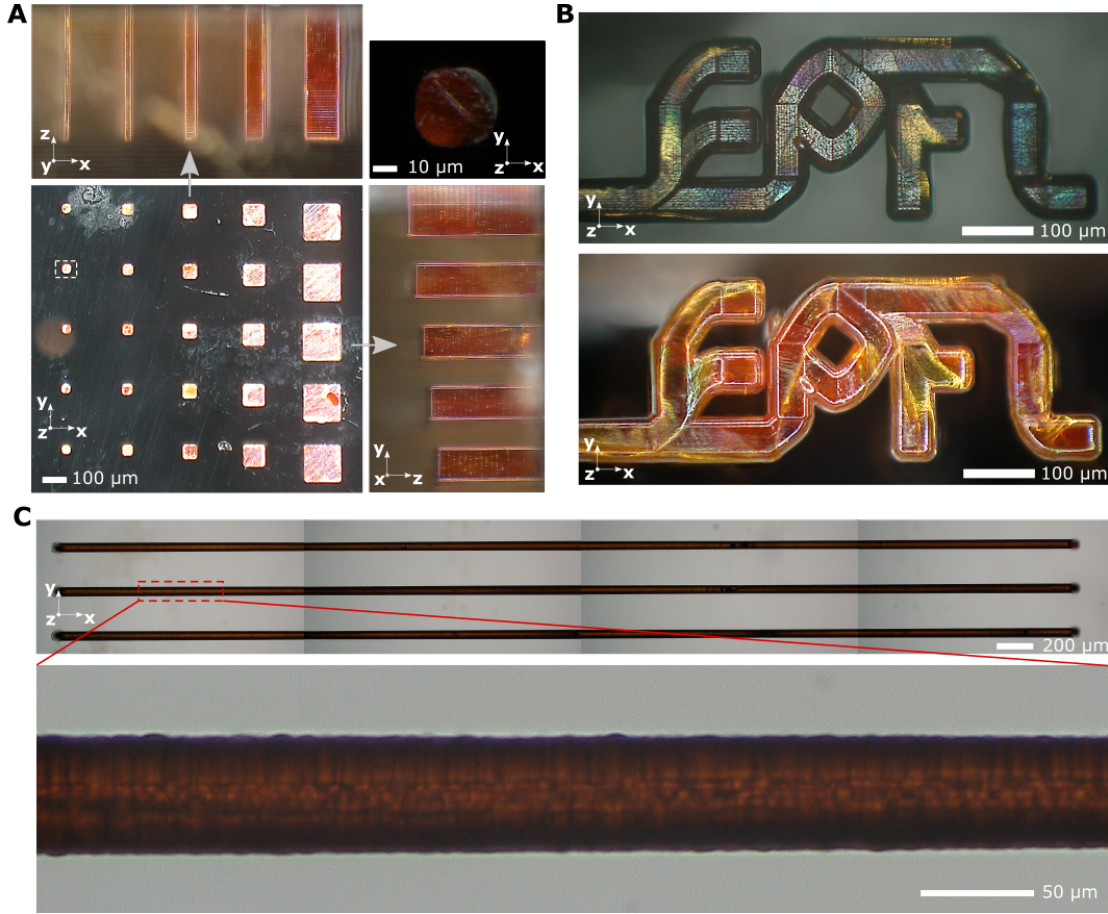
Figure 4.2: *Optical micrographs of different chalcogenide structures infiltrated into fused silica. (A) A set of pillars of different dimensions with a zoomed view (top right) of the pillar framed in the white dotted rectangle, representing the smallest cavity infiltrated in this work. The lateral view images are in scale with the related top view micrograph. (B) A complex 3D shape in dark and bright field illumination, and (C) overview (top) and magnification (bottom) of infiltrated channels 4 mm long and around 50 μm thick and wide (four micrographs are stitched together to form the figure).*

Figure 4.2 displays optical images of structures produced with the presented process. Figure 4.2A shows a set of pillars with dimensions ranging from 30 to 150 μm laterally and from 400 to 500 μm in height. The 'EPFL' logo in Figure 4.2B demonstrates the production of complex geometries out of chalcogenide glass at the microscale, while the long channels in Figure 4.2C show an aspect ratio (here defined as length over thickness) of around 80, thus demonstrating a structure that might be used as an infrared waveguide embedded in a fused silica substrate. Trapped gas bubbles found in the chalcogenide glass infiltrated PCFs [209–212] were not observed here. However, we note that structures infiltrated here are not as spectacularly long as those achieved in fiber infiltration and that the infiltration conditions are not the same. Namely, the mold is at constant temperature (i.e. no thermal gradient as in

the long PCFs) and the infiltration chamber is evacuated prior to melting and pressurization, so that there is no gas trapping in the present experiments. Cracks might on the other hand be present in the complex geometry samples of this work, given the changes in hue of the chalcogenide glass in Figure 4.2B. It should be mentioned that the darker lines visible in Figure 4.2A-B are typical surface texturing due to the laser machining followed by chemical etching of the glass mold and therefore likely not defects from the infiltration process. The roughness of the structures is defined by the femtosecond laser machining of the mold and depends chiefly on laser parameters and the writing strategy used. When those are optimized, an average roughness of about 100 nm can be achieved [98]. Therefore, the structures produced by the presented method can fulfill optical quality requirements for applications in the infrared.

The samples of Figure 4.2A are characterized by performing both Raman and EDS to compare the pristine with the infiltrated glass. Raman analysis (Figure 4.3A) shows spectra for the fused silica substrate (in blue), the infiltrated chalcogenide (in red), the pristine chalcogenide (in dark grey), and the interface between fused silica and the infiltrated chalcogenide (in green). The Raman spectrum of the substrate matches with a typical Raman spectrum of fused silica. It shows the main band (ω_1), the symmetric stretching of the four-membered silicon-oxygen ring structure (D1), together with signatures of the three-membered silicon-oxygen ring structure (D2) and of the symmetric stretching mode of the Si-O-Si bridging bond in $Si(O_{1/2})_4$ tetrahedron network (ω_3) at 440 cm^{-1}, 490 cm^{-1}, 606 cm^{-1}, and 800 cm^{-1}, respectively [228, 229]. For comparison with the unmodified glass, the intensity of the D2 peak is measured relative to the ω_3 peak intensity, which is known to remain constant with respect to the overall Raman intensity [230]. The structure of glassy As_2S_3 consists mainly of $AsS_{3/2}$ pyramidal units linked by As–S–As bridges. The main band at 345 cm^{-1} is assigned to the symmetric stretching vibrational mode of $AsS_{3/2}$ pyramids [231]. Weak bands at around 185 cm^{-1}, 228 cm^{-1}, and 475 cm^{-1} are associated with bending modes in As-As homopolar bonds within As_4S_4 clusters and S_8 rings, respectively [232]. The atomic structure and related properties of the chalcogenide glass depend on the fabrication history of the glass. As seen in Figure 4.3A, there is no structural modification observed between pristine As_2S_3 and the pressure-infiltrated As_2S_3. This shows that the final product is a glassy material, similar to the raw material that was used for infiltration.

Finally, the Raman spectrum at the interface between the fused silica mold and the infiltrated chalcogenide structure is taken, with a goal to spot eventual oxygen and sulfur exchange. The sulfur oxygen vibrational modes were found in literature as follows: broad bands at 928 cm^{-1} and 620 cm^{-1} due to symmetric and asymmetric stretching of S-O and symmetric bending modes of O-S-O, respectively [233]; two broad peaks at 310 cm^{-1} and 370 cm^{-1} for the bending S-O vibrations [234, 235]; molecular SO_2 at room temperature O-S-O at 530-570 cm^{-1} [236]; and absorption bands at around 790 cm^{-1} and 800 cm^{-1} are due to oxygen impurity in As_2S_x glass [237]. No evidence of S-O bonds is observed in the measured spectrum, which displays a blend of chalcogenide and fused silica characteristic peaks.

From the scanning electron micrograph in Figure 4.3B of one of the finer infiltrated features
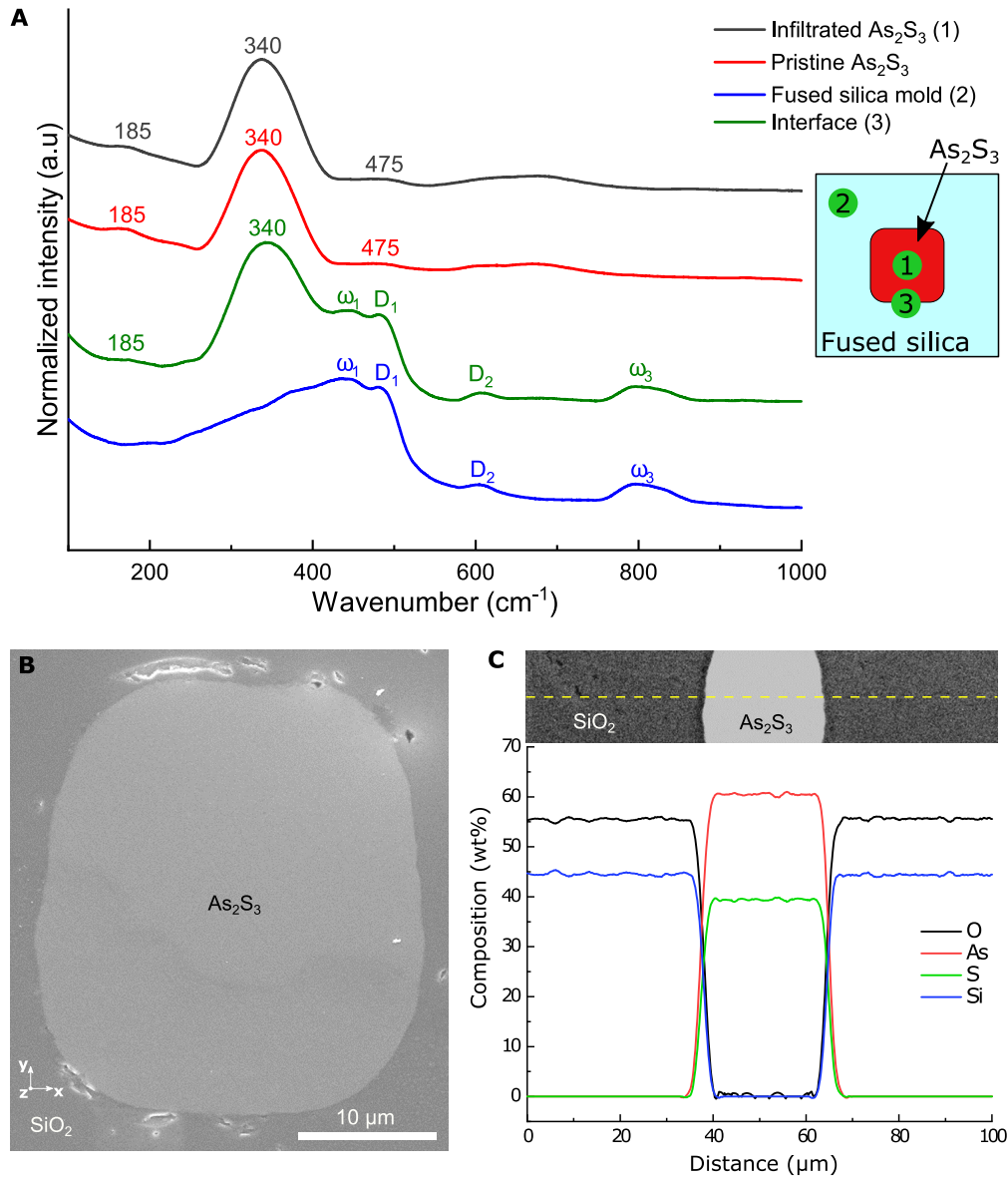
Figure 4.3: *(A) Raman spectra of fused silica mold (in blue) and both pristine and infiltrated* As_2S_3
*chalcogenide (in dark grey and red, respectively), and at the interface between fused silica and infiltrated
chalcogenide (in green). The inset shows a schematic representation of the location of the measurement
on the sample. (B) SEM micrograph of a cross-section of a chalcogenide filled channel in fused silica
(the stain on the chalcogenide was caused by the acetone used before the SEM characterization and
the particles on the surface are residues from polishing), and (C) EDS measurement of the chemical
composition of mold and* As_2S_3 *after infiltration.*

of this work (see the leftmost column in Figure 4.2A) one can conclude that an intimate, void-,
crack-, and reaction-free, sharp interface is formed between the chalcogenide glass and fused
silica, consistent with earlier investigations of As_2S_3 infiltration into fused silica [210]. The
same structure as in Figure 4.3B subjected to an energy dispersive x-ray spectroscopy analysis

gives results shown in Figure 4.3C. The chemical composition measurement confirms that the present infiltration process induces no change in stoichiometry, for both the infiltrated chalcogenide glass and the fused silica mold. In particular, the composition of As_2S_3 is found as 61.0 wt% arsenic and 39.0 wt% sulfur, which (considering the atomic weight of the components) gives an atomic ratio of arsenic to sulfur of 2:3 with a negligible error of 0.15 %. As for the Raman characterization, no evidence of species exchange between fused silica and chalcogenide is found. This suggests that there was no chemical interaction between the mold and the infiltrant. More advanced techniques such as transmission electron microscopy equipped with energy-dispersive X-ray spectroscopy (TEM-EDS), electron energy loss spectroscopy (EELS), or electron probe microanalysis (EPMA) could be used for higher accuracy measurements of eventual ion exchange.

After material characterization, the set of pillars shown in Figure 4.2A is polished to expose both top and bottom surfaces. Then, a spectrum analyzer is used to compare the transmission spectrum of pristine versus infiltrated As_2S_3. An ad-hoc mask is designed and machined in fused silica through femtosecond laser exposure followed by chemical etching, after which it is coated by sputtering with aluminum to obtain a broadband reflectance spectrum. The spectral transmission measurement is first calibrated with only the mask in place while attenuating the reference beam power to 1 %. Then, optical quality polished windows of pristine fused silica and of As_2S_3 having the same thickness as the target sample are placed behind the mask and analyzed. Finally, the fused silica mold with As_2S_3 infiltrated pillars is tested under the same condition, i.e. with the mask positioned in front to let the light pass through only one specific pillar (see Figure 4.4B-D) 500 μm thick and about 80x80 μm^2 in cross-section. In addition, to test the transmission with a mid-IR source, a CO laser beam is focused first on the mask alone and then with the sample behind the mask. For precise measurement, the power is filtered with a bandpass filter around 5550 nm before measuring with a thermopile sensor with a sampling rate of 0.1 Hz for 5 minutes. The averaged results give an initial power through the mask of around 2.4 mW that is then reduced to 1.4 mW when the sample is in place, resulting in transmission efficiency of about 58%. The results are shown in Figure 4.4A.

In general, for the measured wavelengths, the infiltrated chalcogenide transmission spectrum follows the same trend as its pristine counterpart, albeit with a decrease in transmission of around 20 %. We attribute the larger optical losses within the infiltrated sample to multiple factors, including the polished surface roughness, diffraction losses due to shape mismatch and/or alignment errors between the mask and the substrate, as well as the possible presence of micro-cracks or other small volume defects that cannot be totally excluded. Finally, the annealing conditions used here are probably different from those used by the glass manufacturer and it is known that the optimization of such post-process operations is of great importance for the performance of chalcogenide glass. For example, by applying a two-step annealing (soft baking and hard baking), both optical and structural properties of As_2S_3 microstructures can be enhanced [238], and optimizing the annealing temperature increases the IR transmittance in As_2S_3 thin films [225].
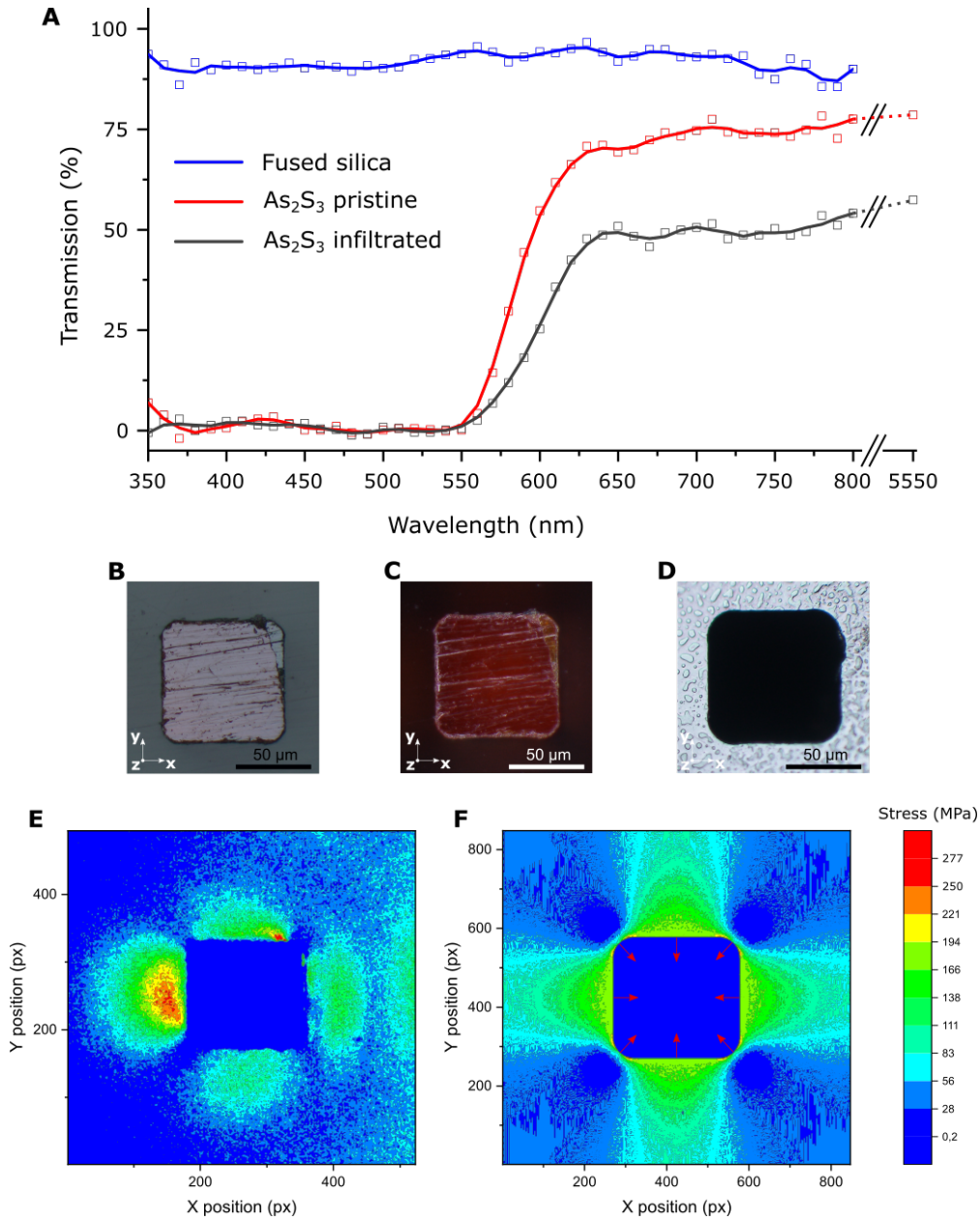
Figure 4.4: *(A) Spectral transmission measurements of fused silica together with both pristine and infiltrated* As_2S_3. *(B) and (C) optical micrographs of the chalcogenide infiltrated pillar (500 μm thick and about 80x80 μm^2 of cross-section) viewed in reflection, and transmission, respectively. (D) optical micrograph of the hole in the aluminum-coated mask (the stains in the picture are an unexpected feature of the aluminum coating). (E) Colored map of an optical micrograph in cross-polarized illumination of the tested pillar. (F) Colored map of a FEA simulation of the stress distribution in the XY plane for the geometry considered in (E), with a uniform 110 MPa pressure applied as indicated by the red arrows.*

Figure 4.4E shows the colored map of the pillar in a cross-polarization illumination setup, while Figure 4.4F illustrates the simulated stress distribution using finite element analysis

(FEA) within the same pillar. When subjected to mechanical stress, even isotropic materials such as fused silica become birefringent. Specifically, this stress-induced birefringence is linearly proportional to the stress state in the material. Here, we take advantage of this characteristic of the fused silica mold to *qualitatively* account for the presence of residual stress. Due to the photoelasticity effect, the brighter portions of the image in cross-polarizers indicate the presence of stress, with an intensity proportional to the light intensity. The presence of internal stresses within the glass near the interface confirms that, after infiltration, we obtain a composite with a strong, bonded interface between the two materials, as speculated from the SEM observations (see Figure 4.3B). We note that this result differs from what was reported in [211, 212], where a poor adhesion between As_2S_3 and silica was found. The reason for the difference remains unclear at this stage.

The presence of stress at the interface originates from the difference in thermal expansion coefficients (CTE) between the two materials, leading to a difference in shrinkage during solidification and cooling. In the simulation shown in Figure 4.4F, we estimate the difference in thermal shrinkage and the resulting level of stress by assuming a linear and isotropic behavior in the two materials, and finally, we apply the analytically computed stress uniformly (red arrows in Figure 4.4F) on the finite element model of the fused silica mold to obtain the actual stress distribution in the plane perpendicular to the light propagation, i.e. XY.

For the calculations, the coefficient of thermal expansion (CTE) and the Young modulus of chalcogenide glass are taken as $2.25 \cdot 10^{-5}$ K^{-1} and 16.6 GPa (from [239]), respectively; while for fused silica we use $5.8 \cdot 10^{-7}$ K^{-1} and 72.5 GPa (from Heraeus). The resulting thermal stress originating from the cooling and applied to the finite element model is estimated to be around 110 MPa. For certain geometries and cooling conditions, depending on its intensity, this stress can result in the formation of cracks in the infiltrated structures, as is visible in the complex geometry of Figure 4.2B given the variations in the hue of the As_2S_3 geometry. This issue might be solved either by carefully optimizing the peak temperature and/or the cooling rate during infiltration or in post-processing annealing and/or by using a glass mold with a CTE similar to that of the infiltrant such as, for example, a borosilicate (i.e. $3.3 \cdot 10^{-6}$ K^{-1}, from Schott). It is worth noting that in case of a change in mold substrate, the infiltrant properties (as glass transition temperature and viscosity) and the process parameters (as temperature and pressure) define the minimum feature size that can be infiltrated. Therefore, although the parameters can be largely tuned, the ultimate constraints are set by the properties of the materials chosen – within the equipment capability. More information on modeling the pressure-assisted infiltration of chalcogenide in straight cylindrical holes can be found in [210–212].

As a proof-of-concept, we demonstrate the potential of this infiltration process by testing the long channels in Figure 4.2C as mid-infrared waveguides. After fine-polishing the sample on both sides to expose both waveguide's input and output (see schematic in Figure 4.5A), a Gaussian beam emitted by a QCL laser operating in continuous wave at 8.3 μm with 100 mW of output power is injected into the waveguide by the use of a high numerical aperture IR lense. An IR camera and a beam profiler are used to collect, respectively, thermal images of the set-up (Figure 4.5B-C) and the collimated beam at the output of the mid-IR waveguide

(Figure 4.5D). The observation of a beam profile at the output of the waveguide suggests that the material quality and homogeneity in the waveguide is sufficient for guiding optical modes at this wavelength. This result is in line with the quasi-perfect material properties match between infiltrated and pristine chalcogenide, and previous results reported in literature [210–212]. Noteworthy, the refractive indexes difference between the chalcogenide and the SiO_2 at 8.3 μm yields a very high numerical aperture (NA) waveguide. Therefore, with the optical element used for the output beam collimation, the NA of the lens limit the collection efficiency. The expected, theoretical beam-size on the beam profiler (assuming a 50 μm beam-size at the waveguide output) is of 2.4 mm where 0.65 mm is measured. The discrepancy is attributed to the high confinement of the beam in the waveguide due on one hand to the large refractive indexes difference, and on the other hand, to the sensitivity of the profiler and the collection optics not been optimized for the waveguide dimensions.
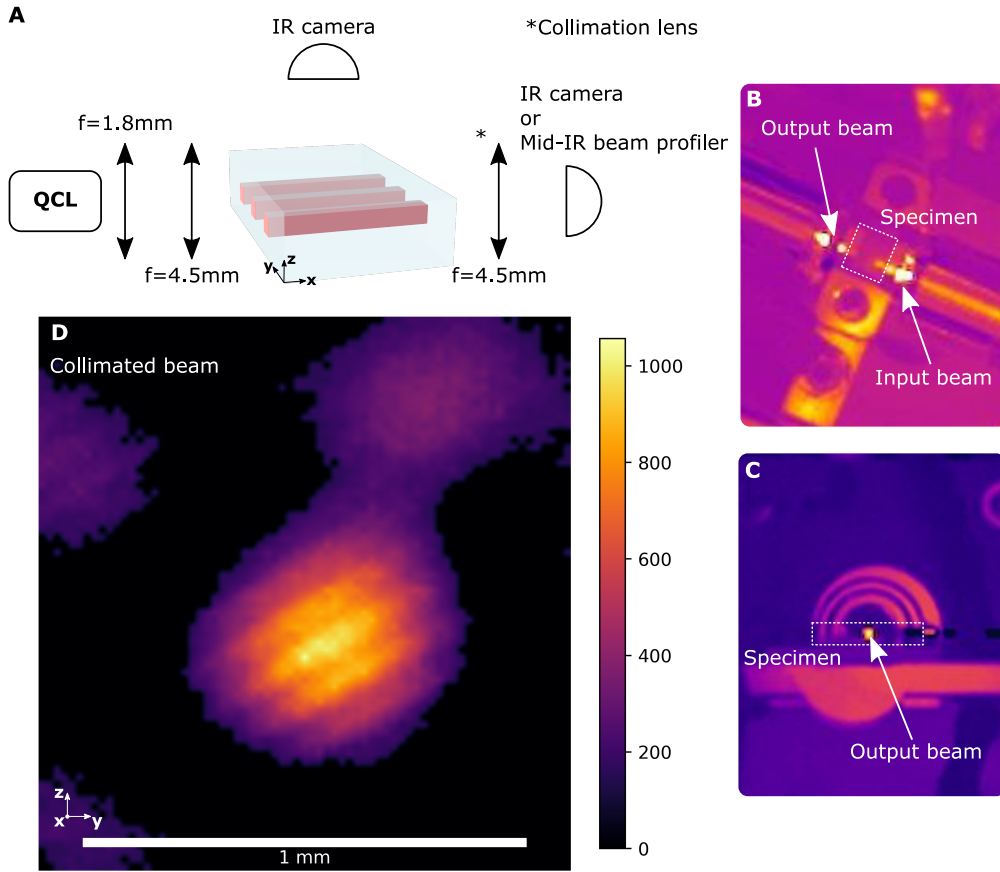
Figure 4.5: *Mid-IR waveguides testing. (A) Schematic of the setup used for testing the long channels of Figure 2C after fine-polishing them on both sides (3.5 mm long and about 50x50 μm^2 of cross-section). Thermal images - top view (B) and lateral view (C) - of the setup showing the specimen under test and the beam input and output. (D) Collimated beam intensity profile image of the multimode waveguide output.*

As shown by the samples presented above, the process enables the fabrication of three-dimensional chalcogenide structures in fused silica with micrometric precision. This in-

novation opens to innovative designs and further integration in the context of broadband photonics by offering a means to produce sub-mm components such as 3D waveguides, tapered or not, lenses, etc. all embedded in a robust silica substrate, that itself may contain additional features such as fluidic channels [19–24] or mechanical elements [101, 106]. To cite one example, such components are particularly interesting for mid-IR spectroscopy applications.

Regarding resolution, the smallest structure produced in this study is about 30 μm in size; however, it is possible to push such limits further by tuning parameters such as the pressure used during infiltration or the viscosity of the infiltrant, which for glass depends greatly on temperature. As an illustration, with the same infiltration process, we have demonstrated infiltration of poorly wetting metals such as silver and gold into glass molds having features around 2 μm in size [129].

Finally, in this demonstration we employed As_2S_3 as a chalcogenide glass for its high glass-forming capability; however, we have not explored how high the glass-forming ability needs to be for the resulting infiltrated glass to always be amorphous in structures such as those of this work. We thus believe that there is scope to transpose the same concept to other glass systems, both within and outside the chalcogenide family, provided the following limitations are respected: (i) the infiltrant and the substrate are not to react mutually at the infiltration temperature, and (ii) the infiltrant must have a glass transition temperature lower than that of the substrate, such that there be sufficient contrast between the (low) infiltrant viscosity and that of the (solid) mold to be infiltrated.

4.4   Summary and conclusion

In summary, we introduce a manufacturing technique by which one can fabricate microscale 3D chalcogenide microstructures embedded in fused silica. The process starts by carving a three-dimensional interconnected pattern into a fused silica mold using femtosecond laser exposure followed by chemical etching. The fabricated glass mold cavities are then filled with the second glass by pressure-assisted infiltration. As a proof of concept, As_2S_3 was employed; microstructural examination confirms the consistency of material properties before and after the infiltration.

The resulting silica-chalcogenide composites offer a high index contrast combination over a broad spectrum, with the silica mold acting as a mechanically and chemically resistant support and protection for the chalcogenide glass. This, together with the fine-scale 3D freeform capability of the presented manufacturing method, opens a wide range of broadband photonic applications for structures of the type presented here.

5 Conclusion

In this thesis work, we experimentally demonstrated novel micro-infiltration techniques enabled by the micro-fabrication of 3D glass molds by femtosecond laser-assisted chemical etching. The possibility to infiltrate freeform structures of metals and glass inside a single glass substrate paves the way for novel concepts of devices with unprecedented design freedom.

The development of these micro-infiltration techniques, included the investigation and optimization of the femtosecond laser-assisted chemical etching process.

There, we introduced a novel etchant with better etching performances than commonly used ones, and at the same time, more environmentally sustainable. Specifically, we unraveled a low laser-fluence etching regime that enables an order of magnitude increase in processing speed, while maintaining (or overcoming) maximum achievable aspect ratios reported so far. On a more fundamental point-of-view, we experimentally proved that in a low-fluence regime the selective etching is dominated by the presence of molecular defects, and not by the presence of *nanogratings.*

5.1 Main results

Let us summarize the main results obtained during this thesis work:

1. Evidence a low exposure-dose regime
The maximum performance of femtosecond laser-assisted chemical etching has been repeatedly reported to be around 15 J/mm^2 for the commonly known etching solutions, i.e. HF 2.5 $\%_{vol}$ and KOH 45 $\%_{wt}$. We have shown that a sodium hydroxide (NaOH) solution 5 $\%_{wt}$ can outperform hydrofluoric acid as well as potassium hydroxide solutions, both in terms of selectivity and etching rate. Interestingly, we found a low exposure-dose regime with a peak around 1.5 J/mm^2 that surpasses (for KOH) and equals (for HF) etching performances at 15 J/mm^2. This result is of practical importance as the reduction of laser deposited energy by a factor of ten, enables ten times faster inscription.

2. Evidence of a defect-driven selective etching process
Femtosecond laser inscription of fused silica induces material modifications that enhance the etching rate for certain chemical solutions. So far, the etching selectivity was observed in an exposure dose regime (above 10 J/mm^2), where micro-structural self-assembled modifications known as nanogratings (i.e. alternating porous and densified nanoplanes). Consequently, and due to the apparent correlation, the origin of induced etching selectivity has been associated, mainly with an increase in active surfaces and percolation due to the formation of porous interconnected nanoplanes. Here, we have demonstrated that for the low exposure dose regime, the etching selectivity is governed by the presence of molecular defects, and not by

the presence of nanogratings. This discovery shows that etching selectivity is induced by the combination of at least two factors: (i) molecular defects, and (ii) porosity and percolation. These two factors are interacting and influence the etching rate at any level of deposited energy, although one or the other may dominate for certain exposure regimes or etchants.

Quite unexpected and most remarkable is the fact that even for the low-exposure dose regime, with an etching-selectivity mainly driven by defects, the etching rate is strongly dependent on the laser polarization direction, and thus, the electrostatic field orientation. This observation hints at the presence of a self-organized network of defects, observed with a number of pulses per micron and energy significantly lower than what was considered up to now. This observation questions not only our true understanding of the femtosecond laser-driven etching but also the onset for the formation of laser-induced self-organized structures and their nature. *When does self-organization begin?*

3. Micro-infiltration of metals
We introduced a freeform manufacturing process combining femtosecond laser glass micro-machining and metal pressure infiltration. The process is suited for any metal which has a melting point below the softening point of silica and which does not react with the substrate. Among these metals, we successfully demonstrated the infiltration of silver, gold, copper, and their alloys of geometrically complex interconnected multiscale components up to a few millimeters in size and with micrometric resolution. Further, we engineered a process methodology to manufacture freeform glass-metal composites and to achieve multiple infiltrations in the same substrate, while demonstrating the process ability for large-scale production rates compared to existing 3D metal-printing technologies.

The resulting glass-metal combinations enable new device architectures for microtechnology applications in fields such as electro-optics, optomechanics, and micro-mechanics. In addition, by dissolving the mold, this process offers a pathway for fabricating complex metallic parts of high geometrical complexity and with micron-feature sizes that cannot be produced by classical lithographic approaches.

4. Micro-infiltration of IR glass
We explored the compatibility of the micro-infiltration process with infrared glass systems. In particular, we demonstrated the fabrication by pressure-assisted micro-infiltration of 3D freeform chalcogenide structures in a fused silica mold. The resulting silica-chalcogenide composites offer a high-index contrast combination over a broad spectrum, with the silica mold acting as a mechanically- and chemically-resistant substrate, protecting the otherwise fragile chalcogenide glass. This, together with the 3D resolution capability of the manufacturing method, opens new opportunities for broadband mid-IR photonic applications.

5.2   Discussion and outlook

When does self-organization begin?

The study on femtosecond laser-induced selective etching of glass presented in chapter 2 raises a fundamental question related to the origin of self-organization. In the debate between models involving plasma-laser interference versus models relying on 'nanoscale' field-effect enhancement, our observations suggest a more complex picture than previously thought. An interesting question is for instance to know if some levels of self-organization are already present after the first pule. Experimentally, this question can be answered for example, by single pulse exposure at low-pulse energy. The difficulty remains in the detection of these few defects and their distributions in the focal volume. A possible characterization may involve brief NaOH etching combined with SEM backscattered microscopy.

New materials for micro-infiltration

A key advantage of infiltration is the diversity of materials choices. However, such a characteristic is not trivially inherited when scaling down to the micron-scale. Here, we experimented micro-infiltration in fused silica, with some selected infiltrants: noble metals and their alloys and one composition of chalcogenide glass.

For the substrate, a better choice would be Al_2O_3 (sapphire) that is one of the most stable materials, both chemically and thermally. Unfortunately, at this stage, it remains difficult to pattern in 3D. Another alternative material substrate is borosilicate glass, for which femtosecond laser 3D glass micromachining has been demonstrated [25, 69, 240–243]. Although having a significant lower-softening point than fused silica, which limits the possible choice of materials to materials with a melting point below 500°C, it offers the advantage of having a CTE higher than silica, and therefore, closer to the CTEs of infiltrants. Thus, the effect of thermal stress can be substantially decreased.

For metal infiltrants, the interest is in expanding the choice towards alloys than pure metals, for example, for applications in micro-mechanics. The main challenges being (i) the chemical reactivity and (ii) the high melting temperature of certain alloying metals such as chromium, nickel, copper, manganese, tungsten, and others.

For glass infiltrants, the demonstration of chalcogenide micro-infiltration in fused silica opens to a multitude of other compounds, that can be synthesized *ad hoc* to have a large glass-forming ability, compatible with the infiltration process. In particular, the interest is in transposing the same manufacturing concept to other chalcogenide or tellurite compositions. The latter has interesting characteristics, such as ultra-high Kerr nonlinearity, broadband infrared transmission, and large rare-earth elements solubility.

Towards applications

In the context of applying these micro-infiltration processes to 3D-integrated micro-device architectures, we provide a few possible research directions.

Infiltrating highly conducting structure of noble metals can be used for designing freeform

electrodes, embedded in a glass. Acousto-optic effects for almost any 3D retardance patterns can be envisioned by taking advantage of the birefringent nature of fused silica coupled with actuating principles such as electrostatic force and electrostriction, combined with the already present thermal stress. Alternatively, by the use of thermal poling (i.e. electro-thermal treatment to break the centrosymmetry of glass and obtain a non zero value of $\chi^{(2)}$) one could design arbitrary second-order nonlinearity domains inside a glass for applications in electro-optics such as quasi-phase-matched (QPM) modulators or higher harmonics generation.

The infiltration of different glass systems inside a more mechanically and chemically stable glass substrate such as fused silica enables the 3D manufacturing and integration of notably weak and reactive compounds such as chalcogenides and tellurites. Despite their poor mechanical and chemical properties, those glass systems present an extremely broadband infrared spectrum and very large Kerr non-linearity ($\chi^{(3)}$). A multitude of micro-optical applications can be envisioned such as integrating 3D infrared waveguides, photonic lanterns, and lenses, but also - taking advantage of high rare earth element solubility - freeform shaped lasing cavities, or even devices for electro-optic phase modulation or supercontinuum generation.

5.3   Personal contributions

The work presented in this thesis was a collaborative effort and the result of teamwork. All started after the conception, chiefly by Prof. A. Mortensen and Y. Bellouard, of *micro-infiltration* as a combination of femtosecond laser micromachining of glass molds and pressure-assisted metals infiltration.

In this context, my objective was to explore the use of *micro-infiltration* for the integration of metals and glass 3D structures inside a glass substrate for applications within the broad photonics field. My principal roles were (i) to optimize femtosecond laser-assisted chemical etching as a process to prepare 3D glass molds, (ii) to investigate the *micro-infiltration* as a means of integrating metallic and infrared glass 3D structures into fused silica. While I was the main contributor to the study on femtosecond laser-assisted chemical etching (chapter 2), I collaborated closely with Luciano Borasi, in the laboratory of Andreas Mortensen, for the development of the *micro-infiltration* process both for metals (chapter 3) and glass (chapter 4). Luciano Borasi optimized the infiltration stage and performed the materials characterization of the metallic components. Finally, in the *micro-infiltration* of glass-in-glass (chapter 4), the experience of Gözden Torun in glass characterization was a key to the success of the project.

Bibliography

[1] K. M. Davis, K. Miura, N. Sugimoto, and K. Hirao. Writing waveguides in glass with a femtosecond laser. *Optics Letters*, 21(21):1729, Nov. 1996. doi:10.1364/OL.21.001729.

[2] Y. Kondo, J. Qiu, T. Mitsuyu, K. Hirao, and T. Yoko. Three-Dimensional Microdrilling of Glass by Multiphoton Process and Chemical Etching. *Japanese Journal of Applied Physics*, 38(Part 2, No. 10A):L1146–L1148, Oct. 1999. doi:10.1143/JJAP.38.L1146.

[3] A. Marcinkevičius, S. Juodkazis, M. Watanabe, M. Miwa, S. Matsuo, H. Misawa, and J. Nishii. Femtosecond laser-assisted three-dimensional microfabrication in silica. *Optics Letters*, 26(5):277, Mar. 2001. doi:10.1364/OL.26.000277.

[4] B. Lenssen and Y. Bellouard. Optically transparent glass micro-actuator fabricated by femtosecond laser exposure and chemical etching. *Applied Physics Letters*, 101(10): 103503, Sept. 2012. doi:10.1063/1.4750236.

[5] T. Yang and Y. Bellouard. Monolithic transparent 3D dielectrophoretic micro-actuator fabricated by femtosecond laser. *Journal of Micromechanics and Microengineering*, 25 (10):105009, Oct. 2015. doi:10.1088/0960-1317/25/10/105009.

[6] Y. Bellouard. Non-contact sub-nanometer optical repositioning using femtosecond lasers. *Optics Express*, 23(22):29258, Nov. 2015. doi:10.1364/OE.23.029258.

[7] Nazir and Bellouard. A Monolithic Gimbal Micro-Mirror Fabricated and Remotely Tuned with a Femtosecond Laser. *Micromachines*, 10(9):611, Sept. 2019. doi:10.3390/mi10090611.

[8] E. Casamenti, T. Yang, P. Vlugter, and Y. Bellouard. Vibrations monitoring based on optical sensing of glass suspended waveguides mechanical nonlinearities. *Optics Express*, 29(7):10853–10862, Mar. 2021. doi:10.1364/OE.414191.

[9] K. Minoshima, A. M. Kowalevicz, I. Hartl, E. P. Ippen, and J. G. Fujimoto. Photonic device fabrication in glass by use of nonlinear materials processing with a femtosecond laser oscillator. *Optics Letters*, 26(19):1516, Oct. 2001. doi:10.1364/OL.26.001516.

[10] A. M. Kowalevicz, V. Sharma, E. P. Ippen, J. G. Fujimoto, and K. Minoshima. Three-dimensional photonic devices fabricated in glass by use of a femtosecond laser oscillator. *Optics Letters*, 30(9):1060, May 2005. doi:10.1364/OL.30.001060.

[11] G. D. Marshall, P. Dekker, M. Ams, J. A. Piper, and M. J. Withford. Directly written monolithic waveguide laser incorporating a distributed feedback waveguide-Bragg grating. *Optics Letters*, 33(9):956, May 2008. doi:10.1364/OL.33.000956.

[12] K. K. Lee, A. Mariampillai, M. Haque, B. A. Standish, V. X. Yang, and P. R. Herman. Temperature-compensated fiber-optic 3D shape sensor based on femtosecond laser direct-written Bragg grating waveguides. *Optics Express*, 21(20):24076, Oct. 2013. doi:10.1364/OE.21.024076.

[13] G. Bharathan, R. I. Woodward, M. Ams, D. D. Hudson, S. D. Jackson, and A. Fuerbach. Direct inscription of Bragg gratings into coated fluoride fibers for widely tunable and robust mid-infrared lasers. *Optics Express*, 25(24):30013, Nov. 2017. doi:10.1364/OE.25.030013.

[14] R. G. Krämer, F. Möller, C. Matzdorf, T. A. Goebel, M. Strecker, M. Heck, D. Richter, M. Plötner, T. Schreiber, A. Tünnermann, and S. Nolte. Extremely robust femtosecond written fiber Bragg gratings for an ytterbium-doped fiber oscillator with 5 kW output power. *Optics Letters*, 45(6):1447, Mar. 2020. doi:10.1364/OL.389427.

[15] M. Beresna, M. Gecevičius, P. G. Kazansky, and T. Gertus. Radially polarized optical vortex converter created by femtosecond laser nanostructuring of glass. *Applied Physics Letters*, 98(20):201101, May 2011. doi:10.1063/1.3590716.

[16] B. McMillen, C. Athanasiou, and Y. Bellouard. Femtosecond laser direct-write waveplates based on stress-induced birefringence. *Optics Express*, 24(24):27239, Nov. 2016. doi:10.1364/OE.24.027239.

[17] J. Liu, Z. Zhang, S. Chang, C. Flueraru, and C. P. Grover. Directly writing of 1-to-N optical waveguide power splitters in fused silica glass using a femtosecond laser. *Optics Communications*, 253(4-6):315–319, Sept. 2005. doi:10.1016/j.optcom.2005.04.082.

[18] R. R. Thomson, T. A. Birks, S. G. Leon-Saval, A. K. Kar, and J. Bland-Hawthorn. Ultrafast laser inscription of an integrated photonic lantern. *Optics Express*, 19(6):5698, Mar. 2011. doi:10.1364/OE.19.005698.

[19] Y. Bellouard, A. Said, M. Dugan, and P. Bado. Fabrication of high-aspect ratio, microfluidic channels and tunnels using femtosecond laser pulses and chemical etching. *Optics Express*, 12(10):2120, 2004. doi:10.1364/OPEX.12.002120.

[20] Y. Cheng, K. Sugioka, and K. Midorikawa. Microfluidic laser embedded in glass by three-dimensional femtosecond laser microprocessing. *Optics Letters*, 29(17):2007, Sept. 2004. doi:10.1364/OL.29.002007.

[21] C. Hnatovsky, R. S. Taylor, E. Simova, V. R. Bhardwaj, D. M. Rayner, and P. B. Corkum. Polarization-selective etching in femtosecond laser-assisted microfluidic channel fabrication in fused silica. *Optics Letters*, 30(14):1867, July 2005. doi:10.1364/OL.30.001867.

[22] T. N. Kim, K. Campbell, A. Groisman, D. Kleinfeld, and C. B. Schaffer. Femtosecond laser-drilled capillary integrated into a microfluidic device. *Applied Physics Letters*, 86 (20):201106, May 2005. doi:10.1063/1.1926423.

[23] K. Sugioka, Y. Cheng, and K. Midorikawa. Three-dimensional micromachining of glass using femtosecond laser for lab-on-a-chip device manufacture. *Applied Physics A*, 81(1): 1–10, June 2005. doi:10.1007/s00339-005-3225-1.

[24] V. Maselli, R. Osellame, G. Cerullo, R. Ramponi, P. Laporta, L. Magagnin, and P. L. Cavallotti. Fabrication of long microchannels with circular cross section using astigmatically shaped femtosecond laser pulses and chemical etching. *Applied Physics Letters*, 88(19): 191107, May 2006. doi:10.1063/1.2203335.

[25] C. Hnatovsky, R. Taylor, E. Simova, P. Rajeev, D. Rayner, V. Bhardwaj, and P. Corkum. Fabrication of microchannels in glass using focused femtosecond laser radiation and selective chemical etching. *Applied Physics A*, 84(1-2):47–61, May 2006. doi:10.1007/s00339-006-3590-4.

[26] R. W. Applegate Jr., J. Squier, T. Vestad, J. Oakey, D. W. M. Marr, P. Bado, M. A. Dugan, and A. A. Said. Microfluidic sorting system based on optical waveguide integration and diode laser bar trapping. *Lab on a Chip*, 6(3):422, 2006. doi:10.1039/b512576f.

[27] M. Kim, D. J. Hwang, H. Jeon, K. Hiromatsu, and C. P. Grigoropoulos. Single cell detection using a glass-based optofluidic device fabricated by femtosecond laser pulses. *Lab Chip*, 9(2):311–318, 2009. doi:10.1039/B808366E.

[28] D. J. Hwang, M. Kim, K. Hiromatsu, H. Jeon, and C. P. Grigoropoulos. Three-dimensional opto-fluidic devices fabricated by ultrashort laser pulses for high-throughput single cell detection and processing. *Applied Physics A*, 96(2):385–390, Aug. 2009. doi:10.1007/s00339-009-5210-6.

[29] R. Martinez Vazquez, R. Osellame, M. Cretich, M. Chiari, C. Dongre, H. J. W. M. Hoekstra, M. Pollnau, H. van den Vlekkert, R. Ramponi, and G. Cerullo. Optical sensing in microfluidic lab-on-a-chip by femtosecond-laser-written waveguides. *Analytical and Bioanalytical Chemistry*, 393(4):1209–1216, Feb. 2009. doi:10.1007/s00216-008-2399-8.

[30] N. Bellini, K. C. Vishnubhatla, F. Bragheri, L. Ferrara, P. Minzioni, R. Ramponi, I. Cristiani, and R. Osellame. Femtosecond laser fabricated monolithic chip for optical trapping and stretching of single cells. *Optics Express*, 18(5):4679, Mar. 2010. doi:10.1364/OE.18.004679.

[31] F. Bragheri, L. Ferrara, N. Bellini, K. C. Vishnubhatla, P. Minzioni, R. Ramponi, R. Osellame, and I. Cristiani. Optofluidic chip for single cell trapping and stretching fabricated by a femtosecond laser. *Journal of Biophotonics*, 3(4):234–243, Apr. 2010. doi:10.1002/jbio.201000011.

Bibliography

[32] R. Osellame, H. Hoekstra, G. Cerullo, and M. Pollnau. Femtosecond laser microstructuring: an enabling tool for optofluidic lab-on-chips. *Laser & Photonics Reviews*, 5(3): 442–463, May 2011. doi:10.1002/lpor.201000031.

[33] A. Schaap, Y. Bellouard, and T. Rohrlack. Optofluidic lab-on-a-chip for rapid algae population screening. *Biomedical Optics Express*, 2(3):658, Mar. 2011. doi:10.1364/BOE.2.000658.

[34] J. Qiu, K. Miura, H. Inouye, J. Nishii, and K. Hirao. Three-dimensional optical storage inside a silica glass by using a focused femtosecond pulsed laser. *Nuclear Instruments and Methods in Physics Research Section B: Beam Interactions with Materials and Atoms*, 141(1-4):699–703, May 1998. doi:10.1016/S0168-583X(98)00172-4.

[35] J. Zhang, M. Gecevičius, M. Beresna, and P. G. Kazansky. Seemingly Unlimited Lifetime Data Storage in Nanostructured Glass. *Physical Review Letters*, 112(3):033901, Jan. 2014. doi:10.1103/PhysRevLett.112.033901.

[36] H. Wang, Y. Lei, L. Wang, M. Sakakura, Y. Yu, G. Shayeganrad, and P. G. Kazansky. 100-Layer Error-Free 5D Optical Data Storage by Ultrafast Laser Nanostructuring in Glass. *Laser & Photonics Reviews*, page 2100563, Jan. 2022. doi:10.1002/lpor.202100563.

[37] D. Strickland and G. Mourou. Compression of amplified chirped optical pulses. *Optics Communications*, 56(3):219–221, Dec. 1985. doi:10.1016/0030-4018(85)90120-8.

[38] C. B. Schaffer, A. Brodeur, J. F. García, and E. Mazur. Micromachining bulk glass by use of femtosecond laser pulses with nanojoule energy. *Optics Letters*, 26(2):93, Jan. 2001. doi:10.1364/OL.26.000093.

[39] E. N. Glezer and E. Mazur. Ultrafast-laser driven micro-explosions in transparent materials. *Applied Physics Letters*, 71(7):882–884, Aug. 1997. doi:10.1063/1.119677.

[40] S. Juodkazis, K. Nishimura, S. Tanaka, H. Misawa, E. G. Gamaly, B. Luther-Davies, L. Hallo, P. Nicolai, and V. T. Tikhonchuk. Laser-Induced Microexplosion Confined in the Bulk of a Sapphire Crystal: Evidence of Multimegabar Pressures. *Physical Review Letters*, 96(16):166101, Apr. 2006. doi:10.1103/PhysRevLett.96.166101.

[41] Y. Bellouard and M.-O. Hongler. Femtosecond-laser generation of self-organized bubble patterns in fused silica. *Optics Express*, 19(7):6807, Mar. 2011. doi:10.1364/OE.19.006807.

[42] Y. Kaganovskii, I. Antonov, D. Ianetz, M. Rosenbluh, J. Ihlemann, S. Mueller, G. Marowsky, and A. A. Lipovskii. Optical recording in silver-doped glasses by a femtosecond laser. *Applied Physics Letters*, 83(3):554–556, July 2003. doi:10.1063/1.1593828.

[43] R. Ricca, V. Boureau, and Y. Bellouard. Ultrafast laser interaction with transparent multi-layer SiO_2/Si_3N_4 films. *Journal of Applied Physics*, 130(24):243105, Dec. 2021. doi:10.1063/5.0065726.

[44] Y. Kondo, T. Suzuki, H. Inouye, K. Miura, T. Mitsuyu, and K. Hirao. Three-Dimensional Microscopic Crystallization in Photosensitive Glass by Femtosecond Laser Pulses at Nonresonant Wavelength. *Japanese Journal of Applied Physics*, 37(Part 2, No. 1A/B): L94–L96, Jan. 1998. doi:10.1143/JJAP.37.L94.

[45] K. Miura, J. Qiu, T. Mitsuyu, and K. Hirao. Space-selective growth of frequency-conversion crystals in glasses with ultrashort infrared laser pulses. *Optics Letters*, 25(6): 408, Mar. 2000. doi:10.1364/OL.25.000408.

[46] K. Hirao and K. Miura. Writing waveguides and gratings in silica and related materials by a femtosecond laser. *Journal of Non-Crystalline Solids*, 239(1-3):91–95, Oct. 1998. doi:10.1016/S0022-3093(98)00755-8.

[47] M. Will, S. Nolte, B. N. Chichkov, and A. Tünnermann. Optical properties of waveguides fabricated in fused silica by femtosecond laser pulses. *Applied Optics*, 41(21):4360, July 2002. doi:10.1364/AO.41.004360.

[48] J. Chan, T. Huser, S. Risbud, and D. Krol. Modification of the fused silica glass network associated with waveguide fabrication using femtosecond laser pulses. *Applied Physics A: Materials Science & Processing*, 76(3):367–372, Mar. 2003. doi:10.1007/s00339-002-1822-9.

[49] V. R. Bhardwaj, P. B. Corkum, D. M. Rayner, C. Hnatovsky, E. Simova, and R. S. Taylor. Stress in femtosecond-laser-written waveguides in fused silica. *Optics Letters*, 29(12): 1312, June 2004. doi:10.1364/OL.29.001312.

[50] S. M. Eaton, M. L. Ng, R. Osellame, and P. R. Herman. High refractive index contrast in fused silica waveguides by tightly focused, high-repetition rate femtosecond laser. *Journal of Non-Crystalline Solids*, 357(11-13):2387–2391, June 2011. doi:10.1016/j.jnoncrysol.2010.11.082.

[51] C. Florea and K. Winick. Fabrication and characterization of photonic devices directly written in glass using femtosecond laser pulses. *Journal of Lightwave Technology*, 21(1): 246–253, Jan. 2003. doi:10.1109/JLT.2003.808678.

[52] R. Osellame, N. Chiodo, V. Maselli, A. Yin, M. Zavelani-Rossi, G. Cerullo, P. Laporta, L. Aiello, S. De Nicola, P. Ferraro, A. Finizio, and G. Pierattini. Optical properties of waveguides written by a 26 MHz stretched cavity Ti:sapphire femtosecond oscillator. *Optics Express*, 13(2):612, 2005. doi:10.1364/OPEX.13.000612.

[53] L. Gui, B. Xu, and T. Chong. Microstructure in Lithium Niobate by Use of Focused Femtosecond Laser Pulses. *IEEE Photonics Technology Letters*, 16(5):1337–1339, May 2004. doi:10.1109/LPT.2004.826112.

[54] R. R. Thomson, S. Campbell, I. J. Blewett, A. K. Kar, and D. T. Reid. Optical waveguide fabrication in z-cut lithium niobate (LiNbO3) using femtosecond pulses in

the low repetition rate regime. *Applied Physics Letters*, 88(11):111109, Mar. 2006. doi:10.1063/1.2186389.

[55] J. Burghoff, C. Grebing, S. Nolte, and A. Tünnermann. Efficient frequency doubling in femtosecond laser-written waveguides in lithium niobate. *Applied Physics Letters*, 89(8): 081108, Aug. 2006. doi:10.1063/1.2338532.

[56] A. H. Nejadmalayeri and P. R. Herman. Ultrafast laser waveguide writing: lithium niobate and the role of circular polarization and picosecond pulse width. *Optics Letters*, 31(20): 2987, Oct. 2006. doi:10.1364/OL.31.002987.

[57] Y. L. Lee, N. E. Yu, C. Jung, B.-A. Yu, I.-B. Sohn, S.-C. Choi, Y.-C. Noh, D.-K. Ko, W.-S. Yang, H.-M. Lee, W.-K. Kim, and H.-Y. Lee. Second-harmonic generation in periodically poled lithium niobate waveguides fabricated by femtosecond laser pulses. *Applied Physics Letters*, 89(17):171103, Oct. 2006. doi:10.1063/1.2364832.

[58] R. Osellame, M. Lobino, N. Chiodo, M. Marangoni, G. Cerullo, R. Ramponi, H. T. Bookey, R. R. Thomson, N. D. Psaila, and A. K. Kar. Femtosecond laser writing of waveguides in periodically poled lithium niobate preserving the nonlinear coefficient. *Applied Physics Letters*, 90(24):241107, June 2007. doi:10.1063/1.2748328.

[59] H. T. Bookey, R. R. Thomson, N. D. Psaila, A. K. Kar, N. Chiodo, R. Osellame, and G. Cerullo. Femtosecond Laser Inscription of Low Insertion Loss Waveguides in Z-Cut Lithium Niobate. *IEEE Photonics Technology Letters*, 19(12):892–894, June 2007. doi:10.1109/LPT.2007.897534.

[60] A. Courvoisier, M. J. Booth, and P. S. Salter. Inscription of 3D waveguides in diamond using an ultrafast laser. *Applied Physics Letters*, 109(3):031109, July 2016. doi:10.1063/1.4959267.

[61] B. Sotillo, V. Bharadwaj, J. P. Hadden, M. Sakakura, A. Chiappini, T. T. Fernandez, S. Longhi, O. Jedrkiewicz, Y. Shimotsuma, L. Criante, R. Osellame, G. Galzerano, M. Ferrari, K. Miura, R. Ramponi, P. E. Barclay, and S. M. Eaton. Diamond photonics platform enabled by femtosecond laser writing. *Scientific Reports*, 6(1):35566, Dec. 2016. doi:10.1038/srep35566.

[62] V. Bharadwaj, A. Courvoisier, T. T. Fernandez, R. Ramponi, G. Galzerano, J. Nunn, M. J. Booth, R. Osellame, S. M. Eaton, and P. S. Salter. Femtosecond laser inscription of Bragg grating waveguides in bulk diamond. *Optics Letters*, 42(17):3451, Sept. 2017. doi:10.1364/OL.42.003451.

[63] A. H. Nejadmalayeri, P. R. Herman, J. Burghoff, M. Will, S. Nolte, and A. Tünnermann. Inscription of optical waveguides in crystalline silicon by mid-infrared femtosecond laser pulses. *Optics Letters*, 30(9):964, May 2005. doi:10.1364/OL.30.000964.

[64] Y. Shimotsuma, P. G. Kazansky, J. Qiu, and K. Hirao. Self-Organized Nanogratings in Glass Irradiated by Ultrashort Light Pulses. *Physical Review Letters*, 91(24):247405, Dec. 2003. doi:10.1103/PhysRevLett.91.247405.

[65] S. Richter, C. Miese, S. Döring, F. Zimmermann, M. J. Withford, A. Tünnermann, and S. Nolte. Laser induced nanogratings beyond fused silica - periodic nanostructures in borosilicate glasses and ULE™. *Optical Materials Express*, 3(8):1161, Aug. 2013. doi:10.1364/OME.3.001161.

[66] F. Zimmermann, A. Plech, S. Richter, A. Tünnermann, and S. Nolte. Ultrashort laser pulse induced nanogratings in borosilicate glass. *Applied Physics Letters*, 104(21):211107, May 2014. doi:10.1063/1.4880658.

[67] Y. Liao, W. Pan, Y. Cui, L. Qiao, Y. Bellouard, K. Sugioka, and Y. Cheng. Formation of in-volume nanogratings with sub-100-nm periods in glass by femtosecond laser irradiation. *Optics Letters*, 40(15):3623, Aug. 2015. doi:10.1364/OL.40.003623.

[68] M. Lancry, F. Zimmerman, R. Desmarchelier, J. Tian, F. Brisset, S. Nolte, and B. Poumellec. Nanogratings formation in multicomponent silicate glasses. *Applied Physics B*, 122(3): 66, Mar. 2016. doi:10.1007/s00340-016-6337-8.

[69] A. Crespi, R. Osellame, and F. Bragheri. Femtosecond-laser-written optofluidics in alumino-borosilicate glass. *Optical Materials: X*, 4:100042, Dec. 2019. doi:10.1016/j.omx.2019.100042.

[70] G. Torun, T. Kishi, and Y. Bellouard. Direct-write laser-induced self-organization and metallization beyond the focal volume in tellurite glass. *Physical Review Materials*, 5(5): 055201, May 2021. doi:10.1103/PhysRevMaterials.5.055201.

[71] T. Q. Jia, H. X. Chen, M. Huang, F. L. Zhao, J. R. Qiu, R. X. Li, Z. Z. Xu, X. K. He, J. Zhang, and H. Kuroda. Formation of nanogratings on the surface of a ZnSe crystal irradiated by femtosecond laser pulses. *Physical Review B*, 72(12):125429, Sept. 2005. doi:10.1103/PhysRevB.72.125429.

[72] Q. Zhang, H. Lin, B. Jia, L. Xu, and M. Gu. Nanogratings and nanoholes fabricated by direct femtosecond laser writing in chalcogenide glasses. *Optics Express*, 18(7):6885, Mar. 2010. doi:10.1364/OE.18.006885.

[73] S. H. Messaddeq, R. Vallée, P. Soucy, M. Bernier, M. El-Amraoui, and Y. Messaddeq. Self-organized periodic structures on Ge-S based chalcogenide glass induced by femtosecond laser irradiation. *Optics Express*, 20(28):29882, Dec. 2012. doi:10.1364/OE.20.029882.

[74] M. Huang, F. Zhao, Y. Cheng, N. Xu, and Z. Xu. Mechanisms of ultrafast laser-induced deep-subwavelength gratings on graphite and diamond. *Physical Review B*, 79(12): 125436, Mar. 2009. doi:10.1103/PhysRevB.79.125436.

Bibliography

[75] A. Abdelmalek, B. Sotillo, Z. Bedrane, V. Bharadwaj, S. Pietralunga, R. Ramponi, E.-H. Amara, and S. M. Eaton. Origin of femtosecond laser induced periodic nanostructure on diamond. *AIP Advances*, 7(10):105105, Oct. 2017. doi:10.1063/1.5001942.

[76] D. Kim, W. Jang, T. Kim, A. Moon, K.-S. Lim, M. Lee, I.-B. Sohn, and S. Jeong. Nanostructure and microripple formation on the surface of sapphire with femtosecond laser pulses. *Journal of Applied Physics*, 111(9):093518, May 2012. doi:10.1063/1.4707951.

[77] C. E. Athanasiou. Non-contact femtosecond laser-based methods for investigating glass mechanics at small scales. 2018. doi:10.5075/EPFL-THESIS-8323. Publisher: Lausanne, EPFL.

[78] S. I. Nazir, C. E. Athanasiou, and Y. Bellouard. On the behavior of uniaxial static stress loaded micro-scale fused silica beams at room temperature. *Journal of Non-Crystalline Solids: X*, 14:100083, June 2022. doi:10.1016/j.nocx.2022.100083.

[79] R. R. Gattass and E. Mazur. Femtosecond laser micromachining in transparent materials. *Nature Photonics*, 2(4):219–225, Apr. 2008. doi:10.1038/nphoton.2008.47.

[80] L. Skuja. Optically active oxygen-deficiency-related centers in amorphous silicon dioxide. *Journal of Non-Crystalline Solids*, 239(1-3):16–48, Oct. 1998. doi:10.1016/S0022-3093(98)00720-0.

[81] H.-B. Sun, S. Juodkazis, M. Watanabe, S. Matsuo, H. Misawa, and J. Nishii. Generation and Recombination of Defects in Vitreous Silica Induced by Irradiation with a Near-Infrared Femtosecond Laser. *The Journal of Physical Chemistry B*, 104(15):3450–3455, Apr. 2000. doi:10.1021/jp992828h.

[82] S. Richter, M. Heinrich, S. Döring, A. Tünnermann, and S. Nolte. Formation of femtosecond laser-induced nanogratings at high repetition rates. *Applied Physics A*, 104(2): 503–507, Aug. 2011. doi:10.1007/s00339-011-6489-7.

[83] L. Sudrie, M. Franco, B. Prade, and A. Mysyrowicz. Study of damage in fused silica induced by ultra-short IR laser pulses. *Optics Communications*, 191(3-6):333–339, May 2001. doi:10.1016/S0030-4018(01)01152-X.

[84] E. Bricchi, B. G. Klappauf, and P. G. Kazansky. Form birefringence and negative index change created by femtosecond direct writing in transparent materials. *Optics Letters*, 29(1):119, Jan. 2004. doi:10.1364/OL.29.000119.

[85] C. Hnatovsky, R. S. Taylor, P. P. Rajeev, E. Simova, V. R. Bhardwaj, D. M. Rayner, and P. B. Corkum. Pulse duration dependence of femtosecond-laser-fabricated nanogratings in fused silica. *Applied Physics Letters*, 87(1):014104, July 2005. doi:10.1063/1.1991991.

[86] R. Taylor, C. Hnatovsky, and E. Simova. Applications of femtosecond laser induced self-organized planar nanocracks inside fused silica glass. *Laser & Photonics Review*, 2 (1-2):26–46, Apr. 2008. doi:10.1002/lpor.200710031.

94

[87] Y. Sikorski, A. Said, P. Bado, R. Maynard, C. Florea, and K. Winick. Optical waveguide amplifier in nd-doped glass written with near-ir femtosecond laser pulses. *Electronics letters*, 36(3):226–227, 2000.

[88] P. Bado, A. Said, M. Dugan, T. Sosnowski, and S. Wright. Dramatic improvements in waveguide manufacturing with femtosecond lasers. *NFOEC, Dallas*, 2002.

[89] R. Osellame, S. Taccheo, M. Marangoni, R. Ramponi, P. Laporta, D. Polli, S. De Silvestri, and G. Cerullo. Femtosecond writing of active optical waveguides with astigmatically shaped beams. *Journal of the Optical Society of America B*, 20(7):1559, July 2003. doi:10.1364/JOSAB.20.001559.

[90] R. Osellame, N. Chiodo, G. Della Valle, S. Taccheo, R. Ramponi, G. Cerullo, A. Killi, U. Morgner, M. Lederer, and D. Kopf. Optical waveguide writing with a diode-pumped femtosecond oscillator. *Optics Letters*, 29(16):1900, Aug. 2004. doi:10.1364/OL.29.001900.

[91] C. Florea, K. Winick, Y. Sikorski, A. Said, and P. Bado. Optical waveguide amplifier in Nd-doped glass written with near-IR femtosecond laser pulses. In *Conference on Lasers and Electro-Optics (CLEO 2000). Technical Digest. Postconference Edition. TOPS Vol.39 (IEEE Cat. No.00CH37088)*, pages 128–129, San Francisco, CA, USA, 2000. IEEE. ISBN 978-1-55752-634-2. doi:10.1109/CLEO.2000.906817.

[92] V. R. Bhardwaj, E. Simova, P. P. Rajeev, C. Hnatovsky, R. S. Taylor, D. M. Rayner, and P. B. Corkum. Optically Produced Arrays of Planar Nanostructures inside Fused Silica. *Physical Review Letters*, 96(5):057404, Feb. 2006. doi:10.1103/PhysRevLett.96.057404.

[93] S. Richter, M. Heinrich, S. Döring, A. Tünnermann, S. Nolte, and U. Peschel. Nanogratings in fused silica: Formation, control, and applications. *Journal of Laser Applications*, 24(4):042008, Sept. 2012. doi:10.2351/1.4718561.

[94] C. Mauclair, M. Zamfirescu, J. P. Colombier, G. Cheng, K. Mishchik, E. Audouard, and R. Stoian. Control of ultrafast laser-induced bulk nanogratings in fused silica via pulse time envelopes. *Optics Express*, 20(12):12997, June 2012. doi:10.1364/OE.20.012997.

[95] A. Rudenko, J.-P. Colombier, and T. E. Itina. From random inhomogeneities to periodic nanostructures induced in bulk silica by ultrashort laser. *Physical Review B*, 93(7):075427, Feb. 2016. doi:10.1103/PhysRevB.93.075427.

[96] M. Gecevičius, M. Beresna, J. Zhang, W. Yang, H. Takebe, and P. G. Kazansky. Extraordinary anisotropy of ultrafast laser writing in glass. *Optics Express*, 21(4):3959, Feb. 2013. doi:10.1364/OE.21.003959.

[97] S. Kiyama, S. Matsuo, S. Hashimoto, and Y. Morihira. Examination of Etching Agent and Etching Mechanism on Femotosecond Laser Microfabrication of Channels Inside Vitreous Silica Substrates. *The Journal of Physical Chemistry C*, 113(27):11560–11566, July 2009. doi:10.1021/jp900915r.

[98] E. Casamenti, S. Pollonghini, and Y. Bellouard. Few pulses femtosecond laser exposure for high efficiency 3D glass micromachining. *Optics Express*, 29(22):35054, Oct. 2021. doi:10.1364/OE.435163.

[99] A. Champion and Y. Bellouard. Direct volume variation measurements in fused silica specimens exposed to femtosecond laser. *Optical Materials Express*, 2(6):789, June 2012. doi:10.1364/OME.2.000789.

[100] A. Champion, M. Beresna, P. Kazansky, and Y. Bellouard. Stress distribution around femtosecond laser affected zones: effect of nanogratings orientation. *Optics Express*, 21 (21):24942, Oct. 2013. doi:10.1364/OE.21.024942.

[101] V. Tielen and Y. Bellouard. Three-Dimensional Glass Monolithic Micro-Flexure Fabricated by Femtosecond Laser Exposure and Chemical Etching. *Micromachines*, 5(3): 697–710, Sept. 2014. doi:10.3390/mi5030697.

[102] C.-E. Athanasiou and Y. Bellouard. A Monolithic Micro-Tensile Tester for Investigating Silicon Dioxide Polymorph Micromechanics, Fabricated and Operated Using a Femtosecond Laser. *Micromachines*, 6(9):1365–1386, Sept. 2015. doi:10.3390/mi6091365.

[103] A. Crespi, Y. Gu, B. Ngamsom, H. J. W. M. Hoekstra, C. Dongre, M. Pollnau, R. Ramponi, H. H. van den Vlekkert, P. Watts, G. Cerullo, and R. Osellame. Three-dimensional Mach-Zehnder interferometer in a microfluidic chip for spatially-resolved label-free detection. *Lab on a Chip*, 10(9):1167, 2010. doi:10.1039/b920062b.

[104] M. Haque, K. K. C. Lee, S. Ho, L. A. Fernandes, and P. R. Herman. Chemical-assisted femtosecond laser writing of lab-in-fibers. *Lab Chip*, 14(19):3817–3829, 2014. doi:10.1039/C4LC00648H.

[105] M. Zanaty, T. Fussinger, A. Rogg, A. Lovera, D. Lambelet, I. Vardi, T. J. Wolfensberger, C. Baur, and S. Henein. Programmable Multistable Mechanisms for Safe Surgical Puncturing. *Journal of Medical Devices*, 13(2):021002, June 2019. doi:10.1115/1.4043016.

[106] Y. Bellouard, A. A. Said, and P. Bado. Integrating optics and micro-mechanics in a single substrate: a step toward monolithic integration in fused silica. *Optics Express*, 13(17): 6635, Aug. 2005. doi:10.1364/OPEX.13.006635.

[107] Y. Bellouard, A. Said, M. Dugan, and P. Bado. Monolithic Three-Dimensional Integration of Micro-Fluidic Channels and Optical Waveguides in Fused Silica. *MRS Proceedings*, 782:A3.2, 2003. doi:10.1557/PROC-782-A3.2.

[108] R. Osellame, V. Maselli, R. M. Vazquez, R. Ramponi, and G. Cerullo. Integration of optical waveguides and microfluidic channels both fabricated by femtosecond laser irradiation. *Applied Physics Letters*, 90(23):231118, June 2007. doi:10.1063/1.2747194.

[109] Y. Bellouard, V. K. Pahilwani, T. Rohrlack, A. A. Said, M. Dugan, and P. Bado. Towards a femtosecond laser micromachined optofluidic device for distinguishing algae species. page 720312, San Jose, CA, Feb. 2009. doi:10.1117/12.813671.

[110] M. Thoury, B. Mille, T. Séverin-Fabiani, L. Robbiola, M. Réfrégiers, J.-F. Jarrige, and L. Bertrand. High spatial dynamics-photoluminescence imaging reveals the metallurgy of the earliest lost-wax cast object. *Nature Communications*, 7(1):13356, Dec. 2016. doi:10.1038/ncomms13356.

[111] J. Maran and P. Stockhammer, editors. *Appropriating innovations: entangled knowledge in Eurasia, 5000-1500 BCE*. Oxbow Books, Oxford Haverton, PA, 2017. ISBN 978-1-78570-724-7.

[112] M. Sahoo and S. Sahu. *Principles of metal casting*. McGraw-Hill Education, New York, third edition edition, 2014. ISBN 978-0-07-178975-2.

[113] E. P. DeGarmo, editor. *Materials and processes in manufacturing*. Wiley, Hoboken, N.J, 9th ed., update ed edition, 2003. ISBN 978-0-471-65653-1 978-0-471-65670-8.

[114] L. A. 04/14/2022 1:50:08 PM. https://wedmg.com/wp-content/uploads/sites/617/2021/12/32. -Investment-Castings-Procedure-and-Key-Components.png.

[115] L. A. 04/14/2022 1:56:48 PM. https://www.custompartnet.com/wu/images/sand-casting/sand-casting-mold.png.

[116] L. A. 04/14/2022 1:57:50 PM. https://www.engineeringclicks.com/wp-content/uploads/2016/06/Pressure-Die-Casting-PDC.jpg.

[117] T. V. R. Rao. *Metal casting: principles and practice*. New Age International Publishers, New Delhi, 1996. ISBN 978-81-224-0843-0. OCLC: 756010018.

[118] N. Eustathopoulos, M. G. Nicholas, and B. Drevet. *Wettability at high temperatures*. Number v. 3 in Pergamon materials series. Pergamon, Amsterdam ; New York, 1st ed edition, 1999. ISBN 978-0-08-042146-9.

[119] G. Baumeister, K. Mueller, R. Ruprecht, and J. Hausselt. Production of metallic high aspect ratio microstructures by microcasting. *Microsystem Technologies*, 8(2-3):105–108, May 2002. doi:10.1007/s00542-001-0132-z.

[120] G. Baumeister, J. Hausselt, and R. Ruprecht. Microcasting of parts made of metal alloys. *Microsystem Technologies*, 10(3):261–264, Mar. 2004. doi:10.1007/s00542-003-0363-2.

[121] A. Siegel, D. Bruzewicz, D. Weibel, and G. Whitesides. Microsolidics: Fabrication of Three-Dimensional Metallic Microstructures in Poly(dimethylsiloxane). *Advanced Materials*, 19(5):727–733, Mar. 2007. doi:10.1002/adma.200601787.

[122] K. Liu, Q. Yang, Y. Zhao, F. Chen, C. Shan, S. He, X. Fan, L. li, X. Meng, G. Du, and H. Bian. Three-dimensional metallic microcomponents achieved in fused silica by a femtosecond-laser-based microsolidifying process. *Microelectronic Engineering*, 113: 93–97, Jan. 2014. doi:10.1016/j.mee.2013.07.017.

[123] J. Xu, D. Wu, Y. Hanada, C. Chen, S. Wu, Y. Cheng, K. Sugioka, and K. Midorikawa. Electrofluidics fabricated by space-selective metallization in glass microfluidic structures using femtosecond laser direct writing. *Lab on a Chip*, 13(23):4608, 2013. doi:10.1039/c3lc50962a.

[124] J. Xu, D. Wu, J. Y. Ip, K. Midorikawa, and K. Sugioka. Vertical sidewall electrodes monolithically integrated into 3D glass microfluidic chips using water-assisted femtosecond-laser fabrication for in situ control of electrotaxis. *RSC Advances*, 5(31):24072–24080, 2015. doi:10.1039/C5RA00256G.

[125] M. Ashby. The CES EduPack Resource Booklet 2 - Material and Process selection charts, Jan. 2009.

[126] L. A. 04/14/2022 2:10:02 PM. https://d3i71xaburhd42.cloudfront.net/ 34d27311f945ed2fbedee495ecdb7a59c107c1f4/ 6-Table1-1.png.

[127] H. J. T. Ellingham. Reducibility of oxides and sulphides in metallurgical processes. *Journal of the Society of Chemical Industry*, 63(5):125–160, May 1944. doi:10.1002/jctb.5000630501.

[128] L. A. 04/14/2022 2:11:35 PM. https://upload.wikimedia.org/wikipedia/commons/thumb /6/6a/Ellingham _richardson-diagram_english.svg/440px-Ellingham _richardson-diagram_english.svg.png.

[129] L. Borasi, E. Casamenti, R. Charvet, C. Dénéréaz, S. Pollonghini, L. Deillon, T. Yang, F. Ebrahim, A. Mortensen, and Y. Bellouard. 3D metal freeform micromanufacturing. *Journal of Manufacturing Processes*, 68:867–876, Aug. 2021. doi:10.1016/j.jmapro.2021.06.002.

[130] E. Casamenti, G. Torun, L. Borasi, M. Lautenbacher, M. Bertrand, J. Faist, A. Mortensen, and Y. Bellouard. Glass-in-glass infiltration for 3D micro-optical composite components. *Optics Express*, Mar. 2022. doi:10.1364/OE.451026.

[131] H. Kodama. Automatic method for fabricating a three-dimensional plastic model with photo-hardening polymer. *Review of Scientific Instruments*, 52(11):1770–1773, Nov. 1981. doi:10.1063/1.1136492.

[132] K. Ikuta and K. Hirowatari. Real three dimensional micro fabrication using stereo lithography and metal molding. In *[1993] Proceedings IEEE Micro Electro Mechanical Systems*, pages 42–47, Fort Lauderdale, FL, USA, 1993. IEEE. ISBN 978-0-7803-0957-9. doi:10.1109/MEMSYS.1993.296949.

[133] S. Maruo, O. Nakamura, and S. Kawata. Three-dimensional microfabrication with two-photon-absorbed photopolymerization. *Optics Letters*, 22(2):132–134, Jan. 1997. doi:10.1364/OL.22.000132. Publisher: Optical Society of America.

[134] S. Kawata, H.-B. Sun, T. Tanaka, and K. Takada. Finer features for functional microdevices. *Nature*, 412(6848):697–698, Aug. 2001. doi:10.1038/35089130. Number: 6848 Publisher: Nature Publishing Group.

[135] Y. Cheng, K. Sugioka, K. Midorikawa, M. Masuda, K. Toyoda, M. Kawachi, and K. Shihoyama. Three-dimensional micro-optical components embedded in photosensitive glass by a femtosecond laser. *Optics Letters*, 28(13):1144, July 2003. doi:10.1364/OL.28.001144.

[136] C. A. Ross, D. G. MacLachlan, D. Choudhury, and R. R. Thomson. Optimisation of ultrafast laser assisted etching in fused silica. *Optics Express*, 26(19):24343, Sept. 2018. doi:10.1364/OE.26.024343.

[137] S. Rajesh and Y. Bellouard. Towards fast femtosecond laser micromachining of fused silica: The effect of deposited energy. *Optics Express*, 18(20):21490, Sept. 2010. doi:10.1364/OE.18.021490.

[138] X. Li, T. Abe, and M. Esashi. Deep reactive ion etching of Pyrex glass using SF6 plasma. *Sensors and Actuators A: Physical*, 87(3):139–145, Jan. 2001. doi:10.1016/S0924-4247(00)00482-9.

[139] B. Park, Y. Choi, and C. Chu. Prevention of Exit Crack in Micro Drilling of Soda-Lime Glass. *CIRP Annals*, 51(1):347–350, 2002. doi:10.1016/S0007-8506(07)61533-9.

[140] A. A. Tseng, Y.-T. Chen, and K.-J. Ma. Fabrication of high-aspect-ratio microstructures using excimer laser. *Optics and Lasers in Engineering*, 41(6):827–847, June 2004. doi:10.1016/S0143-8166(03)00062-9.

[141] B. R. Sarkar, B. Doloi, and B. Bhattacharyya. Parametric analysis on electrochemical discharge machining of silicon nitride ceramics. *The International Journal of Advanced Manufacturing Technology*, 28(9-10):873–881, July 2006. doi:10.1007/s00170-004-2448-1.

[142] M. K. Bhuyan, F. Courvoisier, P.-A. Lacourt, M. Jacquot, L. Furfaro, M. J. Withford, and J. M. Dudley. High aspect ratio taper-free microchannel fabrication using femtosecond Bessel beams. *Optics Express*, 18(2):566, Jan. 2010. doi:10.1364/OE.18.000566.

[143] L. Jiang, P. Liu, X. Yan, N. Leng, C. Xu, H. Xiao, and Y. Lu. High-throughput rear-surface drilling of microchannels in glass based on electron dynamics control using femtosecond pulse trains. *Optics Letters*, 37(14):2781, July 2012. doi:10.1364/OL.37.002781.

[144] L. Brusberg, M. Queisser, C. Gentsch, H. Schröder, and K.-D. Lang. Advances in CO2-Laser Drilling of Glass Substrates. *Physics Procedia*, 39:548–555, 2012. doi:10.1016/j.phpro.2012.10.072.

[145] S. Karimelahi, L. Abolghasemi, and P. R. Herman. Rapid micromachining of high aspect ratio holes in fused silica glass by high repetition rate picosecond laser. *Applied Physics A*, 114(1):91–111, Jan. 2014. doi:10.1007/s00339-013-8155-8.

[146] L. Hof and J. Abou Ziki. Micro-Hole Drilling on Glass Substrates—A Review. *Micromachines*, 8(2):53, Feb. 2017. doi:10.3390/mi8020053.

[147] S. Richter, A. Plech, M. Steinert, M. Heinrich, S. Döring, F. Zimmermann, U. Peschel, E. Kley, A. Tünnermann, and S. Nolte. On the fundamental structure of femtosecond laser-induced nanogratings. *Laser & Photonics Reviews*, 6(6):787–792, Nov. 2012. doi:10.1002/lpor.201200048.

[148] F. Zimmermann, A. Plech, S. Richter, S. Döring, A. Tünnermann, and S. Nolte. Structural evolution of nanopores and cracks as fundamental constituents of ultrashort pulse-induced nanogratings. *Applied Physics A*, 114(1):75–79, Jan. 2014. doi:10.1007/s00339-013-8093-5.

[149] E. Bricchi and P. G. Kazansky. Extraordinary stability of anisotropic femtosecond direct-written structures embedded in silica glass. *Applied Physics Letters*, 88(11):111119, Mar. 2006. doi:10.1063/1.2185587.

[150] M. Cavillon, Y. Wang, B. Poumellec, F. Brisset, and M. Lancry. Erasure of nanopores in silicate glasses induced by femtosecond laser irradiation in the Type II regime. *Applied Physics A*, 126(11):876, Nov. 2020. doi:10.1007/s00339-020-04062-8.

[151] S.-E. Wei, Y. Wang, H. Yao, M. Cavillon, B. Poumellec, G.-D. Peng, and M. Lancry. Thermal Stability of Type II Modifications by IR Femtosecond Laser in Silica-based Glasses. *Sensors*, 20(3):762, Jan. 2020. doi:10.3390/s20030762.

[152] Y. Li, M. Yang, D. N. Wang, J. Lu, T. Sun, and K. T. Grattan. Fiber Bragg gratings with enhanced thermal stability by residual stress relaxation. *Optics Express*, 17(22):19785, Oct. 2009. doi:10.1364/OE.17.019785.

[153] J. J. Witcher, W. J. Reichman, L. B. Fletcher, N. W. Troy, and D. M. Krol. Thermal annealing of femtosecond laser written structures in silica glass. *Optical Materials Express*, 3(4): 502, Apr. 2013. doi:10.1364/OME.3.000502.

[154] Y. Su, H. Yin, X. He, and Y. Zhou. Influence of annealing on the structure of silica glass. *Journal of Wuhan University of Technology-Mater. Sci. Ed.*, 28(5):902–906, Oct. 2013. doi:10.1007/s11595-013-0790-6.

[155] C. Fiori and R. A. B. Devine. Evidence for a wide continuum of polymorphs in a-SiO2. *Physical Review B*, 33(4):2972–2974, Feb. 1986. doi:10.1103/PhysRevB.33.2972.

[156] A. Agarwal and M. Tomozawa. Correlation of silica glass properties with the infrared spectra. *Journal of Non-Crystalline Solids*, 209(1-2):166–174, Jan. 1997. doi:10.1016/S0022-3093(96)00542-X.

[157] K. Awazu and H. Kawazoe. Strained Si–O–Si bonds in amorphous SiO2 materials: A family member of active centers in radio, photo, and chemical responses. *Journal of Applied Physics*, 94(10):6243–6262, Nov. 2003. doi:10.1063/1.1618351.

[158] M. Sakakura, Y. Lei, L. Wang, Y.-H. Yu, and P. G. Kazansky. Ultralow-loss geometric phase and polarization shaping by ultrafast laser writing in silica glass. *Light: Science & Applications*, 9(1):15, Dec. 2020. doi:10.1038/s41377-020-0250-y.

[159] X. W. Wang, R. Buividas, F. Funabiki, P. R. Stoddart, H. Hosono, and S. Juodkazis. Analysis of defects patterned by femtosecond pulses inside KBr and SiO2 glass. *Applied Physics A*, 122(3):194, Mar. 2016. doi:10.1007/s00339-016-9647-0.

[160] S. Juodkazis, K. Yamasaki, V. Mizeikis, S. Matsuo, and H. Misawa. Formation of embedded patterns in glasses using femtosecond irradiation. *Applied Physics A*, 79(4-6): 1549–1553, Sept. 2004. doi:10.1007/s00339-004-2845-1.

[161] *Fundamentals of Microfabrication : The Science of Miniaturization, Second Edition*. CRC Press, Oct. 2018. ISBN 978-1-315-27422-5. doi:10.1201/9781482274004.

[162] S. Y. Chin, V. Dikshit, B. Meera Priyadarshini, and Y. Zhang. Powder-Based 3D Printing for the Fabrication of Device with Micro and Mesoscale Features. *Micromachines*, 11(7): 658, July 2020. doi:10.3390/mi11070658. Number: 7 Publisher: Multidisciplinary Digital Publishing Institute.

[163] E. Becker, W. Ehrfeld, P. Hagmann, A. Maner, and D. Münchmeyer. Fabrication of microstructures with high aspect ratios and great structural heights by synchrotron radiation lithography, galvanoforming, and plastic moulding (LIGA process). *Microelectronic Engineering*, 4(1):35–56, May 1986. doi:10.1016/0167-9317(86)90004-3.

[164] H. Lorenz, M. Despont, P. Vettiger, and P. Renaud. Fabrication of photoplastic high-aspect ratio microparts and micromolds using SU-8 UV resist. *Microsystem Technologies*, 4(3):143–146, May 1998. doi:10.1007/s005420050118.

[165] J. Melngailis. Focused ion beam technology and applications. *Journal of Vacuum Science & Technology B: Microelectronics and Nanometer Structures*, 5(2):469, Mar. 1987. doi:10.1116/1.583937.

[166] S. Reyntjens and R. Puers. A review of focused ion beam applications in microsystem technology. *Journal of Micromechanics and Microengineering*, 11(4):287–300, July 2001. doi:10.1088/0960-1317/11/4/301.

[167] C. A. Volkert and A. M. Minor. Focused Ion Beam Microscopy and Micromachining. *MRS Bulletin*, 32(5):389–399, May 2007. doi:10.1557/mrs2007.62.

[168] J. Xu, X. Wang, C. Wang, L. Yuan, W. Chen, J. Bao, Q. Su, Z. Xu, C. Wang, Z. Wang, D. Shan, and B. Guo. A Review on Micro/Nanoforming to Fabricate 3D Metallic Structures. *Advanced Materials*, 33(6):2000893, Feb. 2021. doi:10.1002/adma.202000893.

[169] T. Tanaka, A. Ishikawa, and S. Kawata. Two-photon-induced reduction of metal ions for fabricating three-dimensional electrically conductive metallic microstructure. *Applied Physics Letters*, 88(8):081107, Feb. 2006. doi:10.1063/1.2177636.

[170] Y. Hanada, K. Sugioka, and K. Midorikawa. Selective metallization of photostructurable glass by femtosecond laser direct writing for biochip application. *Applied Physics A*, 90 (4):603–607, Mar. 2008. doi:10.1007/s00339-007-4373-2.

[171] L. Hirt, A. Reiser, R. Spolenak, and T. Zambelli. Additive Manufacturing of Metal Structures at the Micrometer Scale. *Advanced Materials*, 29(17):1604211, May 2017. doi:10.1002/adma.201604211.

[172] A. Reiser, L. Koch, K. A. Dunn, T. Matsuura, F. Iwata, O. Fogel, Z. Kotler, N. Zhou, K. Charipar, A. Piqué, P. Rohner, D. Poulikakos, S. Lee, S. K. Seol, I. Utke, C. Nisselroy, T. Zambelli, J. M. Wheeler, and R. Spolenak. Metals by Micro-Scale Additive Manufacturing: Comparison of Microstructure and Mechanical Properties. *Advanced Functional Materials*, 30(28):1910491, July 2020. doi:10.1002/adfm.201910491.

[173] P.-W. Wu, W. Cheng, I. B. Martini, B. Dunn, B. J. Schwartz, and E. Yablonovitch. Two-photon photographic production of three-dimensional metallic structures within a dielectric matrix. *Advanced Materials*, 12(19):1438–1441, 2000. doi:https://doi.org/10.1002/1521-4095(200010)12:19<1438::AID-ADMA1438>3.0.CO;2-Y.

[174] M. S. Saleh, C. Hu, and R. Panat. Three-dimensional microarchitected materials and devices using nanoparticle assembly by pointwise spatial printing. *Science Advances*, 3 (3):e1601986, Mar. 2017. doi:10.1126/sciadv.1601986.

[175] D. Oran, S. G. Rodriques, R. Gao, S. Asano, M. A. Skylar-Scott, F. Chen, P. W. Tillberg, A. H. Marblestone, and E. S. Boyden. 3D nanofabrication by volumetric deposition and controlled shrinkage of patterned scaffolds. *Science*, 362(6420):1281–1285, Dec. 2018. doi:10.1126/science.aau5119.

[176] A. Vyatskikh, S. Delalande, A. Kudo, X. Zhang, C. M. Portela, and J. R. Greer. Additive manufacturing of 3D nano-architected metals. *Nature Communications*, 9(1):593, Dec. 2018. doi:10.1038/s41467-018-03071-9.

[177] N. J. Wilkinson, M. A. A. Smith, R. W. Kay, and R. A. Harris. A review of aerosol jet printing—a non-traditional hybrid process for micro-manufacturing. *The International Journal of Advanced Manufacturing Technology*, 105(11):4599–4619, Dec. 2019. doi:10.1007/s00170-019-03438-2.

[178] I. Utke, J. Michler, R. Winkler, and H. Plank. Mechanical Properties of 3D Nanostructures Obtained by Focused Electron/Ion Beam-Induced Deposition: A Review. *Micromachines*, 11(4):397, Apr. 2020. doi:10.3390/mi11040397.

[179] T. M. Braun and D. T. Schwartz. The Emerging Role of Electrodeposition in Additive Manufacturing. *Interface magazine*, 25(1):69–73, Jan. 2016. doi:10.1149/2.F07161if.

[180] A. Reiser, M. Lindén, P. Rohner, A. Marchand, H. Galinski, A. S. Sologubenko, J. M. Wheeler, R. Zenobi, D. Poulikakos, and R. Spolenak. Multi-metal electrohydrodynamic

redox 3D printing at the submicron scale. *Nature Communications*, 10(1):1853, Dec. 2019. doi:10.1038/s41467-019-09827-1.

[181] G. Ercolano, T. Zambelli, C. van Nisselroy, D. Momotenko, J. Vörös, T. Merle, and W. W. Koelmans. Multiscale Additive Manufacturing of Metal Microstructures. *Advanced Engineering Materials*, 22(2):1900961, Feb. 2020. doi:10.1002/adem.201900961.

[182] J. Krebs, S. I. Rao, S. Verheyden, C. Miko, R. Goodall, W. A. Curtin, and A. Mortensen. Cast aluminium single crystals cross the threshold from bulk to size-dependent stochastic plasticity. *Nature Materials*, 16(7):730–736, July 2017. doi:10.1038/nmat4911.

[183] Z. Sun, G. Vladimirov, E. Nikolaev, and L. F. Velasquez-Garcia. Exploration of Metal 3-D Printing Technologies for the Microfabrication of Freeform, Finely Featured, Mesoscaled Structures. *Journal of Microelectromechanical Systems*, 27(6):1171–1185, Dec. 2018. doi:10.1109/JMEMS.2018.2875158.

[184] D. Du, X. Liu, G. Korn, J. Squier, and G. Mourou. Laser-induced breakdown by impact ionization in SiO $_2$ with pulse widths from 7 ns to 150 fs. *Applied Physics Letters*, 64(23): 3071–3073, June 1994. doi:10.1063/1.111350.

[185] E. N. Glezer, M. Milosavljevic, L. Huang, R. J. Finlay, T.-H. Her, J. P. Callan, and E. Mazur. Three-dimensional optical storage inside transparent materials. *Optics Letters*, 21(24): 2023, Dec. 1996. doi:10.1364/OL.21.002023.

[186] W. Oliver and G. Pharr. An improved technique for determining hardness and elastic modulus using load and displacement sensing indentation experiments. *Journal of Materials Research*, 7(6):1564–1583, June 1992. doi:10.1557/JMR.1992.1564.

[187] K. Hasse, G. Huber, and C. Kränkel. Selective etching of fs-laser inscribed high aspect ratio microstructures in YAG. *Optical Materials Express*, 9(9):3627, Sept. 2019. doi:10.1364/OME.9.003627.

[188] F. Madani-Grasset and Y. Bellouard. Femtosecond laser micromachining of fused silica molds. *Optics Express*, 18(21):21826, Oct. 2010. doi:10.1364/OE.18.021826.

[189] A. Schaap and Y. Bellouard. Molding topologically-complex 3D polymer microstructures from femtosecond laser machined glass. *Optical Materials Express*, 3(9):1428, Sept. 2013. doi:10.1364/OME.3.001428.

[190] B. Wu, A. Heidelberg, J. J. Boland, J. E. Sader, Sun, and Li. Microstructure-Hardened Silver Nanowires. *Nano Letters*, 6(3):468–472, Mar. 2006. doi:10.1021/nl052427f.

[191] J. Dolbow and M. Gosz. Effect of out-of-plane properties of a polyimide film on the stress fields in microelectronic structures. *Mechanics of Materials*, 23(4):311–321, Aug. 1996. doi:10.1016/0167-6636(96)00021-X.

[192] G. M. Pharr and W. C. Oliver. Nanoindentation of silver-relations between hardness and dislocation structure. *Journal of Materials Research*, 4(1):94–101, Feb. 1989. doi:10.1557/JMR.1989.0094.

[193] Q. Ma and D. R. Clarke. Size dependent hardness of silver single crystals. *Journal of Materials Research*, 10(4):853–863, Apr. 1995. doi:10.1557/JMR.1995.0853.

[194] Y. Bellouard, E. Barthel, A. A. Said, M. Dugan, and P. Bado. Scanning thermal microscopy and Raman analysis of bulk fused silica exposed to lowenergy femtosecond laser pulses. *Optics Express*, 16(24):19520, Nov. 2008. doi:10.1364/OE.16.019520.

[195] V. Zanetti. *Piccola guida di Murano*. Libreria Filippi editrice, Venezia, 1869.

[196] A. Tosi and A. De Palma, editors. *La memoria del vetro: Murano e l'arte vetraria nelle storie dei suoi maestri*. Marsilio : Scuola del vetro Abate Zanetti, Venezia, 2006. ISBN 978-88-317-9217-2.

[197] A. Pellatt. *Curiosities of glass making: with details of the processes and productions of ancient and modern ornamental glass manufacture*. 2012. ISBN 978-1-230-26028-0 978-0-217-19814-1. OCLC: 895281279.

[198] M. Daumas. *Les Instruments Scientifiques aux XVIIe et XVIIIe Siecles*. Paris: Presses Universitaires de France, Paris, 1st edition, 1953.

[199] B. J. Eggleton, B. Luther-Davies, and K. Richardson. Chalcogenide photonics. *Nature Photonics*, 5(3):141–148, Mar. 2011. doi:10.1038/nphoton.2011.309.

[200] X. Zhang, B. Bureau, P. Lucas, C. Boussard-Pledel, and J. Lucas. Glasses for Seeing Beyond Visible. *Chemistry - A European Journal*, 14(2):432–442, Jan. 2008. doi:10.1002/chem.200700993.

[201] R. R. Gattass, R. Thapa, F. H. Kung, L. E. Busse, L. B. Shaw, and J. S. Sanghera. Review of infrared fiber-based components. *Applied Optics*, 54(31):F25, Nov. 2015. doi:10.1364/AO.54.000F25.

[202] C. R. Petersen, U. Møller, I. Kubat, B. Zhou, S. Dupont, J. Ramsay, T. Benson, S. Sujecki, N. Abdel-Moneim, Z. Tang, D. Furniss, A. Seddon, and O. Bang. Mid-infrared supercontinuum covering the 1.4–13.3 μm molecular fingerprint region using ultrahigh NA chalcogenide step-index fibre. *Nature Photonics*, 8(11):830–834, Nov. 2014. doi:10.1038/nphoton.2014.213.

[203] N. Abdellaoui, F. Starecki, C. Boussard-Pledel, Y. Shpotyuk, J.-L. Doualan, A. Braud, E. Baudet, P. Nemec, F. Cheviré, M. Dussauze, B. Bureau, P. Camy, and V. Nazabal. Tb3+ doped Ga 5 Ge 20 Sb 10 Se 65-x Te-x (x = 0-375) chalcogenide glasses and fibers for MWIR and LWIR emissions. *Optical Materials Express*, 8(9):2887, Sept. 2018. doi:10.1364/OME.8.002887.

[204] M. F. Churbanov, V. S. Shiryaev, V. V. Gerasimenko, A. A. Pushkin, I. V. Skripachev, G. E. Snopatin, and V. G. Plotnichenko. Stability of the Optical and Mechanical Properties of Chalcogenide Fibers. *Inorganic Materials*, 38(10):1063–1068, 2002. doi:10.1023/A:1020593708749.

[205] O. Mouawad, C. Strutynski, J. Picot-Clémente, F. Désévédavy, G. Gadret, J.-C. Jules, and F. Smektala. Optical aging behaviour naturally induced on As_2s_3 microstructured optical fibres. *Optical Materials Express*, 4(10):2190, Oct. 2014. doi:10.1364/OME.4.002190.

[206] T. Miyashita and Y. Terunuma. Optical Transmission Loss of As-S Glass Fiber in 1.0-5.5 μm Wavelength Region. *Japanese Journal of Applied Physics*, 21(Part 2, No. 2):L75–L76, Feb. 1982. doi:10.1143/JJAP.21.L75.

[207] M. Asobe, T. Kanamori, and K. Kubodera. Ultrafast all-optical switching using highly nonlinear chalcogenide glass fiber. *IEEE Photonics Technology Letters*, 4(4):362–365, Apr. 1992. doi:10.1109/68.127214.

[208] J. Zhu, T. M. Horning, M. Zohrabi, W. Park, and J. T. Gopinath. Photo-induced writing and erasing of gratings in As $_2$ S $_3$ chalcogenide microresonators. *Optica*, 7(11):1645, Nov. 2020. doi:10.1364/OPTICA.405136.

[209] M. A. Schmidt, N. Granzow, N. Da, M. Peng, L. Wondraczek, and P. S. J. Russell. All-solid bandgap guiding in tellurite-filled silica photonic crystal fibers. *Optics Letters*, 34(13):1946, July 2009. doi:10.1364/OL.34.001946.

[210] N. Da, L. Wondraczek, M. A. Schmidt, N. Granzow, and P. S. J. Russell. High index-contrast all-solid photonic crystal fibers by pressure-assisted melt infiltration of silica matrices. *Journal of Non-Crystalline Solids*, 356(35-36):1829–1836, Aug. 2010. doi:10.1016/j.jnoncrysol.2010.07.002.

[211] J. Kobelke, R. Spittel, D. Hoh, K. Schuster, A. Schwuchow, F. Jahn, F. Just, C. Segel, A. Hartung, J. Kirchhof, and H. Bartelt. Preparation and characterization of microstructured silica holey fibers filled with high-index glasses. page 80732F, Prague, Czech Republic, May 2011. doi:10.1117/12.886243.

[212] R. Spittel, J. Kobelke, D. Hoh, F. Just, K. Schuster, A. Schwuchow, F. Jahn, J. Kirchhof, M. Jäger, and H. Bartelt. Arsenic chalcogenide filled photonic crystal fibers. *Journal of Non-Crystalline Solids*, 377:231–235, Oct. 2013. doi:10.1016/j.jnoncrysol.2013.01.043.

[213] C. C. Huang, D. W. Hewak, and J. V. Badding. Deposition and characterization of germanium sulphide glass planar waveguides. *Optics Express*, 12(11):2501, 2004. doi:10.1364/OPEX.12.002501.

[214] S. Serna, H. Lin, C. Alonso-Ramos, C. Lafforgue, X. Le Roux, K. A. Richardson, E. Cassan, N. Dubreuil, J. Hu, and L. Vivien. Engineering third-order optical nonlinearities in hybrid chalcogenide-on-silicon platform. *Optics Letters*, 44(20):5009, Oct. 2019. doi:10.1364/OL.44.005009.

Bibliography

[215] W. C. Tan, M. E. Solmaz, J. Gardner, R. Atkins, and C. Madsen. Optical characterization of a-As2S3 thin films prepared by magnetron sputtering. *Journal of Applied Physics*, 107 (3):033524, Feb. 2010. doi:10.1063/1.3295908.

[216] K. E. Youden, T. Grevatt, R. W. Eason, H. N. Rutt, R. S. Deol, and G. Wylangowski. Pulsed laser deposition of Ga-La-S chalcogenide glass thin film optical waveguides. *Applied Physics Letters*, 63(12):1601–1603, Sept. 1993. doi:10.1063/1.110730.

[217] X. Zhang, Y. Guimond, and Y. Bellec. Production of complex chalcogenide glass optics by molding for thermal imaging. *Journal of Non-Crystalline Solids*, 326-327:519–523, Oct. 2003. doi:10.1016/S0022-3093(03)00464-2.

[218] J. Owen, M. Davies, D. Schmidt, and E. Urruti. On the ultra-precision diamond machining of chalcogenide glass. *CIRP Annals*, 64(1):113–116, 2015. doi:10.1016/j.cirp.2015.04.065.

[219] S. Saini, K. Kritika, D. Devvrat, and M. D. Sharma. Survey of chalcogenide glasses for engineering applications. *Materials Today: Proceedings*, 45:5523–5528, 2021. doi:10.1016/j.matpr.2021.02.297.

[220] E. Baudet, Y. Ledemi, P. Larochelle, S. Morency, and Y. Messaddeq. 3D-printing of arsenic sulfide chalcogenide glasses. *Optical Materials Express*, 9(5):2307, May 2019. doi:10.1364/OME.9.002307.

[221] J. Carcreff, F. Cheviré, E. Galdo, R. Lebullenger, A. Gautier, J. L. Adam, D. L. Coq, L. Brilland, R. Chahal, G. Renversez, and J. Troles. Mid-infrared hollow core fiber drawn from a 3D printed chalcogenide glass preform. *Optical Materials Express*, 11(1):198, Jan. 2021. doi:10.1364/OME.415090.

[222] J. Carcreff, F. Cheviré, R. Lebullenger, A. Gautier, R. Chahal, J. L. Adam, L. Calvez, L. Brilland, E. Galdo, D. Le Coq, G. Renversez, and J. Troles. Investigation on Chalcogenide Glass Additive Manufacturing for Shaping Mid-infrared Optical Components and Microstructured Optical Fibers. *Crystals*, 11(3):228, Feb. 2021. doi:10.3390/cryst11030228.

[223] S. I. Nazir and Y. Bellouard. Contactless Optical Packaging Concept for Laser to Fiber Coupling. *IEEE Transactions on Components, Packaging and Manufacturing Technology*, 11(6):1035–1043, June 2021. doi:10.1109/TCPMT.2021.3080513.

[224] A. Mortensen, Y. Bellouard, R. Charvet, and C. Dénéréaz. Small-scale metal castings, small-scale metal/transparent composite structures, and process to produce the same, Nov. 2020.

[225] S. Song, J. Dua, and C. B. Arnold. Influence of annealing conditions on the optical and structural properties of spin-coated As_2s_3 chalcogenide glass thin films. *Optics Express*, 18(6):5472, Mar. 2010. doi:10.1364/OE.18.005472.

[226] R. P. Wang, S. J. Madden, C. J. Zha, A. V. Rode, and B. Luther-Davies. Annealing induced phase transformations in amorphous As2S3 films. *Journal of Applied Physics*, 100(6): 063524, Sept. 2006. doi:10.1063/1.2353787.

[227] H. Khan, S. Islam, P. K. Dwivedi, N. Dilawar, M. Husain, and M. Zulfequar. Effect of Annealing Temperature on Optical and Structural Properties of Solution Processed As2S3 Chalcogenide Glass Films. *Materials Today: Proceedings*, 21:2072–2078, 2020. doi:10.1016/j.matpr.2020.01.326.

[228] A. Pasquarello and R. Car. Identification of Raman Defect Lines as Signatures of Ring Structures in Vitreous Silica. *Physical Review Letters*, 80(23):5145–5147, June 1998. doi:10.1103/PhysRevLett.80.5145.

[229] N. Shen, M. J. Matthews, S. Elhadj, P. E. Miller, A. J. Nelson, and J. Hamilton. Correlating optical damage threshold with intrinsic defect populations in fused silica as a function of heat treatment temperature. *Journal of Physics D: Applied Physics*, 46(16):165305, Apr. 2013. doi:10.1088/0022-3727/46/16/165305.

[230] A. E. Geissberger and F. L. Galeener. Raman studies of vitreous Si O 2 versus fictive temperature. *Physical Review B*, 28(6):3266–3271, Sept. 1983. doi:10.1103/PhysRevB.28.3266.

[231] T. Wagner, S. O. Kasap, M. Vlcek, A. Sklenár, and A. Stronski. Modulated temperature differential scanning calorimetry and Raman spectroscopy studies of asxs100x glasses. *Journal of Materials Science*, 33(23):5581–5588, 1998. doi:10.1023/A:1004455929749.

[232] W. Li, S. Seal, C. Rivero, C. Lopez, K. Richardson, A. Pope, A. Schulte, S. Myneni, H. Jain, K. Antoine, and A. C. Miller. Role of s/se ratio in chemical bonding of as-s-se glasses investigated by raman, x-ray photoelectron, and extended x-ray absorption fine structure spectroscopies. *Journal of Applied Physics*, 98(5):053503, Sept. 2005. doi:10.1063/1.2009815.

[233] L. Mandrile, I. Cagnasso, L. Berta, A. M. Giovannozzi, M. Petrozziello, F. Pellegrino, A. Asproudi, F. Durbiano, and A. M. Rossi. Direct quantification of sulfur dioxide in wine by Surface Enhanced Raman Spectroscopy. *Food Chemistry*, 326:127009, Oct. 2020. doi:10.1016/j.foodchem.2020.127009.

[234] P. Bazylewski, R. Divigalpitiya, and G. Fanchini. In situ Raman spectroscopy distinguishes between reversible and irreversible thiol modifications in L-cysteine. *RSC Advances*, 7(5):2964–2970, 2017. doi:10.1039/C6RA25879D.

[235] C. Luo, E. Hu, K. J. Gaskell, X. Fan, T. Gao, C. Cui, S. Ghose, X.-Q. Yang, and C. Wang. A chemically stabilized sulfur cathode for lean electrolyte lithium sulfur batteries. *Proceedings of the National Academy of Sciences*, 117(26):14712–14720, June 2020. doi:10.1073/pnas.2006301117.

Bibliography

[236] Y. Song, Z. Liu, H.-k. Mao, R. J. Hemley, and D. R. Herschbach. High-pressure vibrational spectroscopy of sulfur dioxide. *The Journal of Chemical Physics*, 122(17):174511, May 2005. doi:10.1063/1.1883405.

[237] S. Tsuchihashi and Y. Kawamoto. Properties and structure of glasses in the system As[]S. *Journal of Non-Crystalline Solids*, 5(4):286–305, Mar. 1971. doi:10.1016/0022-3093(71)90069-X.

[238] P. Sachan, R. Singh, P. K. Dwivedi, and A. Sharma. Infrared microlenses and gratings of chalcogenide: confined self-organization in solution processed thin liquid films. *RSC Advances*, 8(49):27946–27955, 2018. doi:10.1039/C8RA03249A.

[239] W. F. Glaze, D. H. Blackburn, J. S. Osmalov, D. Hubbard, and M. H. Black. Properties of Arsenic Sulfide Glass. *Journal of Research of the National Bureau of Standards*, 59(2), Aug. 1957.

[240] Y. Cheng, K. Sugioka, K. Midorikawa, M. Masuda, K. Toyoda, M. Kawachi, and K. Shihoyama. Control of the cross-sectional shape of a hollow microchannel embedded in photostructurable glass by use of a femtosecond laser. *Optics Letters*, 28(1):55, Jan. 2003. doi:10.1364/OL.28.000055.

[241] S. Matsuo, H. Sumi, S. Kiyama, T. Tomita, and S. Hashimoto. Femtosecond laser-assisted etching of Pyrex glass with aqueous solution of KOH. *Applied Surface Science*, 255(24):9758–9760, Sept. 2009. doi:10.1016/j.apsusc.2009.04.065.

[242] A. A. Serkov and H. V. Snelling. Enhanced chemical etch rate of borosilicate glass via spatially resolved laser-generated color centers. *Journal of Physics D: Applied Physics*, 53 (13):135306, Mar. 2020. doi:10.1088/1361-6463/ab6515.

[243] D. Bischof, M. Kahl, and M. Michler. Laser-assisted etching of borosilicate glass in potassium hydroxide. *Optical Materials Express*, 11(4):1185, Apr. 2021. doi:10.1364/OME.417871.

Curriculum Vitae

Enrico Casamenti

Born on 21st November 1993

Nationality: Italian

enrico.casamenti1@gmail.com

Education

2017-2022	**Ph.D. in Advanced Manufacturing**
	Institute of Electrical and Micro Engineering - Galatea Laboratory
	Ecole Polytechnique Fédérale de Lausanne (EPFL), Switzerland
2015-2017	**Master of Science in Mechanical Engineering**
	Department of Mechanical Engineering
	Politecnico di Torino, Italy
2015-2017	**Master of Science in Mechanical Engineering**
	Department of Mechanical Engineering
	University of Illinois at Chicago, United States
2007-2010	**Bachelor of Science in Mechanical Engineering**
	Department of Mechanical Engineering
	Politecnico di Torino, Italy

Journal articles

Enrico Casamenti, Tao Yang, Pieter Vlugter, and Yves Bellouard. *Vibration monitoring based on optical sensing of mechanical nonlinearities in glass suspended waveguides.* Optics Express, 29(7):10853-10862, March 2021. https://doi.org/10.1364/OE.414191.

Luciano Borasi, Enrico Casamenti, Raphaël Charvet, Cyril Dénéréaz, Sacha Pollonghini, Lea Deillon, Tao Yang, Fatmah Ebrahim, Andreas Mortensen, and Yves Bellouard. *3D metal*

freeform micromanufacturing. Journal of Manufacturing Processes, 68:867-876, August 2021. https://doi.org/10.1016/j.jmapro.2021.06.002.

Enrico Casamenti, Sacha Pollonghini, and Yves Bellouard. *Few pulses femtosecond laser exposure for high efficiency 3D glass micromachining.* Optics Express, 29(22):35054, October 2021. https://doi.org/10.1364/OE.435163. (Optics Express highlights October 2021)

E. Casamenti, G. Torun, L. Borasi, M. Lautenbacher, M. Bertrand, J. Faist, A. Mortensen, and Y. Bellouard, *Glass-in-glass infiltration for 3D micro-optical composite components,* Optics Express, 30(8):13603, 2022, April 2022.https://doi.org/10.1364/OE.451026. (Editor's pick)

Conferences

February 2019 - Enrico Casamenti, Tao Yang, Pieter Vlugter, and Yves Bellouard. *Dynamically tunable optomechanical large mode suspended waveguide for high power and broadband guided optics.* SPIE Photonics West - Advancements for laser technologies (LASE), San Francisco (CA), United States. (Oral presentation, Frontiers in Ultrafast Optics - 2nd best student paper award)

June 2021 - Enrico Casamenti, Luciano Borasi, Adeline Durand, Samuel Rey, Raphaël Charvet, Cyril Dénéréaz, Andreas Mortensen, and Yves Bellouard. *Femtosecond laser-assisted mould fabrication for metal casting at the micro-scale.* Lasers in Manufacturing (LiM), Munich, Germany. (Oral presentation)

June 2021 - Enrico Casamenti, Luciano Borasi, Adeline Durand, Samuel Rey, Raphaël Charvet, Cyril Dénéréaz, Andreas Mortensen, and Yves Bellouard. *Femtosecond laser-assisted mould fabrication for metal microcasting.* Laser Precision Microfabrication (LPM), Osaka, Japan. (Oral presentation)

December 2021 - Enrico Casamenti, Gözden Torun, Luciano Borasi, Maxime Lautenbacher, Andreas Mortensen, and Yves Bellouard. *On the fabrication of silica-chalcogenide three-dimensional micro-glass composite.* Pacific rim conference on ceramic and glass technology including Glass and optical materials division meeting (PACRIM/GOMD), Vancouver (BC), Canada. (Oral presentation)

February 2022 - Enrico Casamenti, Sacha Pollonghini, and Yves Bellouard. *Low fluence femtosecond laser exposure for fast 3D glass micromachining.* SPIE Photonics West - Advancements for laser technologies (LASE), San Francisco (CA), United States. (Oral presentation, LASE - 3D Printing 2022 Best Paper Award)